Generalized dispersion analysis of arbitrarily cut crystals with unknown orientation

Dissertation

zur Erlangung des akademischen Grades

doctor rerum naturalium (Dr. rer. nat.)

seit 1558

vorgelegt dem Rat der Chemisch-Geowissenschaftlichen Fakultät

der Friedrich-Schiller-Universität Jena

von Dipl.-Phys. **Sonja Höfer**

geboren am 19.04.1985 in Dernbach

Gutachter:

1. **Dr. habil. Thomas Mayerhöfer**

   Leibniz-Insitut für Photonische Technologien Jena, Deutschland

2. **Associate Prof. Vladimir Ivanovski**

   Sts. Cyril and Methodius University

   Faculty of Natural Sciences and Mathematics

   Institute of Chemistry, Skopje, Macedonia

3. **Prof. Roberto Moreira**

   Departamento de Fisica

   ICEx, Universidade Federal de Minas Gerais,

   Belo Horizonte MG, Brasilien

Tag der Verteidigung: 27.05.2015

Contents

1 Introduction **3**

2 Theoretical background **5**

2.1 Dielectric function 5

2.2 Characteristics of reflection bands 14

2.3 Measurement scheme 17

2.4 Crystal systems 20

2.5 Miller Indices 26

2.6 Stereographic projection 28

2.7 FT-IR-spectrometer 29

2.8 Fit routine and evaluation scheme 30

3 Characterization of investigated crystals **35**

3.1 Triclinic crystals 35

3.1.1 Copper sulfate pentayhdrate, $CuSO_4 \cdot 5\,H_2O$ 36

3.1.2 Potassium dichromate, $K_2Cr_2O_7$ 37

3.2 Uniaxial crystals 39

3.2.1 Quartz, SiO_2 39

3.2.2 Calcite, $CaCO_3$ 40

3.2.3 Lithium niobate, $LiNbO_3$ 41

3.3 Orthorhombic crystals 42

3.3.1 Neodymium gallate, $NdGaO_3$ 42

3.3.2 Topaz, $Al_2SiO_4(F, OH)$ 43

3.4 Monoclinic crystals 44

3.4.1 Yttrium ortho silicate, Y_2SiO_5 44

3.4.2 Spodumene, $LiAl(SiO_3)_2$ 45

4 Dispersion Analysis of triclinic crystals **47**

4.1 Results of dispersion analysis for $CuSO_4 \cdot 5\,H_2O$ 47

4.2 Results of dispersion analysis for $K_2Cr_2O_7$ 50

4.3 Comparison of orientation angles and dielectric function 54

4.4 Verification of oscillator parameters 56

5 Dispersion analysis of arbitrarily cut uniaxial crystals 59
5.1 Adaption of fit routine to uniaxial crystals 59
5.2 Results of dispersion analysis for quartz 62
5.3 Results of dispersion analysis for calcite 67
5.4 Results of dispersion analysis for lithium niobate 70
5.5 Verification of oscillator parameters 73

6 Dispersion analysis of arbitrarily cut orthorhombic crystals 76
6.1 Adaption of fit routine to orthorhombic crystals 76
6.2 Results of dispersion analysis for neodymium gallate 80
6.3 Results of dispersion analysis for topaz 86

7 Dispersion analysis of arbitrarily cut monoclinic crystals 93
7.1 Adaption of fit routine to monoclinic crystals 93
7.2 Results of dispersion analysis of monoclinic crystals 98

8 Summary 104

9 Zusammenfassung 108

Index of symbols 117

Chapter 1

Introduction

The term dispersion analysis was first defined by Spitzer and Kleinman in 1959 [1] and is described as the determination of dispersion parameters of a single crystal based on the evaluation of polarized reflection spectra. The oscillator parameters together with the dielectric background tensor are required to compute the dielectric tensor function of the sample in the investigated spectral range. The dielectric tensor function itself is the basis for a large variety of different optical calculations and allows to compute e.g reflection, transmission or scattering for arbitrary orientation of the material of interest with arbitrary angle of incidence and polarization state of the incoming light. The optical properties in the infrared (IR), visible (VIS) and ultraviolet (UV) spectral region are determined by phonons (IR) and electronic excitations (UV/VIS). The results of dispersion analysis can amongst others be employed to verify the results of quantum chemical calculations. The first successful dispersion analysis of a single crystal was applied to a cubic crystal and had been performed by Czerny [2] already in 1930 who characterized Reststrahlen bands in the IR spectral region. In that time, dispersion analysis was strongly hindered by the lack of computers as the performance of dispersion analysis strongly depends on computing capacity.

In 1959 Spitzer et al. [1] presented the first successful dispersion analysis of an anisotropic material. If an uniaxial crystal is cut appropriately, the complexity of dispersion analysis is reduced to a level equal to that for cubic crystal. The complexity of dispersion analysis of orthorhombic crystals is also reduced to a level equal for a cubic crystal by investigating an appropriate cut of the crystal. Early investigations on optical properties and dielectric dispersion of the biaxial orthorhombic crystals were e.g. done by Perry et al. [3] in 1965 on perovskite zirconates or by Wiesendanger [4] in 1973, who investigated potassium niobate, $KNbO_3$.

In monoclinic crystals, which also belong to the biaxial crystal systems, dispersion analysis is of considerably higher complexity due to the reduced symmetry of the crystal compared to uniaxial crystals. The theoretical basis for dispersion analysis of mon-

oclinic crystals has been first developed by Koch et al. in 1973 [5]. The first successful dispersion analysis of a monoclinic crystal was presented by Pavinich and Belousov in 1978 [6], yet a severe restriction of the employed formalism was the assumption of normal incidence, that also restricted the applications of dispersion analysis to the analysis of near normal incidence measurements.
Formulas for the reflection from triclinic crystals, also for normal incidence, were provided 10 years later by Emslie and Aronson in 1983 [7], who also made the first attempt of dispersion analysis of a triclinic crystal in 1985 [8]. This attempt was most probably not successful because only three spectra from two different mutually orthogonal crystal faces were investigated to determine the six unknown elements of the dielectric tensor function. Also did dispersion analysis of triclinic crystals require computational resources that were not available at that time.
Reinvestigating the original problem it turned out that even nowadays the computational effort of performing dispersion analysis for triclinic crystals is still challenging. Emslie and Aronson originally proposed that six reflectance spectra have to be employed to perform dispersion analysis, yet further investigations showed that a set of 6 spectra is not sufficient to yield reliable results [9, 10].
This work presents an extended formalism to perform dispersion analysis not only for triclinic crystals, but also for uniaxial, orthorhombic and monoclinic crystals. For the extended formalism the crystal does not need to be cut in an appropriate way, but dispersion analysis can now be performed on arbitrarily cut crystals with a priori unknown orientation. Therefore, for each crystal class the evaluation scheme must fulfill certain constraints according to the crystal symmetry. The constraints reduce the parameter space significantly, which makes it much easier for the fit to find suitable dispersion parameters. Furthermore, the extended formalism is not restricted to normal incidence any more. To verify the dispersion parameters found for the different arbitrarily cut crystals, the parameters were applied to model the measured spectra of a principal cut or the spectra of a polycrystalline sample of the crystal in question.
It is the aim of this thesis to work out a standardized measurement scheme applicable to all crystal classes and an optimization routine that respects the special symmetries of each of the investigated crystal classes.

Chapter 2

Theoretical background

2.1 Dielectric function

The investigated crystals described in this work are dielectric materials, the electrons are mobile only within the electron cloud of the atom or molecule. In the MIR spectral region (Mid Infra Red, wavenumbers of 400-4000 cm^{-1}) the vibrations of the molecular entities get excited, e.g. a periodic change in bond angle or a periodic change in bond length [11]. The FIR spectral region (Far Infra Red, wavenumbers below 400 cm^{-1}) reveals the lattice vibrations or phonons of the crystals.
The dielectric function ε describes the relation between the dielectric displacement field $\vec{D}$ and the external electric field $\vec{E}$ [12]. Physically, the $\vec{D}$-field describes the density of field lines in a given surface area. It is defined as

$$\vec{D} = \varepsilon \cdot \varepsilon_0 \cdot \vec{E} \tag{2.1}$$

with ε_0 the vacuum permittivity $\varepsilon_0 = 8.854 \cdot 10^{-12} A^2\, s^4/(kg\, m^{-3})$ [12, 13]. The dielectric function is frequency dependent but independent of direction for isotropic dielectric media and takes on tensor character for anisotropic media. In this section we want to find an expression for the dielectric function ε.
Exposed to an electric field in the IR-region the electron clouds get shifted so that the centers of the positive and negative charge do not coincide anymore. The molecular entities get polarized [13, 14] and obtain a dipole moment $\vec{p}$. As the dipole moment is created by the external field the dipole moment is called *induced dipole moment*. The corresponding effect is called displacement polarization [13] as the charges get displaced to each other. The induced dipole moment is proportional to the electric field of the electromagnetic wave

$$\vec{p} = \alpha \cdot \varepsilon_0 \cdot \vec{E}. \tag{2.2}$$

The proportionality factor α is called the *polarizability* of the atom or molecule. For isotropic crystals with cubic symmetry the polarizability α is a constant (in the IR spectral region), for all other crystal classes the polarizability is a tensor, depending on the polarization state of the incoming electromagnetic wave. For N atoms or molecules per m^3 of the dielectric material, the electric polarization $\vec{P}$ is the dipole moment per volume

$$\text{polarization} = \frac{\text{dipole moment} \times N}{\text{volume}} \qquad \longrightarrow \qquad \vec{P} = N \cdot \vec{p} = N \cdot \alpha \cdot \varepsilon_0 \cdot \vec{E}. \quad (2.3)$$

In that simple form equation 2.3 is valid only for gaseous samples, for which the individual molecules do not influence each other. In fluids and solid state samples this assumption does not hold and the polarizing field is the sum of the external electric field of the electromagnetic wave and the field created by the surrounding medium. This leads to an additional term considering the mutual influence of the molecules in fluids or solids. The polarization $\vec{P}$ takes on a modified form compared to equation 2.3 [13]:

$$\vec{P} = \underbrace{\frac{N \cdot \alpha}{1 - N \cdot \alpha/3}}_{\chi_e} \cdot \varepsilon_0 \cdot \vec{E} \quad (2.4)$$

The term $\frac{N \cdot \alpha}{1 - N \cdot \alpha/3}$ is defined as the dielectric susceptibility χ_e and indicates the ability of the atoms to be polarized. A high value for χ_e donates a high change in the polarizability. Equation 2.4 relates the dielectric susceptibility χ_e and the dielectric function ε by [12, 13]

$$\varepsilon = 1 + \chi_e = 1 + \frac{N \cdot \alpha}{1 - N \cdot \alpha/3}. \quad (2.5)$$

As ε is frequency dependent, it is $\varepsilon = \varepsilon(\omega)$. In an isotropic medium the polarizability $\vec{P}$ is parallel to the electric field. In anisotropic media like the investigated crystals the polarizability $\vec{P}$ is given by a vector equation with $\varepsilon(\omega)$ being a tensor now. The tensor $\mathbf{I}$ is the unity tensor:

$$\begin{pmatrix} P_x \\ P_y \\ P_z \end{pmatrix} = \varepsilon_0 \left[\begin{pmatrix} \varepsilon_{xx} & \varepsilon_{xy} & \varepsilon_{xz} \\ \varepsilon_{yx} & \varepsilon_{yy} & \varepsilon_{yz} \\ \varepsilon_{zx} & \varepsilon_{zy} & \varepsilon_{xx} \end{pmatrix} - \mathbf{I} \right] \cdot \begin{pmatrix} E_x \\ E_y \\ E_z \end{pmatrix} \quad (2.6)$$

The elements of $\vec{P}$ are calculated by

$$P_i = \varepsilon_0 \left(\varepsilon_{ij} - 1\right) \cdot E_i$$

with the summation over repeated indices, that means for the component P_x e.g. the summation is performed as follows:

$$P_x = \varepsilon_0 \left(\varepsilon_{xx} E_x + \varepsilon_{xy} E_y + \varepsilon_{xz} E_z\right) - \varepsilon_0 \cdot E_x \tag{2.7}$$

In nonmagnetic materials, that are not optically active, the dielectric tensor is real and symmetric with $\varepsilon_{ij} = \varepsilon_{ji}$ [15], which leads to six independent values of the dielectric tensor. Strictly speaking the tensor consists of 12 unknown elements as each element has a real and imaginary part. However, by Kramers-Kronig relation the real and imaginary part are not independent from each other and linked to each other [12, 16]. The components ε_{ji} depend on the choice of the axes of the dielectric tensor relative to the crystal structure. Because of its real and symmetric nature, it is always possible to find three mutual orthogonal axes for which the tensor can be diagonalized in such a way that the off-diagonal elements vanish, which leaves

$$P_x = \varepsilon_0 E_x(\varepsilon_{xx} - 1), \qquad P_y = \varepsilon_0 E_y(\varepsilon_{yy} - 1), \qquad P_z = \varepsilon_0 E_z(\varepsilon_{zz} - 1)$$

and

$$\varepsilon = \begin{pmatrix} \varepsilon_x & 0 & 0 \\ 0 & \varepsilon_y & 0 \\ 0 & 0 & \varepsilon_z \end{pmatrix} = \varepsilon_0 \begin{pmatrix} n_x^2 & 0 & 0 \\ 0 & n_y^2 & 0 \\ 0 & 0 & n_z^2 \end{pmatrix}. \tag{2.8}$$

The elements ε_x, ε_y, and ε_z are the principal dielectric functions and n_x, n_y, n_z are the principal indices of refraction. The diagonalization is independent of frequency for uniaxial and orthorhombic crystals, for which in diagonal form the dielectric axes are aligned parallel to the crystal axes. For monoclinic and triclinic crystals the diagonalization is frequency dependent, the diagonal form can be realized only for single wavenumbers. Additionally, the diagonalization can be performed for either the real part or the imaginary part as both parts have different orientations.
The calculation of the measured reflectance from a single crystal surface is based on a 4×4 matrix formalism that generalizes the formalism developed by Berreman [17] and Yeh [18]. Starting point of the calculation is a suitable oscillator model, like the Drude-Lorentz model [12]. With the Drude-Lorentz-model an expression for the polarizability α can be derived, which leads to an equation for the dielectric function by substituting α in equation 2.5 The semi-classic model of a Lorentz oscillator describes an electron that is bound to the atomic core and excited to harmonic vibrations by an electric field. The equation for the dielectric tensor function is derived from the equation of motion for a damped harmonic oscillator:

$$m_e \frac{\mathrm{d}^2 x}{\mathrm{d}t^2} + m_e \gamma \frac{\mathrm{d}x}{\mathrm{d}t} + m_e \omega_0^2 x = -e \cdot E_{lokal}^0 \cdot \exp^{-i\omega t} \tag{2.9}$$

The periodic exciting force is the interaction with the electromagnetic alternating field, m_e is the mass of the electron, x is the displacement of the electron at a certain time, t is the time, γ is the damping constant of the harmonic oscillator, and e is the charge of the electron. The frequencies ω_0 and ω are the resonance frequency of the oscillator and the frequency of the exciting field, respectively. The local amplitude of the exciting field is described by E^0_{lokal}. With the assumption of a plane wave with $E(\omega) = E^0_{lokal} \cdot \exp^{-i\omega t}$ The solution for $x(t)$ of equation 2.9 is

$$x(t) = \frac{-e \cdot E^0_{lokal}}{m_e(\omega_0^2 - \omega^2 - i\omega\gamma)} \cdot \exp^{-i\omega t} \tag{2.10}$$

The polarizability α in equation 2.4 can be substituted with $\alpha = \frac{\vec{p}}{\varepsilon_0 \cdot \vec{E}}$ from equation 2.2. Combined with the general definition of a dipole moment $\vec{P} = q \cdot \vec{x}$, with q the charge of the dipole (charge e of electron in this case) and $\vec{x}$ the vector that points from the negative to the positive charge α is given by:

$$\alpha = \frac{e \cdot |\vec{x}|}{\varepsilon_0 \cdot |\vec{E}|} \tag{2.11}$$

By inserting equation 2.10 into 2.11 the resulting expression for α is

$$\alpha(\omega) = \frac{e^2}{\varepsilon_0 m_e(\omega_0^2 - \omega^2 - i\omega\gamma)} \tag{2.12}$$

Substituting the polarizability $\alpha(\omega)$ of equation 2.12 into equation 2.5 the dielectric function $\varepsilon(\omega)$ takes on the form

$$\begin{aligned} \varepsilon(\omega) &= 1 + \frac{Ne^2}{\varepsilon_0 m_e(\omega_0^2 - \omega^2 - i\omega\gamma) - \frac{Ne^2}{3\varepsilon_0 m_e}} = 1 + \frac{Ne^2}{\varepsilon_0 m_e} \frac{1}{(\tilde{\omega}^2 - \omega^2 - i\omega\gamma)} \\ \text{with} \qquad \tilde{\omega}^2 &= \omega_0^2 - \frac{Ne^2}{3m_e\varepsilon_0} \end{aligned} \tag{2.13}$$

So far, the equations for polarizability and dielectric function assume a single resonance frequency. In fact, there are several resonance frequencies caused by the different kinds of vibrations for the components of the crystal. Not all bonds between the atoms are identical, therefore, in the dielectric function all contributions from different vibrations are added according to

$$\varepsilon(\omega) = 1 + \frac{Ne^2}{\varepsilon_0 m_e} \sum_j \frac{f_j}{\tilde{\omega}_j^2 - \omega^2 - i\gamma_j\omega} \tag{2.14}$$

The fractions f_j describe the contributions of the different vibrations and are dimensionless, together with the factor $\frac{Ne^2}{\varepsilon_0 m}$ they constitute the oscillator strengths S_j^2 [19],

$$S_j^2 = f_j \cdot \frac{Ne^2}{\varepsilon_0 m_e}. \tag{2.15}$$

As the measured spectra are wavenumber spectra, the frequencies ω in the dielectric tensor function are substituted by wavenumbers $\tilde{\nu}$. The two definitions with frequency or wavenumber have a different units, making them technically different quantities, but clearly describing the same physics via $\tilde{\nu} = \omega/2\pi c$. The real part $\mathrm{Re}(\varepsilon(\tilde{\nu}))$ and imaginary part $\mathrm{Im}(\varepsilon(\tilde{\nu}))$ are given by

$$\begin{aligned} \mathrm{Re}(\varepsilon(\tilde{\nu})) &= 1 + \frac{S_j^2(\tilde{\nu}_j^2 - \tilde{\nu}^2)}{(\tilde{\nu}_j^2 - \tilde{\nu}^2) + \gamma_j^2\tilde{\nu}^2} \\ \mathrm{Im}(\varepsilon(\tilde{\nu})) &= \frac{\gamma_j \tilde{\nu}_j S_j^2}{(\tilde{\nu}_j^2 - \tilde{\nu}^2) + \gamma_j^2\tilde{\nu}^2}. \end{aligned} \tag{2.16}$$

Fig. 2.1 shows the typical form of $\mathrm{Re}(\varepsilon(\tilde{\nu}))$ and $\mathrm{Im}(\varepsilon(\tilde{\nu}))$ according to equation **??** for a resonance wavenumber of 500 cm^{-1}, oscillator strength S=200 cm^{-1} and damping constant γ=10 cm^{-1}. The imaginary part correlates to the absorption coefficient of a sample [20]. The imaginary part has the form of a resonance curve and is only in the vicinity of the resonance wavenumber $\tilde{\nu}$ significantly different from zero. The width of the resonance curve depends on the oscillator strength S, whereas the damping constant γ determines the relative width (ratio of intensity to width). For a small damping constant the first zero point of $\mathrm{Re}(\varepsilon(\tilde{\nu}))$ is approximately at $\tilde{\nu}$. Outside the region of resonance for optical transparent crystals the index of refraction n is the square root of the real part [20].

From the isotropic expression of equation 2.14 the generalized form is derived, which is valid for *all* crystal systems. The generalized *dielectric tensor function* $\varepsilon_{x,y,z}(\tilde{\nu})$ includes an additional angle dependent matrix to describe the orientation of a transition moment, and the dielectric background ε_∞ that is caused by oscillators located at higher wavenumber regions than the spectral region of interest. The dielectric background

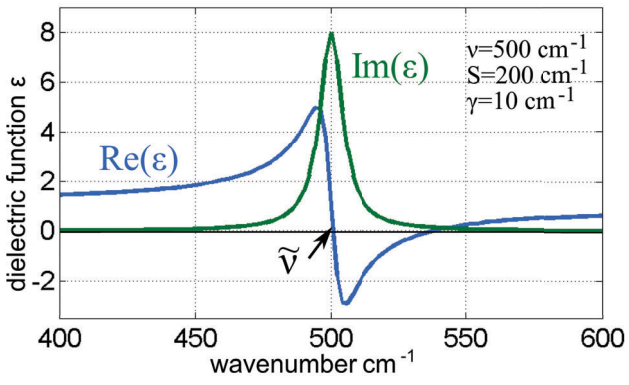

Fig. 2.1. Real part (blue) and imaginary part (green) for the dielectric function in a periodic electric field according to the Lorentz oscillator model.

acts as a constant offset that increases the reflectivity in the IR spectral region.

$$\varepsilon_{x,y,z}(\tilde{\nu}) = \begin{pmatrix} \varepsilon_{\infty,xx} & \varepsilon_{\infty,xy} & \varepsilon_{\infty,xz} \\ \varepsilon_{\infty,yx} & \varepsilon_{\infty,yy} & \varepsilon_{\infty,yz} \\ \varepsilon_{\infty,zx} & \varepsilon_{\infty,zy} & \varepsilon_{\infty,zz} \end{pmatrix} + \sum_{j=1}^{N} \underbrace{\frac{S_j^2}{(\tilde{\nu}_j^2 - \tilde{\nu}^2) - i\gamma_j\tilde{\nu}}}_{\text{Lorentz oscillator}} \times \begin{pmatrix} \sin^2\Theta_j\cos^2\Phi_j & \sin^2\Theta_j\sin\Phi_j\cos\Phi_j & \sin\Theta_j\cos\Theta_j\cos\Phi_j \\ \sin^2\Theta_j\sin\Phi_j\cos\Phi_j & \sin^2\Theta_j\sin^2\Phi_j & \sin\Theta_j\cos\Theta_j\sin\Phi_j \\ \sin\Theta_j\cos\Theta_j\cos\Phi_j & \sin\Theta_j\cos\Theta_j\sin\Phi_j & \cos^2\Theta_j \end{pmatrix} \tag{2.17}$$

The sum runs over all j contributing oscillators. In this generalized form the degenerate oscillators are counted according to the degree of degeneracy, a twofold degenerate vibration contributes two oscillators to the sum, a threefold degenerate vibration contributes three oscillators to the sum. The oscillator parameters remain the resonance wavenumber $\tilde{\nu_j}$, the oscillator strength S_j and the damping constant γ_j. The angles Φ_j and Θ_j are defined in spherical coordinates and describe the orientation of the transition moment creating a certain vibration. The angle dependent matrix will be abbreviated as $\mathbf{M}(\Phi_j, \Theta_j)$ in the further equations. The orientation angles of the transition moments are characteristic for a certain crystal classes since the crystal class determines the distribution of the transition moments. The arrangement of transition moments in turn allow to conclude to the crystal class.

To calculate the dielectric tensor function from the measured reflection spectra, the introduction of two coordinate systems is necessary: the laboratory coordinate system of the spectrometer (X, Y, Z) describes the external coordinate system, the crystal coordinate system (x, y, z) describes the internal coordinate system and is fixed within the crystal, as is illustrated in fig. 2.2. So the matrix $\mathbf{M}(\Phi_j, \Theta_j)$ describes the orientation of a transition moment relative to the internal coordinate system. The crystal coordinate system (x, y, z) is rotated as the crystal cube is rotated within the spectrom-

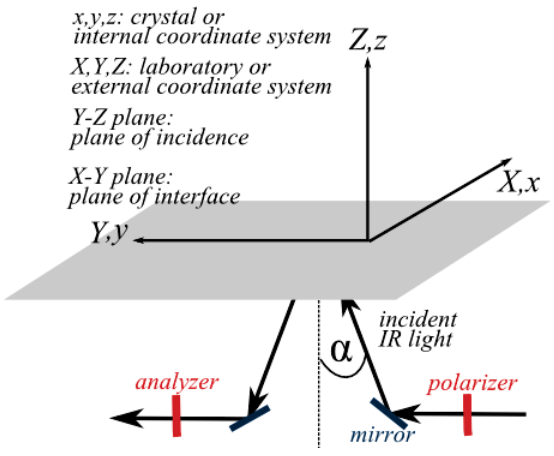

Fig. 2.2. Employed coordinate systems for the evaluation scheme: (X, Y, Z) laboratory or external coordinate system, (x, y, z) crystal or internal coordinate system. The plane of incidence is given by the Y-Z-plane, the plane of interface is constituted by the X-Y-plane. The polarizer is necessary for all measurements, the analyzer was used for only two crystal systems.

eter. The laboratory coordinate system (X, Y, Z) is defined by the plane of incidence (X-Z plane), and the plane of interface between crystal and incidence medium (X-Y plane). The laboratory coordinate system remains unchanged as the cube is rotated. Accordingly, p-polarized incident light is polarized parallel to the Y-Z plane and s-polarized incident light is polarized parallel to the X-Y plane. The incidence angle for all measurements was 8°, for a small incidence angle like that for p-polarized incident light the contribution of the polarization component normal to the plane of interface is negligible.
As the crystal is rotated within the spectrometer, also the internal coordinate system is rotated. Due to the rotation of the internal coordinate system a coordinate transformation has to be performed. The transformation can be performed by describing the rotation with a rotation matrix A:

$$\varepsilon_{X,Y,Z}(\tilde{\nu}) = A(\varphi, \theta, \psi) \cdot \varepsilon_{x,y,z}(\tilde{\nu}) \cdot A^{-1}(\varphi, \theta, \psi) \tag{2.18}$$

The rotation matrix A is a function of the Euler angles φ, θ and ψ with

$$\begin{aligned} A(\varphi, \theta, \psi) &= A(\varphi) \cdot A(\theta) \cdot A(\psi) \\ &= \begin{pmatrix} \cos\theta\cos\varphi\cos\psi - \sin\varphi\sin\psi & \cos\theta\cos\psi\sin\varphi + \cos\varphi\sin\psi & -\cos\psi\sin\theta \\ -\cos\psi\sin\varphi - \cos\theta\cos\varphi\sin\psi & \cos\varphi\cos\psi - \cos\theta\sin\varphi\sin\psi & \sin\theta\sin\psi \\ \cos\varphi\sin\theta & \sin\theta\sin\varphi & \cos\theta \end{pmatrix} \end{aligned} \tag{2.19}$$

and

$$\begin{aligned} A(\varphi) &= \begin{pmatrix} \cos\varphi & \sin\varphi & 0 \\ -\sin\varphi & \cos\varphi & 0 \\ 0 & 0 & 1 \end{pmatrix}, \quad A(\theta) = \begin{pmatrix} \cos\theta & 0 & \sin\theta \\ 0 & 1 & 0 \\ \sin\theta & 0 & \cos\theta \end{pmatrix}, \\ A(\psi) &= \begin{pmatrix} \cos\psi & \sin\psi & 0 \\ -\sin\psi & \cos\psi & 0 \\ 0 & 0 & 1 \end{pmatrix}. \end{aligned} \tag{2.20}$$

In equation (2.19) the rotation matrix $A(\varphi)$ describes a rotation around the Z-axis of the laboratory coordinate system, the matrix $A(\theta)$ a rotation around the Y-axis and the matrix $A(\psi)$ again a rotation around the Z-axis (as all the different possibilities to perform a rotation in three dimensional space are equivalent [21, 22], the present form of the matrix A has no special reason). To calculate the reflectivity of the measured spectra we assume a plane wave with wave vector $\vec{k} = k_0(0, \sin(\alpha), \cos(\alpha))^T$ that travels through the incidence medium along the Y-Z plane and falls with incidence angle α onto a crystal surface. Applying the Maxwell equations

$$\nabla \times \vec{E} = i\omega\mu\vec{H} \quad \text{and} \quad \nabla \times \vec{H} = -i\omega\varepsilon\vec{E}$$

with $\vec{E}$ the electric field, $\vec{H}$ the magnetic field and μ_0 the magnetic permeability. The dependence of the field vector $\vec{\Psi} = (E_X, H_Y, E_Y, -H_X)$ in Z-direction is given by

$$\frac{\partial}{\partial Z}\vec{\Psi} = ik_0 D\vec{\Psi} \quad \text{or} \quad \frac{\partial}{\partial Z}\vec{\Psi}\begin{pmatrix} E_X \\ H_Y \\ E_Y \\ -H_X \end{pmatrix} = ik_0 D \begin{pmatrix} E_X \\ H_Y \\ E_Y \\ -H_X \end{pmatrix}. \tag{2.21}$$

The matrix D is called the differential propagation matrix [17]. Under the assumed conditions (non-magnetic and optically inactive medium with arbitrary angle of incidence, and the component $k_x = 0$) the matrix D takes on the following form:

$$D = \begin{pmatrix} 0 & 1 & 0 & 0 \\ k_0^2 \sin^2(\alpha) + \varepsilon_{XX} - \frac{\varepsilon_{XZ}^2}{\varepsilon_{ZZ}} & 0 & \varepsilon_{XY} - \frac{\varepsilon_{XZ}\varepsilon_{YZ}}{\varepsilon_{ZZ}} & -\frac{k_0 \sin(\alpha)\varepsilon_{XZ}}{\varepsilon_{ZZ}} \\ -\frac{k_0 \sin(\alpha)\varepsilon_{XZ}}{\varepsilon_{ZZ}} & 0 & -\frac{k_0 \sin(\alpha)\varepsilon_{YZ}}{\varepsilon_{ZZ}} & 1 - \frac{k_0^2 \sin^2(\alpha)}{\varepsilon_{ZZ}} \\ \varepsilon_{XY} - \frac{\varepsilon_{XZ}\varepsilon_{YZ}}{\varepsilon_{ZZ}} & 0 & \varepsilon_{YY} - \frac{\varepsilon_{YZ}^2}{\varepsilon_{ZZ}} & -\frac{k_0 \sin(\alpha)\varepsilon_{YZ}}{\varepsilon_{ZZ}} \end{pmatrix} \tag{2.22}$$

Equation (2.21) describes an eigenvalue problem, which can be solved by finding the eigenvalues of the differential propagation matrix (2.22). For this, the determinant equation $Det(D - \gamma \cdot \mathbf{I}) = 0$ must be solved, wherein $\mathbf{I}$ represents the 4×4 identity matrix and γ_i the four eigenvalues of the propagation matrix. Of the four eigenvalues two describe a forward traveling wave and the other two describe the backward traveling wave, which would be a wave reflected on the interface crystal-incidence medium after having traveled through the crystal. The eigenvalues for the forward traveling wave are either real valued or have a positive imaginary part, the eigenvalues for the backward traveling wave are complex with a negative imaginary part. Due to the assumption of a semi-infinite medium only the eigenvalues describing the forward traveling wave are selected. With the two eigenvectors Ψ_I and Ψ_{II} resulting from the selected eigenvalues the dynamical matrix of the crystal $D_{crystal}$ is built. The second and fourth column that describe the backward traveling wave are zero in this case.

$$D_{crystal} = \begin{pmatrix} \Psi_{I,1} & 0 & \Psi_{II,1} & 0 \\ \Psi_{I,2} & 0 & \Psi_{II,2} & 0 \\ \Psi_{I,3} & 0 & \Psi_{II,3} & 0 \\ \Psi_{I,4} & 0 & \Psi_{II,4} & 0 \end{pmatrix} = \begin{pmatrix} E_{X,s} & 0 & E_{X,p} & 0 \\ H_{Y,s} & 0 & H_{Y,p} & 0 \\ E_{Y,s} & 0 & E_{Y,p} & 0 \\ -H_{X,s} & 0 & -H_{X,p} & 0 \end{pmatrix} \tag{2.23}$$

The indices s and p describe the polarization state of the $\vec{E}$ and $\vec{H}$ fields. The amplitudes of the incident (A_s, A_p), reflected (B_s, B_p) and transmitted (C_s, C_p) wave are linked by the dynamical matrix of the crystal and the (inverse) dynamical matrix D_{inc}

of the incidence medium:

$$D_{inc}^{-1} = \begin{pmatrix} 1 & \frac{1}{\cos\alpha} & 0 & 0 \\ 1 & -\frac{1}{\cos\alpha} & 0 & 0 \\ 0 & 0 & \frac{1}{\cos\alpha} & 1 \\ 0 & 0 & \frac{1}{\cos\alpha} & -1 \end{pmatrix} \tag{2.24}$$

The first quadrant of the dynamical matrix D_{inc} in (2.24) describes the dynamical matrix of a p-polarized wave, the fourth quadrant donates the matrix of a s-polarized wave. The matrix $M = D_{inc}^{-1} \cdot D_{crystal}$ is the matrix that links the amplitudes of incidence, reflected and transmitted wave [23]

$$\begin{pmatrix} A_s \\ B_s \\ A_p \\ B_p \end{pmatrix} = D_{inc}^{-1} \cdot D_{crystal} \cdot \begin{pmatrix} C_s \\ 0 \\ C_p \\ 0 \end{pmatrix} = \begin{pmatrix} M_{11} & M_{12} & M_{13} & M_{14} \\ M_{21} & M_{22} & M_{23} & M_{24} \\ M_{31} & M_{32} & M_{33} & M_{34} \\ M_{41} & M_{42} & M_{43} & M_{44} \end{pmatrix} \cdot \begin{pmatrix} C_s \\ 0 \\ C_p \\ 0 \end{pmatrix} \tag{2.25}$$

with

$$M = \begin{pmatrix} \Psi_{I,1} + \frac{\Psi_{I,2}}{\cos\alpha} & 0 & \Psi_{II,1} + \frac{\Psi_{II,2}}{\cos\alpha} & 0 \\ \Psi_{I,1} - \frac{\Psi_{I,2}}{\cos\alpha} & 0 & \Psi_{II,1} - \frac{\Psi_{II,2}}{\cos\alpha} & 0 \\ \frac{\Psi_{I,3}}{\cos\alpha} + \Psi_{I,4} & 0 & \frac{\Psi_{II,3}}{\cos\alpha} + \Psi_{II,4} & 0 \\ \frac{\Psi_{I,3}}{\cos\alpha} - \Psi_{I,4} & 0 & \frac{\Psi_{II,3}}{\cos\alpha} - \Psi_{II,4} & 0 \end{pmatrix}. \tag{2.26}$$

From equation (2.25) and (2.26) explicit expressions for the reflection coefficients matrix $\mathbf{r}$ of the calculated spectra for different polarization states of the incoming light can be derived. The reflection coefficients are given by

$$\mathbf{r} = \begin{pmatrix} r_{ss} & r_{sp} \\ r_{ps} & r_{pp} \end{pmatrix} = \frac{1}{d} \cdot \begin{pmatrix} M_{21}M_{33} - M_{23}M_{31} & M_{41}M_{33} - M_{43}M_{31} \\ M_{11}M_{23} - M_{21}M_{13} & M_{11}M_{43} - M_{41}M_{13} \end{pmatrix}. \tag{2.27}$$

with the abbreviation d for the denominator

$$d = \frac{1}{M_{11}M_{33} - M_{13}M_{31}}$$

The first index of the reflection coefficients r_{ij} in equation (2.27) describes the polarization state of the incoming light. The second index describes the transmission direction of the analyzer relative to the plane of incidence. The measured quantity is the reflectivity R and is calculated by

$$R = r \cdot r^* \tag{2.28}$$

with r^* the complex conjugate. If the reflection spectra are measured with both the polarizer and an analyzer they are called cross polarization spectra. The reflectivity is

also labeled with the indices "s" and "p", e.g. R_{sp} or R_{ps}, the first index describes the transmission direction of the polarizer, the second index describes the transmission direction of the analyzer, in relation to the plane of incidence. If the spectrum is recorded with the sole polarizer the reflectivity is indicated by R_s or R_p. These spectra are called one polarizer spectra. As with only one polarizer all polarization directions of the reflected light are detected, the reflectivity R_s and R_p is calculated by

$$R_s = R_{ss} + R_{sp} \qquad \text{and} \qquad R_p = R_{ps} + R_{pp}. \tag{2.29}$$

The quantities R_s, R_p, R_{sp} and R_{ps} now get fitted by an optimization routine described in chapter 2.8 to reproduce the measured spectra and therefore to find the dielectric function.

2.2 Characteristics of reflection bands

In contrary to symmetric bands like Raman bands, which can be approximated by a Gauss- or Voigt-profile, the reflectivity of an IR spectrum is calculated via the dielectric tensor function. For a Gaussian shaped band the wavenumber of highest intensity is the central wavenumber, and the intensity is more or less equal to the area implied by the band. As there is a complex dependency between the dielectric tensor function and the reflectivity, the reflectivity does not allow to conclude directly to the dielectric tensor function and therefore to the parameters of the contributing oscillators. The reflection band is not directly fitted by the damped Lorentz oscillators, the shape of the fitted reflectivity is created by the dielectric tensor function.

Fig. 2.3 shows the reflection band created by an oscillator with resonance wavenumber $\tilde{\nu}$=100 cm^{-1} and damping constant γ=30 cm^{-1} with different strengths from 100-1000 cm^{-1}. The dielectric background was set to 1.5. The stronger the oscillator is,

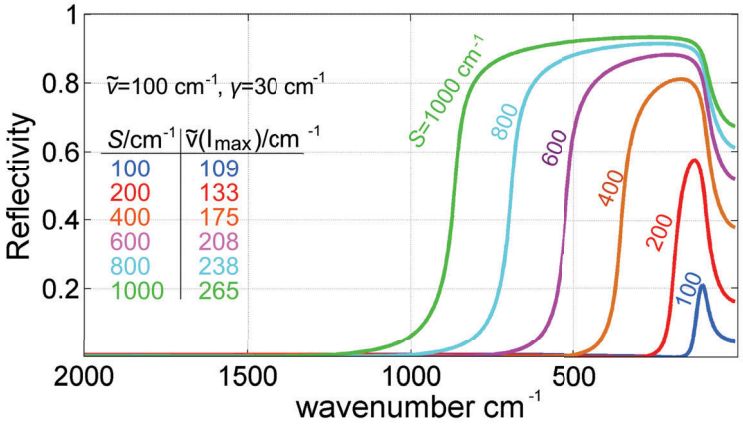

Fig. 2.3. Wavenumber of highest reflected intensity $\tilde{\nu}(I_{max})$ and band shape in dependency of the oscillator strength for a given resonance wavenumber.

the more shifted is the wavenumber of the highest reflected intensity $\tilde{\nu}(I_{max})$ compared to the resonance wavenumber of the oscillator. Also, the higher the oscillator strength is, the broader the reflection band gets. So the width of the band is not given by the damping constant, but by the strength.

Fig. 2.4 shows the form of a reflection band created by an oscillator with resonance wavenumber $\tilde{\nu}$=900 cm^{-1}, strength S=500 cm^{-1} and damping constant γ=30 cm^{-1} in dependency of the dielectric background. The dielectric background is the asymptotic value in the higher wavenumber region due to oscillators located at higher wavenumbers than the region of interest. The tail of the reflection band in the lower wavenumber region is then the dielectric background for the oscillators located in the lower wavenumber region ("new dielectric background" in fig. 2.4). The dielectric background acts like a constant offset to the spectrum. The higher the dielectric background is, the lower is the intensity of the reflection band. The reflection band also becomes narrower, but the higher the dielectric background is, the smaller is the shift between the wavenumber of highest reflected intensity $\tilde{\nu}(I_{max})$ and the given resonance wavenumber.

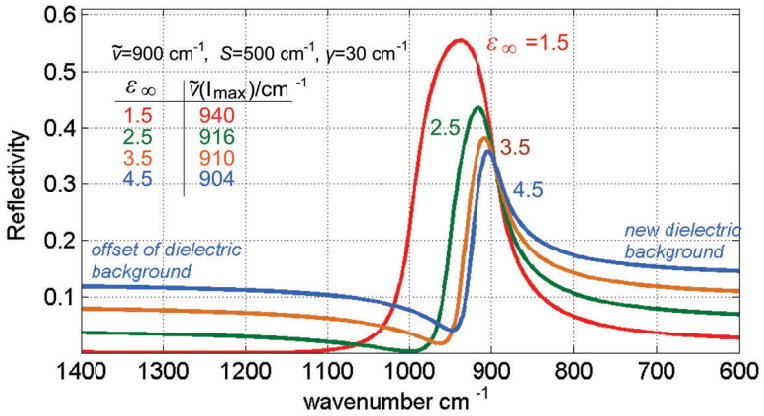

Fig. 2.4. Wavenumber of highest reflected intensity $\tilde{\nu}(I_{max})$ in dependency of the dielectric background. The dielectric background also influenced the width and intensity of the reflection band.

The damping constant determines the ratio of width to intensity. Fig. 2.5 shows the form of the reflection band in dependency of the damping constant for an oscillator with resonance wavenumber of 500 cm^{-1}, a strength of 500 cm^{-1} and different damping constants. The dielectric background is 3.5 in this example. The higher the damping constant is, the lower the intensity gets, whereas the width of the band remains constant. The wavenumber of highest reflectivity $\tilde{\nu}(I_{max})$ shifts from higher values than the resonance wavenumber to values below the resonance wavenumber.

Furthermore, the smaller the damping constant is, the deeper gets the tail of the reflection band at 600 cm^{-1} before reaching the asymptotic value at higher wavenumbers.

Also, oscillators that share the same wavenumber region can seem to have a negative strength by visually interpreting a spectrum. If there is a weak oscillator within the

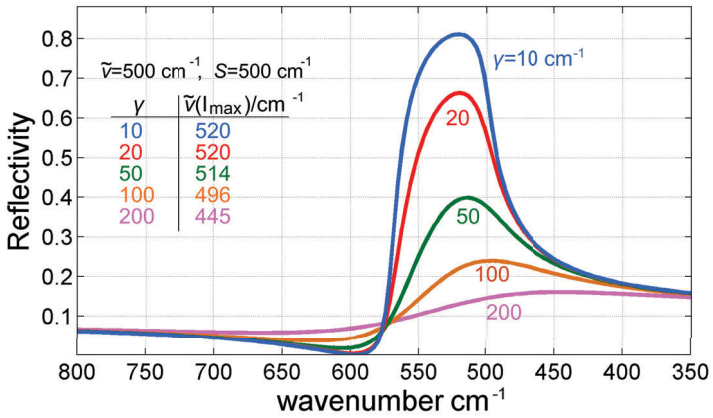

Fig. 2.5. Wavenumber of highest reflected intensity $\tilde{\nu}(I_{max})$ in dependency of the damping constant. The damping constant it influences the depth of the reflection minimum of the tail of the reflection band at $600\,\mathrm{cm}^{-1}$.

wavenumber region of an intense oscillator, the weak oscillator creates a dip in the spectral slope of the strong oscillator due to electromagnetic induced transparency of Fano-resonance [24] (without the weak oscillator the reflectivity of the strong oscillator is close to 100%; the weak oscillator creates a dip and reduces the reflectivity, which is the transparency-effect). The strength of the weak oscillator seems to have a negative value. An example is shown in the left part of fig. 2.6. The deepest point of the dip approximately coincides with the resonance wavenumber of the weak oscillator. This band behavior occurs e.g. in the reflection spectra for quartz or neodymium gallate (chapter 5.2 and 6.2). Likewise, the apparent intensity of an oscillator is frequency dependent, as can be seen in the right part of fig. 2.6, where two oscillators with the same strength and damping constant but different resonance wavenumbers are shown. The oscillator with the lower resonance wavenumber appears with a remarkably higher intensity than the oscillator with the higher resonance wavenumber.

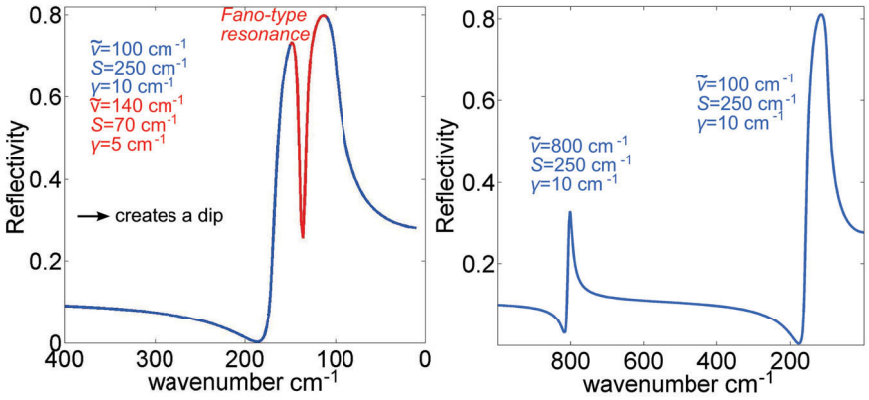

Fig. 2.6. Left: A weak oscillator within the wavenumber region of an intense oscillator creates a dip. Right: The apparent intensities of oscillators is frequency dependent. The oscillator in the lower wavenumber region seems to have a higher intensity than the oscillator in the higher wavenumber region.

2.3 Measurement scheme

To perform dispersion analysis, reflectance spectra from different crystal faces with different polarization states of the incoming light have to be measured. Best possible reflectance and prevention of diffuse reflection is realized by optically polished crystal faces. To ensure that every oscillator is caught carefully, the most appropriate sample form is a cube or cuboid, or only three orthogonal faces that are carved out of the crystal following an idea from Aronson, Emslie and Strong [8]. For convenience, the cut sample is henceforth illustrated as cube. Fig. 2.7 shows the position of the cube in the laboratory (X, Y, Z) and internal coordinate (x, y, z) systems. An exemplary transition moment with the orientation angles Φ and Θ is represented with the red double arrow. For the transition moments double arrows are used as they are orientation dependent but not direction dependent. The faces 1, 2 and 3 are mutual orthogonal faces that are employed for the measurements.
Intuitively, to determine the six independent elements of the dielectric tensor a set of six independent spectra should be sufficient. Such a set of spectra could be measured from the cube shaped sample by employing polarized light with the polarization directions parallel to the cube edges as is illustrated in fig. 2.8. The set with six spectra could be realized e.g. by recording two spectra with different polarization directions of the incoming light of each of three mutually orthogonal cube faces. The polarization states of the incoming light is represented by the blue and red double arrows in fig. 2.8. Another set of six spectra could comprise three spectra recorded with the polarization direction of the incident light parallel to three mutually orthogonal cube edges and three mutually orthogonal cube face diagonals. The reflection spectra of $K_2Cr_2O_7$ for example were tried to be fitted using the latter spectra set, but it turned out that all in all the agreement between measured and fitted spectra was not satisfying.

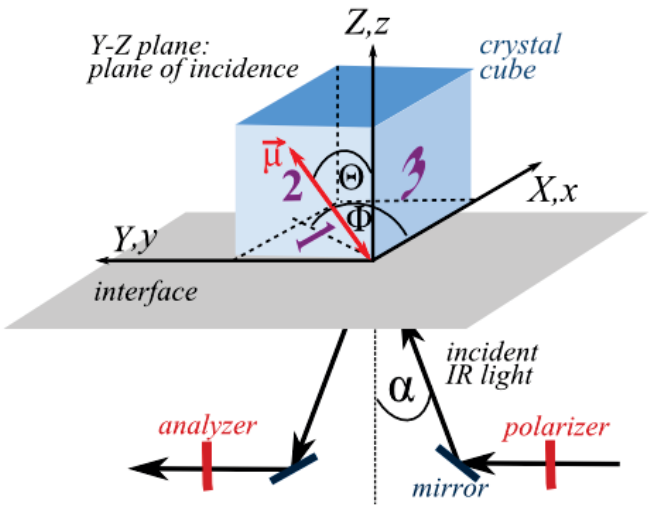

Fig. 2.7. Orientation of the crystal cube with respect to the external and internal coordinate system. Cube face 1 is defined by the x-y-plane, cube face 2 by the y-z-plane and cube face 3 is given by the x-z-plane. The polarizer is placed in front of the sample holder, the analyzer is mounted in front of the detector.

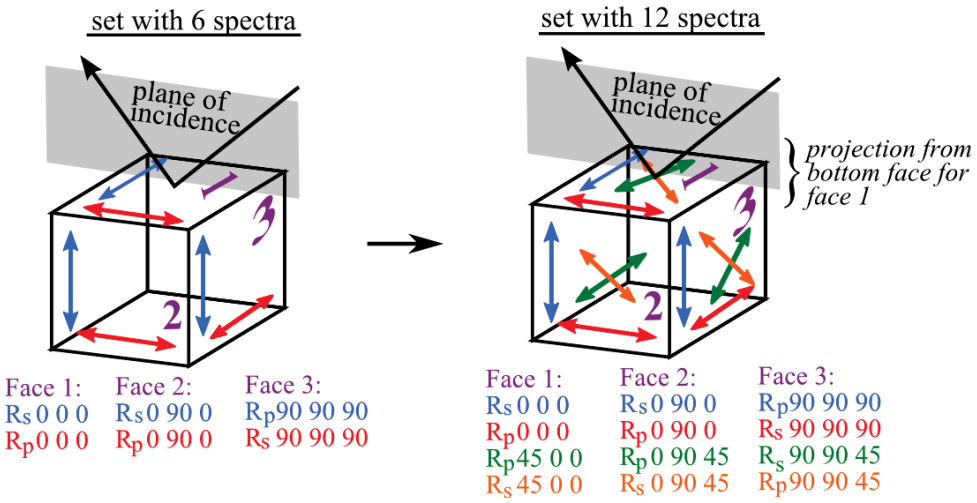

Fig. 2.8. Possible spectra sets that can be employed to perform dispersion analysis. Left: A set of spectra containing only 6 reflectance spectra leads to ambiguities concerning the orientation angles of the oscillators. Right: A set of 12 spectra including spectra that are recorded with polarization direction of the incident light parallel to the cube face diagonals removes the ambiguities. For the measurements face 1 is the bottom face, but for illustration purposes it is projected to the top face.

Experience showed that six spectra are not sufficient to yield reliable results for dispersion analysis. There exist different angle combinations for oscillators that generate the same reflection bands. To differentiate between the angle combinations that cause the same reflection band in the spectra, a second set of spectra is employed. The second spectra set is recorded with the polarization direction of the incoming light parallel to the cube face diagonals, as is shown fig. 2.8, right. The final set of 12 spectra includes four spectra of three mutual orthogonal cube faces. Of the four spectra two are recorded with polarization direction of the incoming light parallel to the cube edges and two spectra are recorded with the polarization direction parallel to the cube face diagonals.

The corresponding scheme to address all crystal faces is proposed in fig. 2.9. To distinguish between the different orientations the spectra are named according to a nomenclature that refers to the polarization state of the incident light and actual rotation applied to the cube. Each of the six orientations is employed twice, one spectrum is recorded with p-polarized (R_p-spectrum) and one spectrum is recorded with s-polarized incident light (R_s-spectrum). The coordinate axes drawn in orange represent the orientation of the internal coordinate system for each rotation. The dashed black lines represent the axes of the laboratory coordinate system (which are not rotated). The axes are drawn in a solid black line if an axis of the laboratory coordinate system coincides with an axis of the internal coordinate system. To switch from a spectrum recorded with s-polarized light to a spectrum recorded with p-polarized light the polarizer is rotated (instead of the cube). To obtain e.g. orientation 0 90 0 the cube is

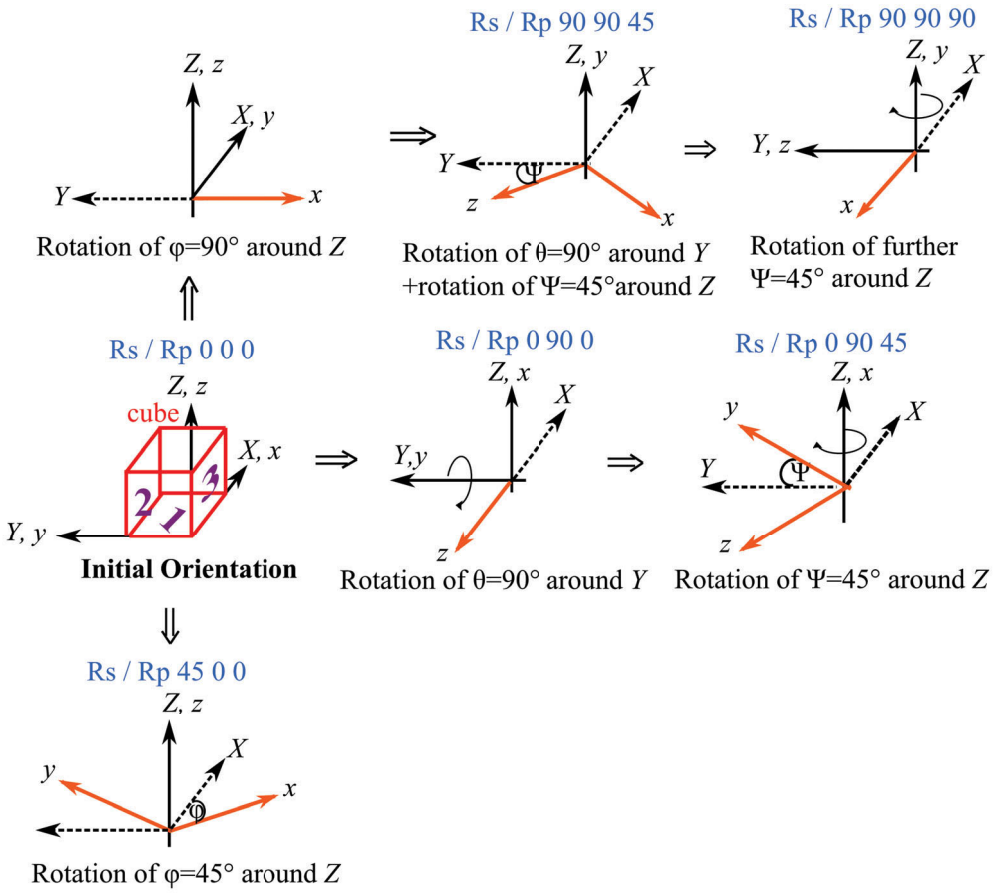

Fig. 2.9. Rotation scheme to address all 12 spectra that are necessary to perform dispersion analysis. All six different rotations are realized by a combination of rotations around the Y- and Z-axis. Each rotation two spectra with s-and p-polarization are recorded, respectively.

rotated around Y by 90° outgoing from the initial position. Likewise, orientation 90 90 90 is obtained by rotating the cube clockwise around Z by 90°, then by rotating clockwise by 90°around Y and finally rotating it around Z again by 90°, also starting from the initial position.

If, for example, an oscillator has the orientation angles (Φ, Θ)=(20°,110°) and if only the spectra of the cube edges (R_s 0 0 0, R_p 0 0 0, R_s0 90 0, R_p 0 90 0, R_s 90 90 90 and R_p 90 90 90) and R_p 0 90 45 are measured, one can not distinguish between (Φ, Θ)=(20°,110°) and (Φ, Θ)=(-20°,-110°) as the band originating from this oscillator looks very similar in the mentioned spectra. For another oscillator with e.g. (Φ, Θ)=(-30°,60°), one could not distinguish between (Φ, Θ)=(-30°,60°) and (Φ+90°, Θ+90°)=(60°,150°) if only the spectra R_s 0 90 45, R_p 0 90 0 and R_s 45 0 0 are measured. Therefore, it is advisable to perform dispersion analysis with the complete set of 12 spectra. Nevertheless, the performance of the fit employing all 12 spectra does not constitute an increased computing effort as by the formalism described in this chapter always all 12 spectra are calculated.

2.4 Crystal systems

A crystal is defined as a three dimensional periodic arrangement of atoms, ions or molecules [25]. This periodic arrangement guarantees the long range order within the crystal, also, the periodic arrangement is always anisotropic, as for different directions identical points have different distances. The consequence of the periodic anisotropic arrangement is intrinsic birefringence for *all* crystals (cubic crystals are only isotropic in the VIS and IR spectral region. Anisotropy becomes relevant for the UV and x-ray spectral region). Every crystal can be described by one of the seven crystal systems, whose unit cell is described by the crystallographic axes a, b, c and the angles between the axes α, β, γ. The unit cell is the smallest unit.
Geometrically, there exists an infinite number of possible unit cells, though the unit cell is defined as the cell with the smallest possible volume. The unit cell plus the atoms belonging to it is called the *base*. There must be distinguished between two terms; all the identical points of a crystal form the elementary grid, and the three dimensional arrangement of the atoms itself. The elementary grid does not comprise any atoms, it is an abstraction of the crystal structure, cf. fig. 2.10. Within the unit cell, an atom can have different symmetry dependent positions. These positions are called the Wyckoff positions and are listed in the International Tables of Crystallography, A [26]. The symmetry of a crystal with a certain arrangement of atoms described by the Wyckoff positions is called the *space group*. All in all, there exist 230 different space groups, which consider point group and translational symmetries that are possible for the symmetry of that crystal system. The orientation angles Φ and Θ of the transition moments are determined by the crystal system. Therefore, the dielectric function takes on a characteristic form for each of the crystal system.

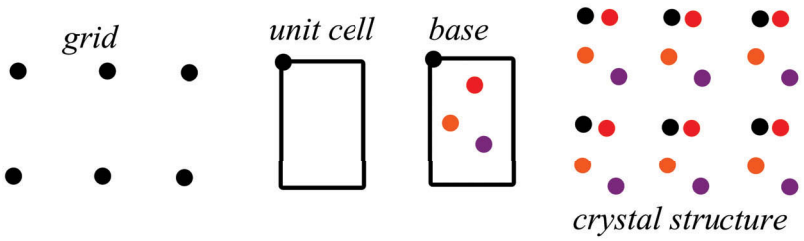

Fig. 2.10. Components of crystal structure: grid, unit cell and base.

Cubic crystal class

Due to crystal symmetry all cuts of a **cubic** crystal are a principal cut. Therefore cubic crystals were not investigated in this work. But to complete the crystal classes the cubic system is also introduced here. In the cubic crystal class all three crystal axes are of equal length, the angles between the axes are 90° (cf. fig. 2.11).

It is the crystal system with the simplest unit cell and highest symmetry. The dielectric tensor function is independent of the direction in the crystal, so the function is of diagonal form with three equal principal elements. All off-diagonal elements are generally zero. Each vibration is threefold degenerate, the IR-reflection spectra show isotropic behavior. In fig. 2.11 the transition moments of a threefold degenerate vibration are represented by three equally colored arrows. The orientation of a threefold degenerate oscillator triple is arbitrarily as the triplet describes a high symmetric vibration. For a single reflection spectrum of a cubic crystal the dielectric tensor function is calculated by

$$\varepsilon_{x,y,z}(\tilde{\nu}) = \varepsilon_\infty + \sum_{t=1}^{N} \frac{S_t^2}{(\tilde{\nu}_t^2 - \tilde{\nu}^2) - i\gamma_t\tilde{\nu}} \tag{2.30}$$

with t the sum over all oscillators occurring in this spectrum. The dielectric function for a cubic crystal can also be expressed with the generalized dielectric function of equation 2.17.

$$\varepsilon_{x,y,z}(\tilde{\nu}) = \begin{pmatrix} \varepsilon_{\infty,xx} & 0 & 0 \\ 0 & \varepsilon_{\infty,xx} & 0 \\ 0 & 0 & \varepsilon_{\infty,xx} \end{pmatrix} + \sum_{j=1}^{N} \frac{S_j^2}{(\tilde{\nu}_j^2 - \tilde{\nu}^2) - i\gamma_j\tilde{\nu}} \cdot \mathbf{M}(\Phi_j, \Theta_j)$$

In the generalized form the index j is 3 times the index t of equation 2.30, since every vibration is threefold degenerate. The three oscillators of a threefold degenerate vibration have the same resonance wavenumber, strength and damping constant, but the angles Φ_j and Θ_j are fixed in a way that each triple of degenerate oscillators is mutually orthogonal.

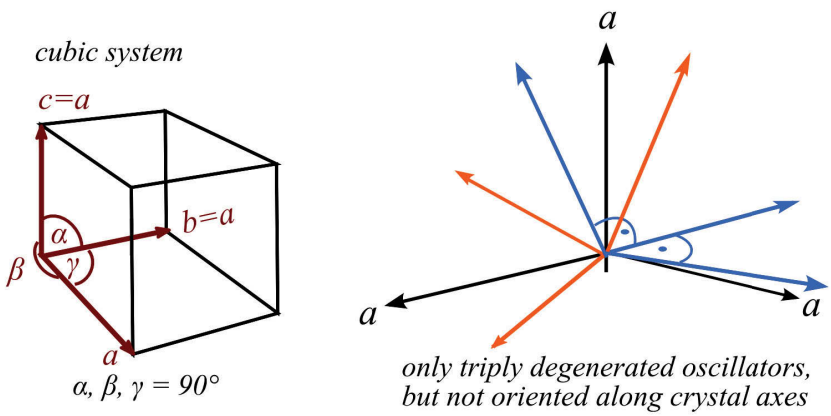

Fig. 2.11. Left: unit cell for a cubic crystal. Right: distribution of transition moments, represented by the arrows.

Uniaxial crystals

In the **uniaxial** crystal classes the symmetry is reduced compared to the symmetry of the cubic crystal class. The uniaxial crystal classes include the **hexagonal**, **trigonal** and **tetragonal** class. In these crystal systems two axes are of equal length, $a = b$, the c-axis is set as the optical axis by definition. The angle between two a-axes is 120° for the trigonal and hexagonal crystal systems and 90° for the tetragonal crystal class. The unit cells and distribution of transition moments for uniaxial crystals are shown in fig. 2.12. The three uniaxial crystal classes show identical infrared behavior as there exist only two distinct principal optical directions: one direction is parallel to the c-axis and the other is *any* direction perpendicular to c. All directions perpendicular to c are equivalent [27]. In consequence, there exist one class of non-degenerate vibrations, whose transition moments are oriented parallel to the c-axis and a second class of degenerate vibrations, whose transition moments are oriented on a plane normal to the c-axis. Therefore, as all directions normal to the c-axis are equivalent, the orientations of the a-axes of the uniaxial crystals remain undetermined by dispersion analysis.
The two transition moments of a twofold degenerate vibration have the same values for resonance wavenumber, strength and damping constant and are perpendicular to each other. Therefore if the orientation of the crystal is known, to perform dispersion analysis two reflection spectra are sufficient. If the crystal face parallel to the c-axis is framed by an edge parallel and normal to the c-axis, respectively, this configuration is called a principal cut. Then one spectrum with polarization direction of the incoming light parallel and one spectrum with the polarization direction normal to the c-axis has to be recorded. The spectra should be recorded with s-polarized light with the optical axis oriented parallel or normal to the polarization direction of the incoming light to ensure that only one principal component is probed.

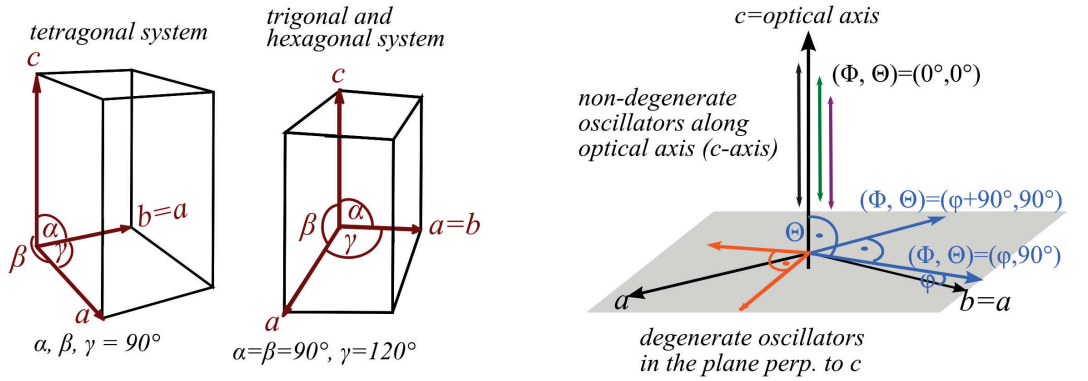

Fig. 2.12. Left: unit cell for a tetragonal crystal. Middle: unit cell for the trigonal and hexagonal crystals (in hexagonal setting) with. Right: The non-degenerate oscillators are oriented parallel to the optical axis, the degenerate oscillators are oriented on a plane normal to the optical axis.

In this configuration the two measured spectra are independent and the dielectric tensor function takes on diagonal form with two equal principal elements $\varepsilon_\perp$ that describe the dielectric tensor function perpendicular to the optical axis. The other principal element $\varepsilon_{||}$ describes the dielectric tensor function parallel to the optical axis. For the two independent spectra the dielectric tensor function is calculated separately according to

$$\begin{aligned} \varepsilon_\perp &= \varepsilon_{\infty,\perp} + \sum_{t=1}^{N} \frac{S_t^2}{(\tilde{\nu}_t^2 - \tilde{\nu}^2) - i\gamma_t\tilde{\nu}} \\ \varepsilon_{||} &= \varepsilon_{\infty,||} + \sum_{g=1}^{N} \frac{S_g^2}{(\tilde{\nu}_g^2 - \tilde{\nu}^2) - i\gamma_g\tilde{\nu}}. \end{aligned} \tag{2.31}$$

The expression for the generalized dielectric function has the form

$$\varepsilon_{x,y,z}(\tilde{\nu}) = \begin{pmatrix} \varepsilon_{\infty,\perp} & 0 & 0 \\ 0 & \varepsilon_{\infty,\perp} & 0 \\ 0 & 0 & \varepsilon_{\infty,||} \end{pmatrix} + \sum_{j=1}^{N} \frac{S_j^2}{(\tilde{\nu}_j^2 - \tilde{\nu}^2) - i\gamma_j\tilde{\nu}} \cdot \mathbf{M}(\Phi_j, \Theta_j)$$

The orientation angles of the angle matrix $\mathbf{M}(\Phi_j, \Theta_j)$ are (Φ, Θ)=(0°, 0°) for the oscillators parallel to the c-axis, and (Φ, Θ)=(φ, 90°) and (Φ, Θ)=(φ+90°, 90°) for a degenerate oscillator pair. The angle φ is different for each oscillator pair. The index j is now $j = 2t + g$ as the twofold degenerate oscillators normal to the c-axis are counted twice.

Biaxial crystals

The crystal classes with even more reduced symmetry are the biaxial crystals, namely the **orthorhombic**, **monoclinic** and **triclinic** crystal classes. In all three crystal classes the crystallographic axes are of different length, therefore all vibrations are non-degenerate.

In the **orthorhombic** system the angle between the axes is 90°, the dielectric axes (principal axes of the dielectric tensor function) coincide with the crystal axes a, b, c. Accordingly, three spectra are sufficient to perform dispersion analysis if the spectra are recorded with s-polarized incident light with the crystal axes oriented parallel to the polarization direction of the incoming light, respectively. A suitable sample could be realized by a cube of that crystal with the cube edges oriented parallel to the crystal axes, which is the principal cut of an orthorhombic crystal. These orientations of the crystal guarantee that the dielectric tensor takes on diagonal form while the polarization of the light ensures that only one principal component of the tensor is probed. Fig 2.13 shows the unit cell and orientation of transition moments for an

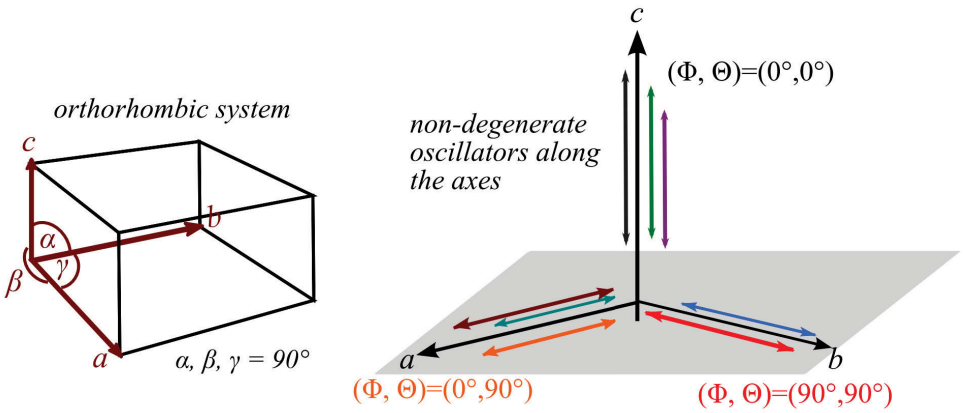

Fig. 2.13. Left: unit cell for an orthorhombic crystal. Right: distribution of transition moments, the non-degenerate oscillators are oriented parallel to the crystal axes.

orthorhombic crystal. For each of the three independent spectra the dielectric tensor function $\varepsilon_{||a,b,c}$ is computed individually by

$$\begin{aligned}
\varepsilon_{||a} &= \varepsilon_{\infty,a} + \sum_{g=1}^{N} \frac{S_g^2}{(\tilde{\nu}_g^2 - \tilde{\nu}^2) - i\gamma_g\tilde{\nu}} \\
\varepsilon_{||b} &= \varepsilon_{\infty,b} + \sum_{t=1}^{N} \frac{S_t^2}{(\tilde{\nu}_t^2 - \tilde{\nu}^2) - i\gamma_t\tilde{\nu}} \\
\varepsilon_{||c} &= \varepsilon_{\infty,c} + \sum_{n=1}^{N} \frac{S_n^2}{(\tilde{\nu}_n^2 - \tilde{\nu}^2) - i\gamma_n\tilde{\nu}}.
\end{aligned} \tag{2.32}$$

In the generalized form the sum runs over all the oscillators parallel to each crystal axis. The summation index j is now $j = g + t + n$.

$$\varepsilon_{x,y,z}(\tilde{\nu}) = \begin{pmatrix} \varepsilon_{\infty,||a} & 0 & 0 \\ 0 & \varepsilon_{\infty,||b} & 0 \\ 0 & 0 & \varepsilon_{\infty,||c} \end{pmatrix} + \sum_{j=1}^{N} \frac{S_j^2}{(\tilde{\nu}_j^2 - \tilde{\nu}^2) - i\gamma_j\tilde{\nu}} \cdot \mathbf{M}(\Phi_j, \Theta_j)$$

The orientation angles are (Φ, Θ)=(0°, 0°) for the oscillators parallel to the c-axis, (Φ, Θ)=(0°, 90°) for the oscillators parallel to the a-axis and (Φ, Θ)=(90°, 90°) for the oscillators parallel to the b-axis if the crystal is oriented as shown in fig. 2.13.
In the **monoclinic** system two angles are still 90°, the angle β is $> 90°$. Fig. 2.14 shows the unit cell and distribution of transition moments for a monoclinic crystal. The only symmetry axis is defined as the b-axis. The oscillators are oriented either parallel to the b-axis or on a plane normal to the b-axis. Dispersion analysis of monoclinic crystal can be performed with four spectra if one spectrum is recorded with the polarization direction of the incoming light parallel to the b-axis and three spectra are recorded

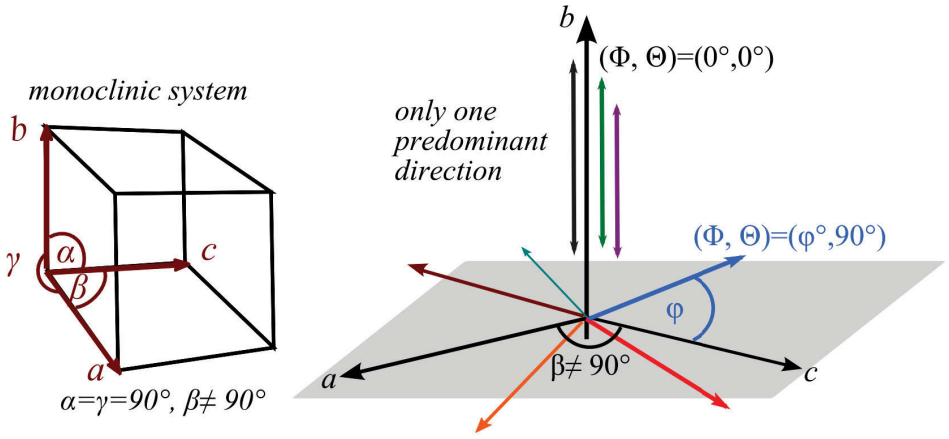

Fig. 2.14. Left: unit cell for a monoclinic crystal. Right: distribution of transition moments. In the monoclinic system the b-axis is the only symmetry axis and therefore only predominant direction. One group of oscillators is oriented parallel to the b-axis, the other group of oscillators is oriented on the a-c plane.

with the polarization direction of the incoming light perpendicular to the b-axis [28]. The spectra also should be measured with s-polarized light to avoid the excitation of transition moments of the other orientation. In this setup the dielectric tensor function takes on block-diagonalized form consisting of a 2×2 matrix and a single element [28]. The single element is determined with the spectrum of the oscillators aligned parallel to the b-axis. The orientation of the dielectric axis that corresponds to the single element is fixed parallel to the b-axis for all frequencies.

In contrary, due to the missing orthogonality between the a- and c-axis and the missing alignment of the transition moments parallel to these axes, the other two dielectric axes are restricted to be parallel to the a-c plane, but their orientation relative to the a- and c-axis varies with frequency and is also different for the imaginary and real part. The dielectric tensor function normal to the b-axis has to be calculated by simultaneously fitting the four spectra recorded from the a-c-plane:

$$\varepsilon_{x,z} = \begin{pmatrix} \varepsilon_{\infty,xx} & \varepsilon_{\infty,xz} \\ \varepsilon_{\infty,zx} & \varepsilon_{\infty,zz} \end{pmatrix} + \sum_{t=1}^{N} \frac{S_t^2}{(\tilde{\nu}_t^2 - \tilde{\nu}^2) - i\gamma_t\tilde{\nu}} \begin{pmatrix} \cos^2\varphi_t & \cos\varphi_t \sin\varphi_t \\ \cos\varphi_t \sin\varphi_t & \sin^2\varphi_t \end{pmatrix} \tag{2.33}$$

In the generalized form the dielectric function has the form

$$\varepsilon_{x,y,z}(\tilde{\nu}) = \begin{pmatrix} \varepsilon_{\infty,xx} & 0 & \varepsilon_{\infty,xz} \\ 0 & \varepsilon_{\infty,yy} & 0 \\ \varepsilon_{\infty,xz} & 0 & \varepsilon_{\infty,zz} \end{pmatrix} + \sum_{j=1}^{N} \frac{S_j^2}{(\tilde{\nu}_j^2 - \tilde{\nu}^2) - i\gamma_j\tilde{\nu}} \cdot \mathbf{M}(\Phi_j, \Theta_j).$$

The index j is the sum of t and the number of oscillators aligned normal to the b-axis. The orientation angles in the generalized form are (Φ, Θ)=(0°, 0°) for the oscillators

parallel to the b-axis and $(\Phi, \Theta)=(\varphi, 90°)$ for the oscillators in the a-c plane.
The angles between the crystal axes in the **triclinic** system are all different from 90°. The only possible symmetry is inversion symmetry. Fig. 2.15 shows the unit cell and exemplary distribution of transition moments for a triclinic crystal. As there is no predominant direction, the transition moments are arbitrarily arranged relative to the crystallographic a-, b- and c-axis in the crystal. Consequently, the principal (or dielectric) axes of the real and imaginary part of the dielectric tensor function have in general different orientations, also, the orientation of the axes vary with frequency. Therefore, a preference of certain crystal faces, from which reflection measurement should be taken, over others does not exist. To perform dispersion analysis, a set of 12 spectra recorded from three crystal faces turned out to be the most suitable set of spectra, cf. chapter 2.3. The only condition with regard to the shape of the crystal is that the orientation of the crystal faces to each other must ensure that dispersion analysis can capture the transition moments as good as possible.

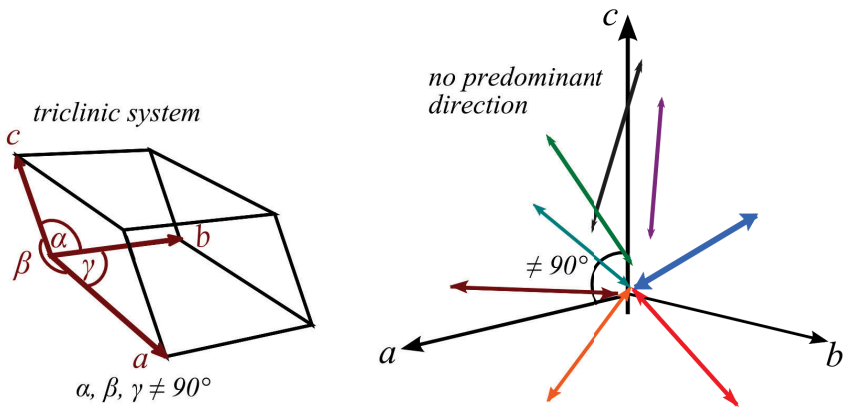

Fig. 2.15. Left: unit cell for a triclinic crystal. Right: distribution of transition moments. In the triclinic system no predominant axis is left and the transition moments are oriented arbitrarily relative to the crystallographic a-, b- and c-axis.

2.5 Miller Indices

To guarantee reproducibility of the measurements and to identify the orientation of the sample or cube cut out of the crystal it is helpful to know the Miller indices of the crystal faces. Miller indices can be determined by x-ray analysis or by creating the stereographic projection of a crystal [25]. All Miller indices given in this work are related to the crystal coordinate system. The indices are defined as the reciprocal intersection points of the crystal face with the coordinate system (which is not necessarily the case [25]). The indices h k l refer to the axes $a\,b\,c$, respectively.
In fig. 2.16 three crystal faces are shown with different orientation in the crystal coordinate system. The procedure is as follows: The intersection points m, n, p of e.g. the

blue plane with the axes $a\,b$ and c are determined: $m\,n\,p$=1 2 3. In the next step of the reciprocal intersection points $\frac{1}{1}\,\frac{1}{2}\,\frac{1}{3}$ the lowest common denominator is determined:

$$\frac{1}{1}\,\frac{1}{2}\,\frac{1}{3} \quad \longrightarrow \quad \frac{6}{6}\,\frac{3}{6}\,\frac{2}{6}$$

Then the values of the numerator are the Miller indices, for the blue plane they are (hkl)=(632). For the green plane in fig. 2.16 the intersection points m n p are 2 2 4. After finding the common denominator of the reciprocal intersection points $\frac{1}{2}\,\frac{1}{2}\,\frac{1}{4} \longrightarrow \frac{2}{4}\,\frac{2}{4}\,\frac{1}{4}$ the Miller indices for the green plane are (hkl)=(221). If a plane is oriented parallel to a coordinate axis, the intersection point with that axis is a point at infinity, the corresponding Miller index is 0. Conventionally, a negative index is indicated with a bar above the number, so the indices of the red plane are (hkl)=($\bar{2}$30). Characterizing the orientation of the crystal planes with Miller indices allows to indicate the plane detached from the absolute intersection points, as the Miller indices give the ratio of the intersection points. The so-called *higher order* planes, which differ by a multiplication factor are equal, e.g. (110) and (220), but the distance between the parallel planes is reduced by that factor. The coordinate system the Miller indices refer to is not restricted to be orthogonal; for monoclinic and triclinic crystals the normals of the crystal planes (100), (010) and (001) are *not* parallel to the crystal axes a, b, c [25]. Labeling faces with Miller indices in curly brackets {hkl} means the faces are indicated by permutations of the h, k, l in curly brackets, e.g. {120}=(120), (210), (012), ($\bar{1}$20) and so on.

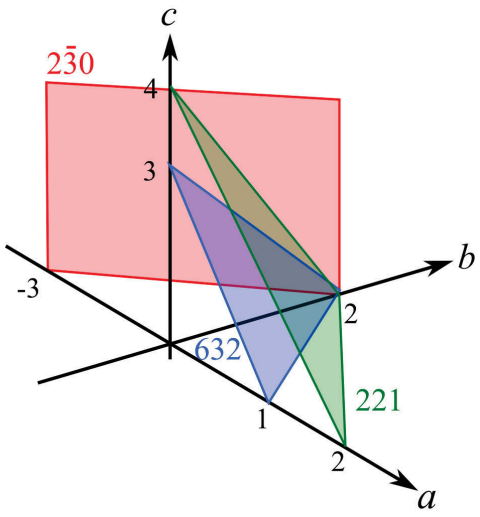

Fig. 2.16. Illustration of Miller indices: a, b, c: crystal coordinate system, the blue, green and red plane represent the crystal faces.

2.6 Stereographic projection

The stereographic projection is a method that reveals the relation of the Miller indices to each other. It also offers the possibility to set the crystal axes in correct relation to the Miller indices of the crystal faces for crystals with no orthogonal coordinate systems. To describe the morphology of a crystal only the angle relations of the faces to each other are relevant. Different crystals of one kind can grow their faces in different sizes and can also grow distorted faces if they grow under stress. Therefore, it is more general to only consider the face *normals* instead of the crystal face itself [25].
To create the stereographic projection the perpendiculars are dropped of each of the crystal face outgoing from a point within the crystal body, as is shown in fig. 2.17, left. That point simultaneously is the center of a sphere, whose surface is penetrated by the face normals. The intersection point of a face normal with the surface of the sphere is called the *pole* of that certain crystal face. Conventionally the sphere is projected to the "equatorial plane" with the "south pole" as center [25], cf. fig. 2.17, right. This is done by letting the pole drop perpendicularly onto the equatorial plane. The result of this procedure is the stereographic projection. The coordinates of the poles are given with the angles φ and θ. By definition the angle φ runs clockwise around the stereographic projection with ϕ=0° at 12 o'clock position, the angle θ runs from the center of the stereographic projection towards the edge of the circle. The poles of the face normals are labeled with Miller indices in round brackets. The poles of the penetration point of a *crystal axis* with the sphere are labeled with Miller indices in square brackets.

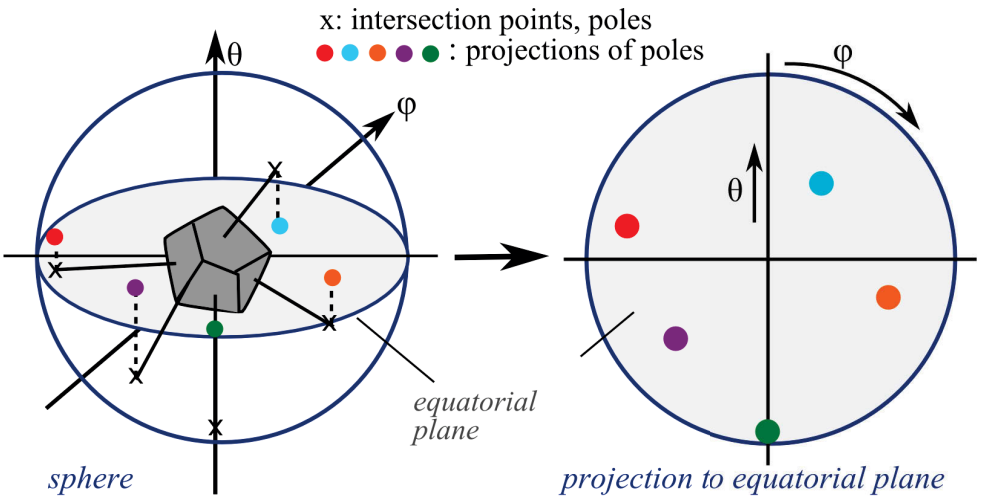

Fig. 2.17. Stereographic projection of a crystal. Left: of each of a crystal face the intersection point of the face normal with the sphere is determined. Right: The poles are projected to the equatorial plane.

2.7 FT-IR-spectrometer

The reflection spectra of the crystals were recorded with a Bruker V80v FT-IR spectrometer. A FT-IR (Fourier Transform InfraRed) spectrometer computes a measured spectrum via Fourier Transformation (as the name already suggests). This implies that the spectrum is recorded as interferogram before it is transformed into a frequency spectrum which plots the reflected intensity at each individual frequency[1]. The spectrometer consists of an IR-source, an interferometer, a sample compartment, and a detector to register the interferogram signal and a computer to transform the interferogram into a frequency spectrum [13, 29]. The schematic setup of the spectrometer is shown in fig. 2.18.
The MIR-source of the Bruker V80v spectrometer is a globar source, which is basically a glowing silicon carbide resistor. A mercury high pressure bulb covers the FIR spectral region. For the triclinic crystals the latter source was used to measure in the FIR region, for all other employed crystals in this work the silicon carbide source was sufficient to cover both the MIR and FIR regions. The interferometer of the Bruker spectrometer is a Michelson spectrometer in which the IR beam is split by a 50% beam splitter into two beams ("BMS" in fig. 2.18). The two beams are reflected by a mirror, of which one of them is a mobile mirror, and are reunited again by the beam splitter so the beams can interfere. The interferogram is created by moving the mobile mirror, therefore the interferogram is a function of the translation distance of the mirror. The resolution $\Delta\nu$ of the spectrometer is given by $1/\Delta\nu = 2d$ [13] with d the traveled

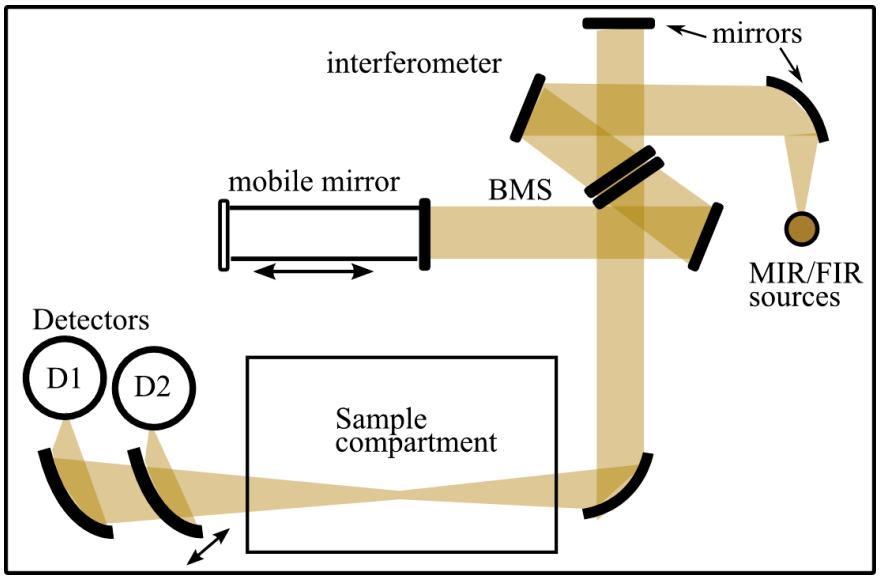

Fig. 2.18. Schematic setup of the Bruker V80v spectrometer. The spectrometer consists of different radiation sources, the interferometer with the beam splitter (BMS), mobile mirror and sample compartment, and different detectors to cover the different ranges of the radiation.

[1]The output spectrum is given in wavenumbers as mentioned in chapter 2.1.

distance of the mirror. For the employed resolution of $2\,\mathrm{cm}^{-1}$ the travel distance is 0.25 cm, for a resolution of $0.01\,\mathrm{cm}^{-1}$ the mirror must be moved as far as 0.5 m.
The number of measured frequency points is determined by the desired highest wavenumber ν_{max} for the spectrum and is given by $\nu_{max}/2$ (Shannon-Nyquist theorem [30]). For the MIR region the Bruker spectrometer employs are a deuterated L-alanin doped triglycine sulfate detector (RT-DLaTGS) and for the FIR region a deuterated triglycine sulfate detector (RT-DTGS) is used.
The intensity of the IR-source varies with frequency, so a background spectrum usually with a gold mirror (R_{mirr}) is recorded. For the employed 8° reflection unit a second background spectrum (R_{ru}) needs to be recorded, as a small quantity of the incident light ($\approx 5\%$) is reflected without a sample. The corrected reflection spectrum ($R_{spec'}$) if the spectrum is measured with the sole polarizer is then calculated by

$$R_{spec',s/p} = \frac{R_{spec,s/p} - R_{ru,s/p}}{R_{mir,s/p} - R_{ru,s/p}}. \tag{2.34}$$

In case of the cross polarization spectra the corrected spectrum is calculated by

$$R_{spec',sp/ps} = \frac{R_{spec,sp/ps} - R_{ru,ss/pp}}{R_{mir,ss/pp} - R_{ru,ss/pp}}. \tag{2.35}$$

The indices in $R_{s/p}$, $R_{sp/ps}$ and $R_{ss/pp}$ are an abbreviation for R_s or R_p, R_{sp} or R_{ps} and R_{ss} or R_{pp}, respectively. For the cross-polarization spectra the reference spectra of the reflection unit and mirror are recorded with the same transmission direction of the polarizer and analyzer as the cross-polarization spectra indicate the ratio of the reflected light whose polarization has been changed by the crystal.

2.8 Fit routine and evaluation scheme

The measured reflection spectra are fitted with a self-written optimization routine in Matlab [31]. All measured spectra have to be fitted simultaneously as every oscillator generally influences every spectrum. The spectra are evaluated according to the following scheme: For the measured spectra starting values are manually created by roughly modeling the spectra giving each oscillator a value for resonance wavenumber, strength and damping constant. The initial orientation angles are set to (Φ, Θ)=(0°, 0°), (0°, 90°) or (90°, 90°). As the orientations are unknown and each start value is as good as the other, each oscillator is given one of the three orientation angle pairs. Oscillators with one of these three orientations appear in two spectra with full intensity (given by the strength) and in four spectra with halved intensity. Tab. 2.1 lists the orientation angles and the according spectra the oscillator with this certain orientation appears with full and halved intensity. As with these initial orientation angles the oscillators

Φ, Θ	appears with full intensity in	appears with halved intensity in
0°, 0°	R_s 0 90 0, R_p 90 90 90	$R_{s/p}$ 0 90 45, $R_{s/p}$ 90 90 45
0°, 90°	R_s 0 0 0, R_s 90 90 90	$R_{s/p}$ 45 0 0, $R_{s/p}$ 90 90 45
90°, 90°	R_p 0 0 0, R_p 0 90 0	$R_{s/p}$ 45 0 0, $R_{s/p}$ 0 90 45

Table 2.1. Orientation angle for the start values and influence on the respective reflectance spectra.

appear with highest intensity in the spectra of the cube edges, it is advisable to model the spectra of the cube edges as best as possible with the manually generated start values. The spectra recorded with incident light parallel to the cube face diagonals are generally reproduced very poorly that way, but as long as a few spectra seem to be roughly modeled by the initial values, the fit routine can handle the spectra.

For the principal elements of the dielectric background values are estimated by roughly taking the square root of the reflectivity in the high wavenumber region behind the last oscillator with the highest wavenumber. The off-diagonal elements are set zero for the beginning. The number of oscillators is mainly chosen by the numbers of visible bands present in the spectral range of interest, supported on the one hand by the information about the total number of expected vibrations (factor group analysis, [32]) and on the other hand by the number of expected vibrations for a certain crystal compound (site group analysis, [32]).

In the second step the error value of the manually modeled spectra is calculated. The error of one spectrum is the difference spectrum between measured and calculated spectrum, summed for all wavenumber points. The difference spectrum is the absolute value of the difference between measured and calculated spectrum. The total error value is then the sum of the errors of all spectra. For complex spectra with many reflection bands sometimes the fit routine achieves better results by adding a power to the errors of the spectra, so the respective difference values get more weighted. With e.g. a power of 2 a difference of 0.1 is now 0.01, a difference of 0.5 is now 0.25. The ratio of 0.5/0.1 is 5, the ratio of 0.25/0.01 is 25, so the higher the power added to the errors of the spectra, the more contribute higher difference values to the error value. With this, for spectra with an only moderate agreement between measurement and calculation, the fit can (not always) find a deeper minimum for the error values.

Then the loop of the fit routine is started. Fig. 2.19 shows the evaluation scheme on the example of one quartz spectrum (in reality the fit routine evaluates all 12 measured spectra simultaneously). By a suitable fit algorithm new oscillator parameters are created and the error value is calculated again. If the total error value from one step to the next step got higher, also the error of at least one difference spectrum got higher, so these new oscillator parameters are skipped. If the error value got lower that means that the error of at least one difference spectra got lower, so the new parameters are taken as initial values for the next loop cycle. In the further process for some loop cycles the principal elements of the dielectric background and the oscillator parame-

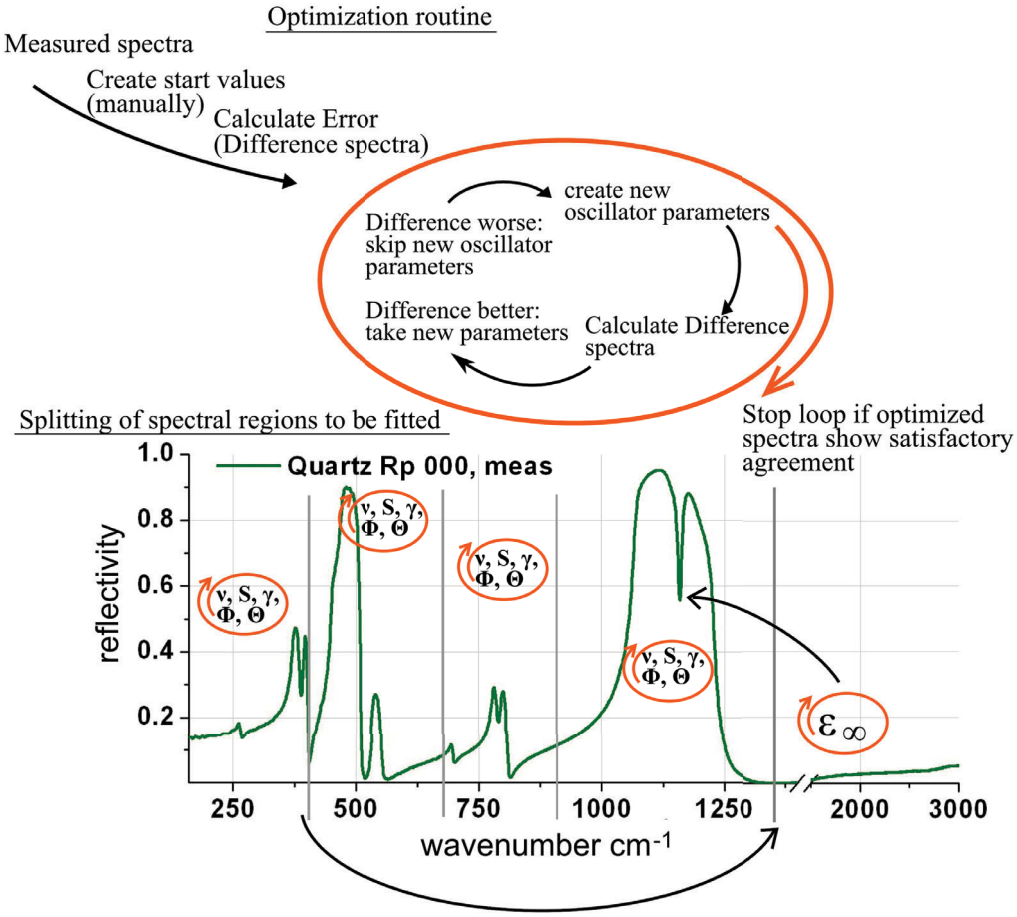

Fig. 2.19. Above: Schematic illustration of the fit routine. The initial values are created manually as explained in the text. Below: Step by step the oscillator parameters of each following spectral section are fitted. The hole sequence should be repeated for a few cycles until the results for the oscillator parameters converge. If no satisfying results are gained for the fitted oscillator parameters, the optimization routine has to be restarted with new initial values.

ters are optimized alternately, as also the principal elements influence the oscillator parameters. With the help of simulated spectra many different sequences to find the best order for the oscillator parameters to be fitted were tried out and compared to the known oscillator parameters of the simulated spectra. The fitted oscillator parameters matched the true parameters of the simulated spectra best by fitting the oscillator strengths first, then the resonance wavenumbers and then the orientation angles and damping constants. Afterward the whole sequence of fitting the oscillator parameters should be repeated several times.

Later on the off-axis elements of the dielectric background are fitted. Experience and comparison with simulated reflection spectra showed that the best results for the off-axis elements are achieved by employing the same wavenumber region that was used to fit the principal elements. The oscillator parameters are fitted beginning with os-

cillators at the high wavenumber region and advancing step by step to the oscillators at the low wavenumber region, as is shown in fig. 2.19. In each spectral region it is advisable to fit at first dominant oscillators with high intensity and then proceed with weaker oscillators, which significantly shortens the fit procedure.
By trying out many different algorithms the two algorithms "fminunc" and "fminseachbnd" remained the ones that produced the best fit results. The algorithm "fminunc" proved to be the best algorithm for the beginning of the fit routine when the starting values resemble the measured spectra still very poorly. "Fminunc" is a quasi-Newton algorithm that was proposed by William C. Davidon [33]. As quasi-Newton method the Hessian matrix (square matrix of the second-order partial derivative of a function) is not computed explicitly as calculating the Hessian matrix numerically involves a large amount of computation [31]. To gain curvature information the observed behavior of the function $f(x)$ in question and its derivative $\nabla f(x)$ is employed to make an approximation to the Hessian matrix using an appropriate updating technique.
The "fminseachbnd" algorithm is based on the Nelder-Mead simplex algorithm [34] and allows to introduce boundaries for a variable. A boundary is a maximum value Δx by which a variable can be altered from one optimization step to the other. The Nelder-Mead method is a direct search method, the algorithm works without computing any derivatives of the function. The algorithm first makes a simplex (a polytope of N+1 basic points in N dimensions) around the start values. Then some test points together with their function values are computed, and around each test point a new simplex is generated. The worst test point, which generates the highest error value is reflected through the center of the simplex. If for this point the error value is lower than for the current point, the algorithms stretches exponentially into this direction, if not, the algorithms shrinks the simplex towards a better point.
During the fitting process it can occur that the optimization gets stuck in a local minimum; the error value is reduced only marginally from one cycle to the other, but the agreement between fitted and measured spectra is still poor. In this case the number of oscillators and their parameters have to be checked. There can be too many or too less oscillators, or some parameters are too far away from a value that makes the fit agreeable. In this case the fitting process starts again by improving the manually generated initial values. The fit of the spectra can be regarded as being successful if the fitted spectra show satisfactory agreement to the measured spectra.
Fig. 2.20 shows an example of a measured (red) and fitted spectrum (black) of the uniaxial lithium niobate. The single bands shown in different colors are all the oscillators, that sum up to the fitted spectrum.
The figure shows that one can not conclude directly from the form of a measured spectrum to the parameters (resonance wavenumber, strength and damping constant) of the transition moments contributing to a spectrum. In this example the oscillator

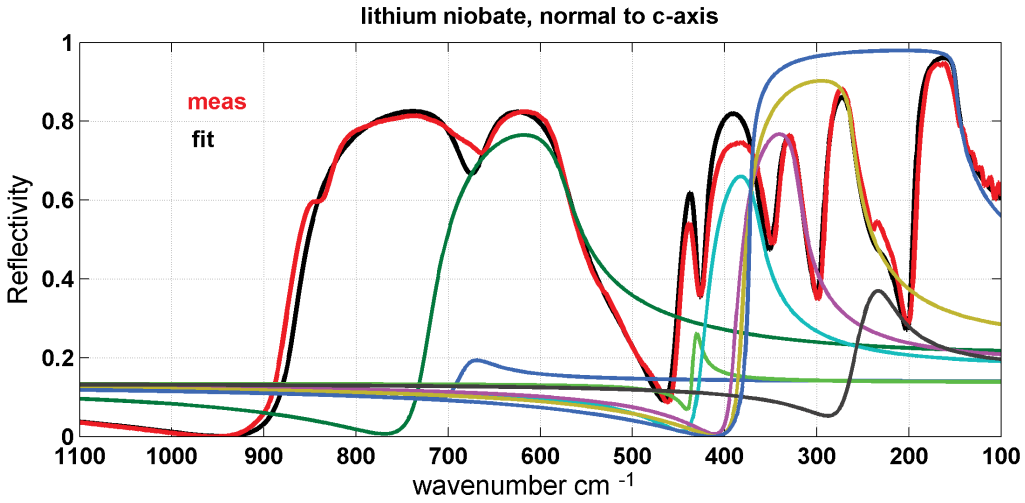

Fig. 2.20. Example of a measured (red) and fitted (black) spectrum of the uniaxial lithium niobate. The single bands in different colors represent the oscillators that sum up to the fitted spectra.

with the highest wavenumber is at $\approx$600 cm^{-1} and not at $\approx$750 cm^{-1}, as it might seem intuitively.

Concerning the reliability of the oscillator parameters investigations with different sets of simulated spectra with varying number of oscillators and spectral distance between the oscillators were made. It turned out that if the spectral distance of the oscillators is roughly not more than the half value of the strength of the more intense oscillator, the strength can be found within $\pm$20 cm^{-1}, damping constants are found within $\pm$20%. Reason for the higher uncertainty of the damping constant is that changes in the damping constant do not influence the shape of the spectrum as distinctive as changes in the strength do. Orientation angles in this configuration can differ up to $\pm$20°. For a very weak oscillator that appears only as shoulder in a very intense oscillator (ratio roughly 1:6) the strength and damping constant fitted for the weak oscillator can only be regarded as a tentative guess. The errors of the calculated angles can get so high that the angles lose any meaning for the oscillator.

Depending on the quality of the spectra the uncertainty of the fitted principal elements of the dielectric background tensor is between $\pm$0.1 and $\pm$0.2 (the dielectric tensor is unitless). For spectra of poor quality like the spectra of triclinic $K_2Cr_2O_7$ the uncertainty of the fitted off-axis elements is in the order of the values for the elements themselves. As the off-axis elements usually are less than 10% of the values for the principal elements and contribute therefore only little to the background tensor, the quality of the fitted spectra is barely affected. For spectra of good quality, like the spectra of the uniaxial crystals, the uncertainty of the fitted off-axis elements can be estimated as roughly 40-50/% of the values for the principal elements.

Chapter 3

Characterization of investigated crystals

By the selection of the employed crystals preference was given to crystals grown in the laboratory to avoid impurity effects that might occur in naturally grown crystals and might disturb the measured IR reflectance spectra.
The triclinic crystals $CuSO_4 \cdot 5\,H_2O$ and $K_2Cr_2O_7$ were grown from an oversaturated solution. The quartz and one calcite crystal were grown by hydrothermal synthesis by Carl Zeiss, Jena. The other calcite and the topaz crystals were naturally grown crystals and a loan from the Mineralogische Sammlung, Jena. The lithium niobate, neodymium gallate and yttrium ortho silicate crystals were grown by Czochralski method by the Institut für Kristallzüchtung, Berlin. The monoclinic spodumene crystal was purchased from a private mineral collection. The spodumene crystal is a naturally grown crystal of excellent quality. If possible, a cube with an edge length of at least 5 mm was cut out of the crystals and polished with 1μm diamond paste from Struers, the water soluble $CuSO_4 \cdot 5\,H_2O$ and $K_2Cr_2O_7$ samples were polished with a special water free, oil-based paste.

3.1 Triclinic crystals

$CuSO_4 \cdot 5\,H_2O$and $K_2Cr_2O_7$ single crystals were grown at room temperature by evaporation of a saturated copper(II)sulfate solution and a saturated potassium(II)dichromate solution, respectively. Of the several small crystals that grow in the beginning three to four crystals with nicely developed faces are selected to grow on in the solution, the other initial crystals are removed. The solution the selected crystals grow in has to be kept free from newly grown crystals. After several weeks, depending on the temperature of the solution, $CuSO_4 \cdot 5\,H_2O$ crystal with a length of the longest edge of 5 cm and $K_2Cr_2O_7$ crystals with a length of 2 cm were obtained.

The Miller indices of the natural growing faces were determined with the help of stereographic projections, supported with x-ray analysis in case of the $CuSO_4{\cdot}5\,H_2O$ crystal. The $K_2Cr_2O_7$ crystal could not be investigated with x-ray analysis due to the high absorption of the material. Both $CuSO_4{\cdot}5\,H_2O$ and $K_2Cr_2O_7$ have C_i^1 symmetry, the i indicates that this crystal class possesses an inversion center.

3.1.1 Copper sulfate pentayhdrate, $CuSO_4{\cdot}5\,H_2O$

Of the $CuSO_4{\cdot}5\,H_2O$ crystal a cube was cut out with an edge length of ≈5 mm under the preservation of the (110) surface. Fig. 3.1, right, shows the $CuSO_4{\cdot}5\,H_2O$ crystal labeled with the Miller indices and the corresponding stereographic projection (left). Due to the triclinic symmetry the poles of the axes do not coincide with the poles of the (100), (010) and (001) face normals. The table in fig. 3.1 gives the angle orientations of the direction of the axes. The unit cell parameters for $CuSO_4{\cdot}5\,H_2O$ are [35]:
a=6.12 Å, b=10.72 Å, c=5.97 Å
α=82.3°, β=107.3°, γ=102.6°
The unit cell contains two $CuSO_4{\cdot}5\,H_2O$ molecules (Z=2) [35].
In the $CuSO_4{\cdot}5\,H_2O$ unit cell there are two different types of water molecules. The first type consists of four water molecules whose oxygen atoms are coordinated to a central copper ion in a nearly square plane configuration. The second type is the fifth water molecule, that is not coordinated to a copper ion but to one oxygen atom from each of two sulfate ions by hydrogen bonding. The bond angle α of the first type of water molecules is with α=114° more distorted than the bond angle of the second

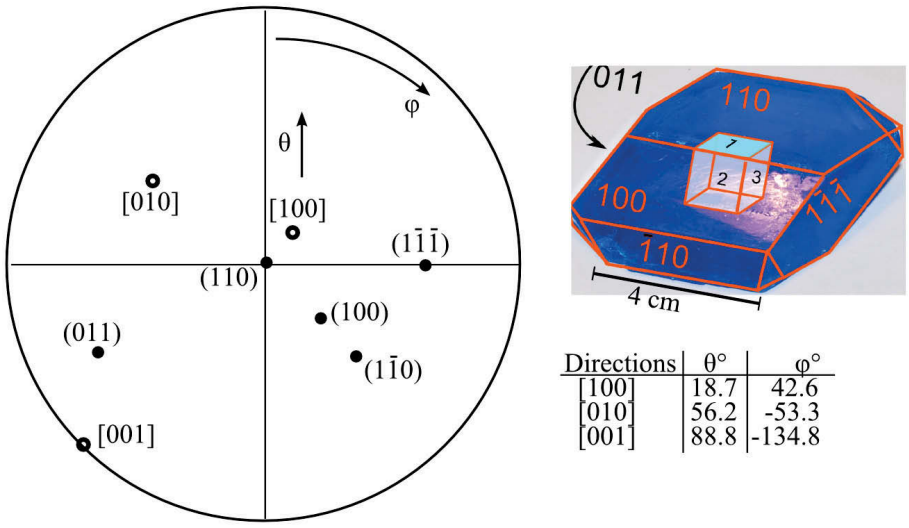

Directions	θ°	φ°
[100]	18.7	42.6
[010]	56.2	-53.3
[001]	88.8	-134.8

Fig. 3.1. Left: Stereographic projection of $CuSO_4{\cdot}5\,H_2O$. Right: Single crystal of $CuSO_4{\cdot}5\,H_2O$ labeled with Miller indices. The poles of the crystal axes a, b, c are listed separately as they do not coincide with the (100), (010) and (001) face normals due to triclinic symmetry (table).

water molecule type with α=105°, which is the bond angles of a free water molecule. The Cu–O–S bonds are oriented perpendicular to the square plane, the compounds of the unit cell build infinite chains of $(H_2O)_4 - Cu - SO_4 - Cu(H_2O)_4$, which are linked by hydrogen bonding to the second type of water molecule as bridge. The SO_4^{2-} ions have lost the tetrahedral symmetry of the free SO_4^{2-} ion. Factor group analysis was performed based on the tabulation of vibrational contributions of atoms on different sites [32], and the obtained distribution of normal modes among the symmetry species and their activities are listed in tab. 3.1 (for the meaning of the vibration symbols see Index of symbols). The site symmetry of the Wyckoff position is given in brackets next to the Wyckoff symbol.

ion	Wyckoff-position	contributed vibrations
Cu(1)	1a (C_i)	$3\,A_u$
Cu(2)	1e (C_i)	$3\,A_u$
1×S, 9×O, 10×H	2i (C_1)	$3\,A_g$+$3\,A_u$
		$\sum 66\,A_u$+$60\,A_g$
Raman active	acoustic	total IR active
$60\,A_g$	$3\,A_u$	$63\,A_u$

Table 3.1. Factor group analysis of $CuSO_4{\cdot}5\,H_2O$.

3.1.2 Potassium dichromate, $K_2Cr_2O_7$

Of the $K_2Cr_2O_7$ crystal no cube could be gained as the crystal cracked into pieces during the attempt to cut the cube. Furthermore, the cut faces did not reach a sufficient surface quality by polishing due to the brittleness of the crystal. Therefore, and because of the presence of three mutual almost orthogonal naturally grown faces the as-grown single crystal was employed instead of a cube. The stereographic projection and the single crystal of $K_2Cr_2O_7$ labeled with Miller indices are shown in fig. 3.2. The top right photograph shows the grown $K_2Cr_2O_7$ crystals. The unit cell parameters of $K_2Cr_2O_7$ are [36]
a=13.37 Å, b=7.37 Å, c=7.44 Å
α=90.75°, β=96.21°, γ=97.96°, Z=4
With Z=4 there are four dichromate ($Cr_2O_7^{2-}$) ions per unit cell, but due to inversion symmetry there are only two crystallographic distinct types of dichromate ions. The skeletal structure is built by the dichromate ions which consist of two tetrahedral CrO_4 groups that are only slightly distorted. Both CrO_4 groups share one oxygen ion. The dichromate ions differ by 5° and 10° from the eclipsed configuration. The angle of eclipse is the angle by which one of the the CrO_4 tetrahedra must be turned to bring the $Cr_2O_7^{2-}$ group into the eclipsed configuration [37]. The Cr-O-Cr bridge angle for the one dicromate ion is 124°, the bridge angle for the second dichromate type is 128° [37]. Additionally, the Cr-O bond angle of the distorted tetrahedron varies from the tetrahedra angle of 109.5°, which reduces the C_{2v} symmetry of a free

dichromate ion to C_1. In $K_2Cr_2O_7$ all atoms occupy the same Wyckoff position, which gives rise to an equal number of even and odd modes. The corresponding factor group analysis is given in tab. 3.2. The 4 Cr ions and 14 O ions of 2× $Cr_2O_7^{2-}$ give rise to $18\times(3\,A_g + 3\,A_u) = 54\,A_g + 54\,A_u$ modes. Subtracting the 2×6 rotational and translational degrees of freedom for each of the A_g and A_u vibrations [32] leaves 42 A_u+42 A_g internal modes for the two crystallographically distinct $Cr_2O_7^{2-}$ molecules. A single potassium ion contributes 3 A_g+3 A_u vibrations, but after subtracting the 3 translational degrees of freedom (a single atom has no rotational degrees of freedom) for each of the A_g and A_u vibrations no internal vibrations are left.

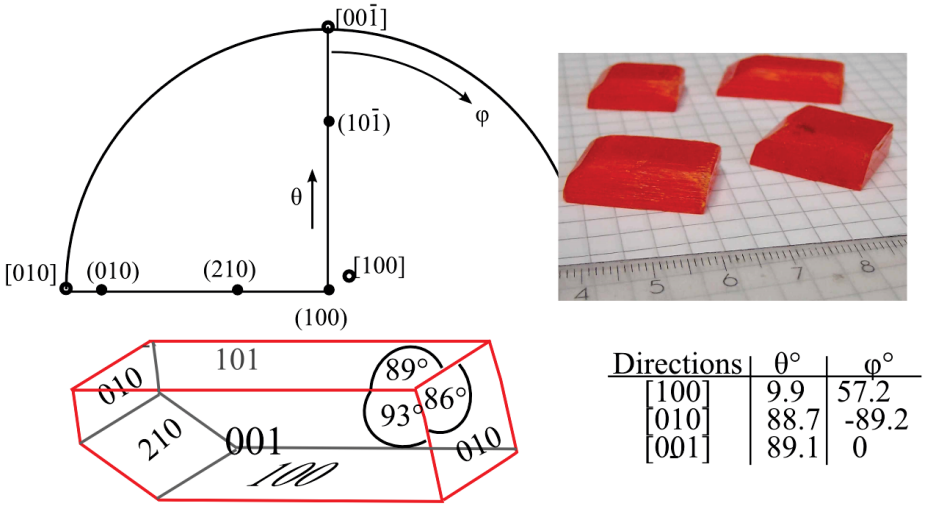

Directions	θ°	φ°
[100]	9.9	57.2
[010]	88.7	-89.2
[00$\bar{1}$]	89.1	0

Fig. 3.2. Top left: Half sphere of the stereographic projection of $K_2Cr_2O_7$ (there are no relevant poles in the lower half sphere). Bottom left: schematic picture of a grown $K_2Cr_2O_7$ crystal labeled with Miller indices. Top right: Photograph of the grown $K_2Cr_2O_7$ crystals. Bottom right table: angle orientation of the poles of the crystal axes.

ion	Wyckoff-position	contributed vibrations
4×Cr, 4×K, 14×O	2i (C_i)	3 A_g+3 A_u $\sum$66 A_u+66 A_g
Raman active	acoustic	total IR active
66 A_g	3 A_u	63 A_u

Table 3.2. Factor group analysis of $K_2Cr_2O_7$.

3.2 Uniaxial crystals

3.2.1 Quartz, SiO_2

The quartz crystal employed for dispersion analysis is the low-temperature modification and has trigonal symmetry with space group D_3^6 or $P3_221$, No. 154 in the International Tables of Crystallography [26]. The lattice parameters are given by a=b=4.91 Å, c=5.40 Å and γ=120°with three molecular entities per unit cell (Z=3) [38].
The trigonal c-axis is a screw axis, a rotation of 120°around the c-axis followed by a translation of c/3 along the c-axis transfers every atom to an equivalent position. The unit cell of quartz contains three SiO_2^{2-} tetrahedra, that are connected to infinite chains oriented along the c-axis. Bragg [39] showed that this spiral can be twisted clockwise or anticlockwise around the c-axis, but the sense of rotation has no effect on the total number and kind of vibrations [32]. Huggins [40] also found that the SiO_2^{2-} tetrahedra are only slightly distorted, as the deviation of the Si–O bond angles from the tetrahedron angle of 109.5°is less than one degree, and the bond lengths of Si–O and O–O in the tetrahedra are also almost identical [41].
Fig. 3.3 shows a stereographic projection of the cube cut out of the crystal and the resulting orientation of the optical axis. For the characterization of the quartz cube the four axis system with four Miller indices is applied as is the common convention for trigonal crystal systems [25]. In the four axis system each of the three a-axes are equal, so the numeration of the axes can be chosen freely. The stereographic projection only shows the orientation of the cube as the original crystal was of quite bulky shape.

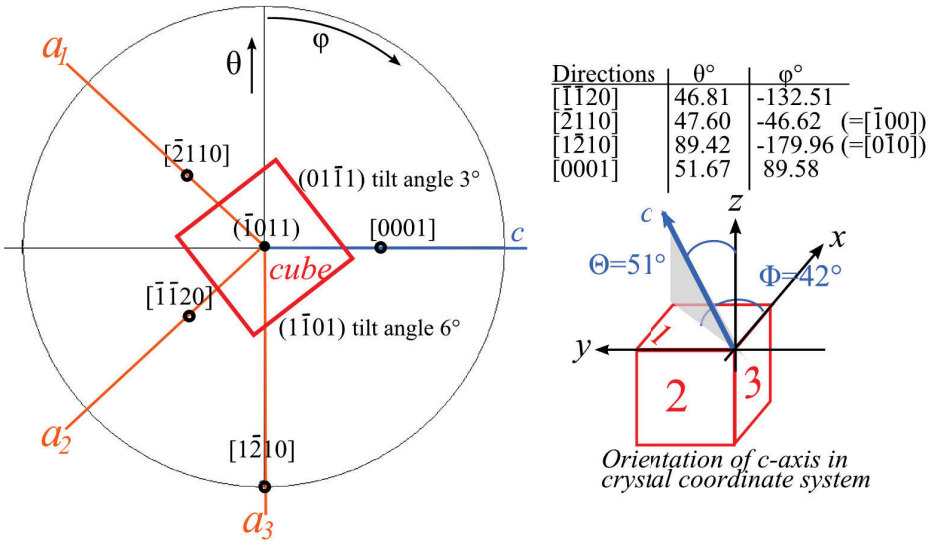

Fig. 3.3. Left: stereographic projection of quartz. The face in direction of view is the ($\bar{1}$011) face, the one side face of the cube is tilted by 3° to the (01$\bar{1}$1) face, the other side face is tilted by 6° to the (1$\bar{1}$01) face. Table: Coordinates of the poles of the axes. Below table: Initial orientation of the cube and c-axis relative to the internal coordinate system.

The cube is cut under preservation of the $(\bar{1}011)$ face of the original crystal with the direction of the c-axis (pole of [0001]) and the direction of the a_3 axis (pole of $[1\bar{2}10]$) almost crossing two corners of the cube. The other two faces are the $(01\bar{1}1)$ face with circa 3° miscut angle, meaning the $(01\bar{1}1)$ face is not the "real" face, but tilted by 3° to the surface. The miscut angle of the $(1\bar{1}01)$ face is 6°. Tab. 3.3 gives the factor group analysis for quartz according to [32]. For the silicon ion the Wyckoff position 3a or 3b depends on the rotation sense of the tetrahedra chain around the c-axis.

ion	Wyckoff-position	contributed vibrations
O	6c (C_1)	$3\,A_1+3\,A_2+6\,E$
Si	3a/3b (C_1)	$A_1+2\,A_2+3\,E$
		$\sum 4\,A_1+5A_2+9\,E$
Raman active	acoustic	total IR active
$4\,A_1$	A_2+E	$4\,A_2+8\,E$

Table 3.3. Factor group analysis for quartz

3.2.2 Calcite, $CaCO_3$

Calcite is of trigonal symmetry with space group $R\bar{3}c$ or D^6_{3d}, No. 167 in the International Tables of Crystallography [26]. The lattice parameters are a=b=4.99 Å, c=17.00 Å and γ=120° with six molecular entities per unit cell (Z=6) [42]. The structure of calcite is mostly illustrated by an infinite chain of Ca^{2+} – CO_3^{2-} – Ca^{2+} – CO_3^{2-} ions, with the CO_3^{2-} ions tilted by 60°to each other [43].

Factor group analysis of calcite according to [32] is given in tab. 3.4. The A_{1u} and A_{2g} modes are silent. One A_{2u} and two E_u modes of the IR active vibrations constitute the internal modes of the CO_3^{2-} ion.

The arbitrarily cut cube was cut out of a $\{10\bar{1}4\}$ rhombohedron. Fig. 3.4 presents the stereographic projection of the calcite rhombohedron with the cube cut out of it. The cube is cut under preservation of the $(10\bar{1}4)$ face of the original rhombohedron with one cube face parallel to the $(0\bar{1}14)$ face and the projection of the c-axis oriented along the face diagonal of the top view. The table in fig. 3.4 lists the coordinates of the directions and face normals, the figure below the table shows the absolute orientation of the optical axis in the crystal coordinate system.

ion	Wyckoff-position	contributed vibrations
1×Ca	6b (S_6)	$3\,A_{1u}+A_{2u}+2\,E_u$
1×C	6a (D_3)	$A_{2g}+A_{2u}+E_g+E_u$
1×O	18e (C_2)	$A_{1g}+A_{1u}+2\,A_{2g}+2\,A_{2u}+E_g+E_u$
		$\sum A_{1g}+4\,A_{1u}+4\,A_{2u}+3\,A_{2g}+6\,E_u+4\,E_g$
Raman active	acoustic	total IR active
$A_{1g}+4\,E_g$	$A_{2u}+E_u$	$3\,A_{2u}+5\,E_u$

Table 3.4. Factor group analysis for calcite.

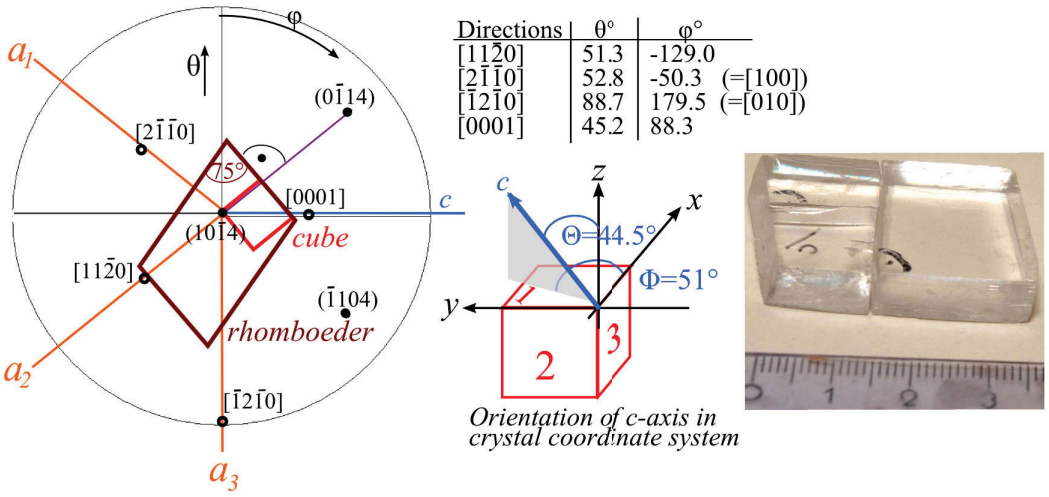

Fig. 3.4. Left: stereographic projection of the calcite $\{10\bar{1}4\}$ rhombohedron and the cube cut out of it. Table: Coordinates of the poles of the crystal axes. Below table: Initial orientation of the cube and orientation c-axis in the crystal coordinate system. Right: employed calcite rhombohedron.

3.2.3 Lithium niobate, $LiNbO_3$

Lithium niobate also is of trigonal symmetry with space group R3c or C_{3v}^6, No. 161 in the International Tables. The lattice parameters are a=b=5.15 Å, c=13.86 Å and γ=120° with Z=6 [44].

Investigations of the structure and physical properties have been carried out particularly by Megaw [44] and Abrahams [45], dielectric properties and optical phonons have been determined by Barker and Loudon [46]. At room temperature the oxygen ions form planar sheets of approximately hexagonal packaging. One third of the interstitial holes is occupied by Li^+ ions, one third by Nd^{5+} ions and the remaining holes have no ion in its center and are empty. Parallel to the c-axis a Li^+ occupied octahedron, an oxygen octahedron with a Nb^{5+} in its center and an empty octahedron are stacked on top of each other, then the sequence repeats.

The hexagonal packaging of the oxygen ions is slightly distorted due to the pronounced difference radii of the Li^+ and Nb^{5+} ions. Furthermore, the Li–O bonds are much weaker than the Nb–O bonds, so the crystal structure is mainly established by the Nb–O framework. Factor group analysis for lithium niobate based on the tables in [32] is given in tab. 3.5. The A_2 modes are silent in Raman- and IR-spectroscopy.

In fig. 3.5 the orientation of the cube cut out of the crystal bar is illustrated. The right photograph in fig. 3.5 shows the employed lithium niobate cube. The c-axis is tilted by 38° to the face normal of the $(10\bar{1}4)$ face. The other two faces are a $(10\bar{1}\bar{2})$ face with 5° miscut angle and a $(1\bar{2}10)$ face.

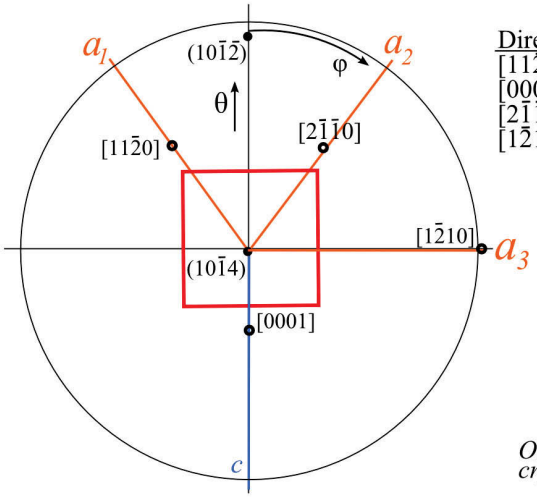

Directions	θ°	φ°
[11$\bar{2}$0]	58.3	-36.9
[0001]	38.1	-179.0
[2$\bar{1}\bar{1}$0]	57.2	35.5 (=[100])
[1$\bar{2}$10]	89.0	90.0 (=[0$\bar{1}$0])

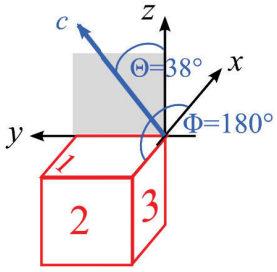

Orientation of c-axis in crystal coordinate system

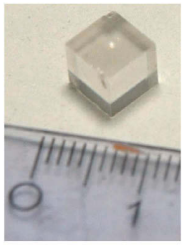

Fig. 3.5. Left: stereographic projection of the lithium niobate cube. The bar grown by Czochralski method is not shown as it is of cylindrical shape without natural growing faces. The face in viewing direction is a (10$\bar{1}$4) face. The optical axis is tilted by 38° to that face. Table: Poles of the crystal axes. Below table: initial orientation of the cube and c-axis relative to the internal coordinate system. Right: Photograph of the employed lithium niobate cube.

ion	Wyckoff-position	contributed vibrations
1×Li and 1×Nb	8a (C_3)	$3\,A_1+A_2+2\,E$
1×O	18b (C_1)	$3\,A_1+3\,A_2+6\,E$
		$\sum 5\,A_1+5\,A_2+10\,E$
Raman active	acoustic	total IR active
$5\,A_1+10\,E$	A_1+E	$4\,A_1+9\,E$

Table 3.5. Factor group analysis for lithium niobate.

3.3 Orthorhombic crystals

3.3.1 Neodymium gallate, $NdGaO_3$

Neodymium gallate has space group Pbnm or D_{2h}^{16} with four $NdGaO_3$ molecular entities per unit cell [47]. The unit cell parameters are a=5.43 Å, b=5.50 Å and c=7.71 Å with α, β, γ=90° [47].

$NdGaO_3$ belongs to the perovskite family with the structure form ABX_3, but due to the different radii of the Nd^{5+} and Ga^{+} ions the symmetry of the cubic perovskite cell is reduced to orthorhombic symmetry [25]. The structure of $NdGaO_3$ is built of GaO_6 octahedra that are tilted to each other. The Nd^{5+} ions sit in the holes between the octahedra. The deviation angle of the inter atomic angles within the GaO_6 octahedra from 90° or 180° is with ±1° very small [48].

Factor group analysis of $NdGaO_3$ is given in tab. 3.6. The left part of fig. 3.6 shows the

$NdGaO_3$ cube cut out of the bar labeled with Miller indices. The cube was cut in a way that the crystal c-axis is aligned parallel to the cube face diagonal of face 1. The axes a and b point upwards towards the other corners of face 1 with an angle of 45°.

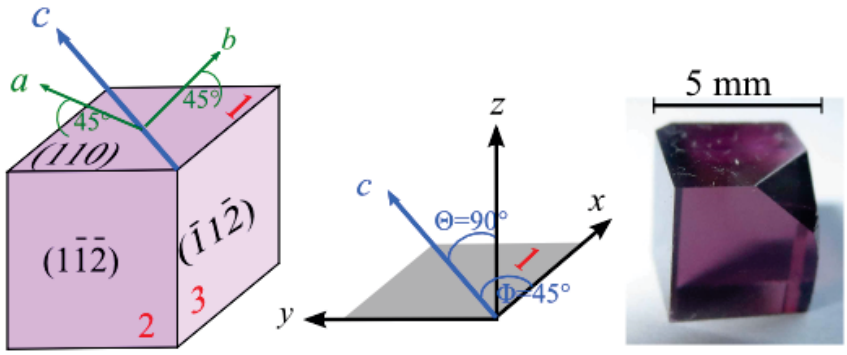

Fig. 3.6. Left: cube cut out of the $NdGaO_3$ bar indicated with Miller indices. The cube was cut with the c-axis parallel to the cube face diagonal of face 1. Middle: orientation of c-axis relative to internal coordinate system (x, y, z). Right: Photograph of the employed $NdGaO_3$ cube.

ion	Wyckoff-position	contributed vibrations
1×Nd, 1×O	4c (C_s)	$2\,A_g+A_u+B_{1g}+2\,B_{1u}+2\,B_{2g}+B_{2u}+B_{3g}$
1×Ga	4b (C_i)	$3\,A_u+3\,B_{1u}+3\,B_{2u}+3\,B_{3u}$
2×O	8d (C_1)	$3\,A_g+3\,A_u+3\,B_{1g}+3\,B_{1u}+3\,B_{2g}+3\,B_{2u}+3\,B_{3g}+3\,B_{3u}$
		$\sum 7A_g+8A_u+7B_{1g}+8B_{1u}+5B_{2g}+10B_{2u}+5B_{3g}+10B_{3u}$
Raman active	acoustic	total IR active
$7\,A_g+7\,B_{1g}+5\,B_{2g}+5\,B_{3g}$	$B_{1u}+B_{2u}+B_{3u}$	$9\,B_{1u}(\|\|c)+7\,B_{2u}(\|\|b)+9\,B_{3u}(\|\|a)$

Table 3.6. Factor group analysis for neodymium gallate.

3.3.2 Topaz, Al_2SiO_4(F, OH)

Topaz has the same space group D_{2h}^{16} as $NdGaO_3$with the unit cell parameters a=4.46 Å, b=8.87 Å and c=8.37 Å with four formula units per unit cell [49]. The left part of fig. 3.7 shows the orientation of the topaz crystal. The right part of the figure shows a photopraph of the real crystal. The structure is built by chains of AlO_4F_2 octahedra and SiO_4 tetrahedra, that are aligned parallel to the crystallographic c-axis [50]. In the ALO_4F_2 octahedron one fluorine ion is located on the top or bottom corner of the octahedron, the other fluorine ion is located in a corner of the equatorial plane. The bond angles between the fluorine and oxygen ions to the aluminum ion are distorted up to 10° from 90°, also vary the inter atomic distances in the octahedra by 0.4 Å [50]. The SiO_4 groups are quite stable, the deviations between the bond length is negligible and the bond angles differ only by 2° from the tetrahedra angle of 109.5° [50]. The AlO_4F_2 octahedra occur in pairs, meaning that each octahedron shares two edges with an adjoining octahedron. No SiO_4 tetrahedron shares edges with another SiO_4 tetrahedron, they are all linked to AlO_4F_2 octahedra.

Factor group analysis of topaz is listed in tab. 3.7. The fluorine and hydroxide ions in the molecular formula of topaz are exchangeable. As the hydroxide content of the employed topaz sample is unknown, the crystal is treated in tab. 3.7 to be free of hydroxide, which has no effect of the expected number of vibrations. As it was not allowed to cut the topaz crystal, the prismatic shape with an angle of 95° instead of 90° must be taken into account for in the Euler matrix that describes the rotation of the sample within the spectrometer (cf. chapter 2.3).

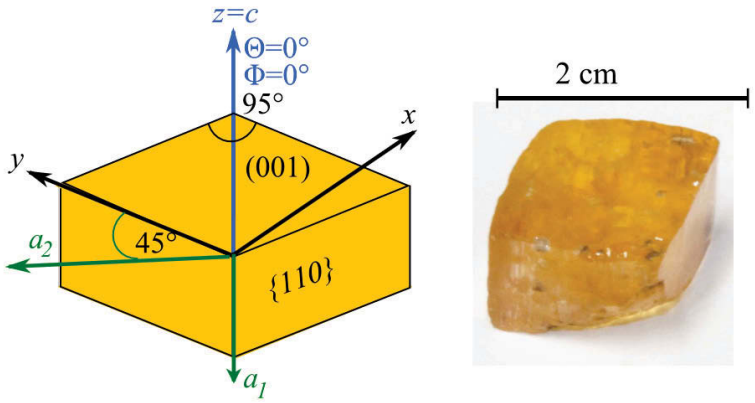

Fig. 3.7. Naturally grown yellow topaz crystal. The side faces are {110} faces, the top face is the (001) face. As for this crystal there is no information which of the crystal axes normal to the c-axis is the a- and b-axis, the axes are indicated with a_1 and a_2.

ion	Wyckoff-pos.	contributed vibrations
1×Si, 1×O, 1×O 1×Al, 1×F, 1×O	4c (C_s) 8a (C_i)	$2\,A_g+A_u+2\,B_{1g}+B_{1u}+2\,B_{2g}+2\,B_{2u}+B_{3g}+2\,B_{3u}$ $3\,A_g+3\,A_u+3\,B_{1g}+3\,B_{1u}+3\,B_{2g}+3\,B_{2u}+3\,B_{3g}+3\,B_{3u}$ $\sum 15A_g+12A_u+15B_{1g}+12B_{1u}+15B_{2g}+15B_{2u}+12B_{3g}+15B_{3u}$
Raman active	acoustic	total IR active
$15A_g+15B_{1g}+15B_{2g}+12B_{3g}$	$B_{1u}+B_{2u}+B_{3u}$	$11\,B_{1u}(\|\|c)+14\,B_{2u}(\|\|b)+14\,B_{3u}(\|\|a)$

Table 3.7. Factor group analysis for topaz.

3.4 Monoclinic crystals

3.4.1 Yttrium ortho silicate, Y_2SiO_5

Y_2SiO_5 has space group 2/m or C_{2h}^6 [51], No. 15 in the International Tables of Crystallography [26]. The unit cell parameters are a=10.41 Å, b=6.72 Å, c=12.49 Å and β=102.65° with Z=8 [51]. The symbol "2/m" indicates that beneath the twofold rotation axis (indicated by "2") which is characteristic for all monoclinic crystals, there is an additional mirror plane normal to the rotation axis (indicated by "/m").
The principle structure of Y_2SiO_5 consists of SiO_4 tetrahedra and a fifth, not silicon-bonded oxygen ion [52]. The fifth oxygen ion is surrounded by four Y^{3+} ions in slightly

distorted tetrahedral coordination, so the structure can be expressed as an arrangement of SiO_4 and OY_4 tetrahedra. The OY_4 tetrahedra form chains that are aligned parallel to the a-axis and are connected to the isolated SiO_4 tetrahedra. The Y^{3+} ions occupy two different positions, one type of Y^{3+} ions is coordinated by nine oxygen ions, the second type of Y^{3+} ions is coordinated by seven oxygen ions [53]. All atoms in Y_2SiO_5 occupy general positions (xyz), factor group analysis based on [32] is given in tab. 3.8.

Of the yttrium silicate crystal only a principally cut sample was available (fig. 3.8). The b-axis was aligned parallel to the internal z-axis, the face normal to the b-axis is the (010)=[010] face. The other cube faces were a $(10\bar{4})$ and (100) face.

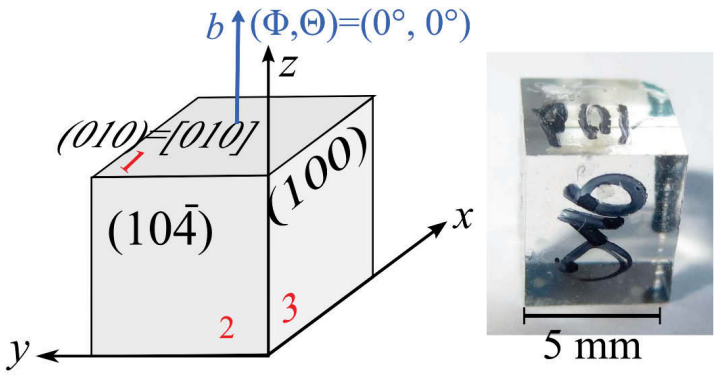

Fig. 3.8. Left: Orientation and Miller indices of the yttrium silicate cube in principal cut. Right: Photograph of the real yttrium silicate cube.

ion	Wyckoff-position	contributed vibrations
2×Y, 1×Si, 5×O	8f (C_1)	$3\,A_g$+$3\,A_u$+$3\,B_g$+$3\,B_u$ $\sum 4\,A_g$+$24\,A_u$+$24\,B_g$+$24\,B_u$
Raman active	acoustic	total IR active
$24\,A_g$+$24\,B_g$	A_u+$2\,B_u$	$23\,A_u$(||b)+$22\,B_u$($\perp$b)

Table 3.8. Factor group analysis for yttrium silicate.

3.4.2 Spodumene, $LiAl(SiO_3)_2$

Spodumene belongs to the pyroxene group and has the same space group as Y_2SiO_5, 2/m or C^6_{2h} with unit cell parameters a=9.45 Å, b=8.39 Å, c=5.21 Å and β=110° with four formulas per unit cell [54].

The crystal is built of infinite SiO_4 tetrahedra chains, in each chain one face of the tetrahedra points into the same direction [55], for adjacent chains that special face points into opposite directions. The SiO_4 tetrahedra chains are not connected directly to each other but by interstitial AlO_6 octahedra. The sites between adjacent SiO_4 tetrahedra are occupied by Li ions [55]. The bond lengths of the O-O and Si-O bonds of the tetrahedra are almost identical, derivations from the mean bond lengths are

negligible [56]. Although the bond lengths O-O and Al-O of the AlO_6 octahedra vary barely, the inter atomic angles in the octahedra differ up to more than 20° from the ideal angles 180° and 90° [56]. Also of the spodumene crystal no arbitrarily cut sample was available, the orientation of the principally cut sample is shown in fig. 3.9. The (110) and ($\bar{1}$00) face are naturally grown faces of the crystal. The Wyckoff positions and contributed vibrations of the ions of $LiAl(SiO_3)_2$ are given in tab. 3.9.

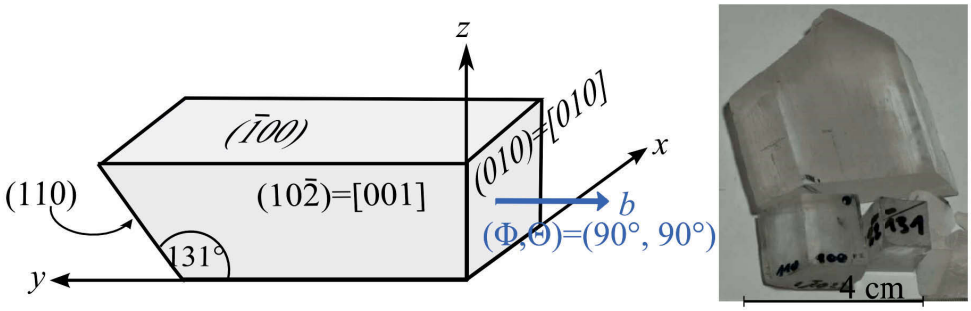

Fig. 3.9. Left: Orientation and Miller indices of a principally cut spodumene sample. Right: Photograph of the purchased spodumene crystal with the samples cut out of it.

ion	Wyckoff-position	contributed vibrations
1×Li, 1×Al	4e (C_2)	A_g+A_u+2 B_g+2 B_u
1×Si, 3×O	8f (C_1)	3 A_g+3 A_u+3 B_g+3 B_u
		$\sum$14 A_g+14 A_u+16 B_g+16 B_u
Raman active	acoustic	total IR active
14 A_g+16 B_g	A_u+2 B_u	13 A_u(||b)+14 B_u($\perp$b)

Table 3.9. Factor group analysis for spodumene.

Chapter 4

Dispersion Analysis of triclinic crystals

4.1 Results of dispersion analysis for $CuSO_4 \cdot 5\,H_2O$

The presentation of the results for the different crystals starts with the triclinic crystals, since the optimization routine for triclinic crystals is the basis for the optimization routine for the other crystals.
The oscillator parameters calculated by dispersion analysis as well as the dielectric background tensor for $CuSO_4 \cdot 5\,H_2O$ are presented in tab. 4.1. Of the 63 vibrations predicted by factor group analysis 50 were found by dispersion analysis. The other oscillators are either located out of the investigated spectral region below $100\,cm^{-1}$ or are shadowed by other oscillators and can therefore not be identified by the fit routine. The 5 water molecules of the unit cell (although Z=2, due to inversion symmetry only five instead of ten water molecules need to be considered) give rise to five deformation vibrations (δ) and 10 symmetric (ν_s) and asymmetric (ν_{as}) vibrations. The fit routine found 4 oscillators (38-41 of tab. 4.1) that describe the δvibration of the water molecules, and 9 oscillators (42-50) that represent the ν_s and ν_{as} vibrations of the water molecules. Usually, the ν_{as} vibrations are located on the higher wavenumber region [11].
The one relevant sulfate ion gives rise to three vibrations originating from the threefold degenerate asymmetric stretching vibration (ν_4) of the free ion. All three are found in oscillators 35-37. The three oscillators have similar values for resonance wavenumber, strength and damping constant and are nearly mutually orthogonal. The angle between oscillators 35 and 36 is 97°, between oscillators 36 and 37 is 86°, and between oscillators 35-37 is 91°. Oscillator 34 represents the symmetric stretching or breathing vibration (ν_1) of the sulfate ion. For a free sulfate ion this vibration is only Raman active, but due to the distortion of the tetrahedron the vibration also becomes IR active,

	$\tilde{\nu}_j$	S_j	γ_j	Φ_j	Θ_j		$\tilde{\nu}_j$	S_j	γ_j	Φ_j	Θ_j
2	117.2	141.7	13.6	129.9	163.0	27	622.2	182.7	17.3	177.5	159.6
3	123.6	79.2	11.9	1.3	118.1	28	647.7	196.3	41.3	5.7	1.1
4	134.8	173.2	19.5	87.9	85.6	29	674.2	254.6	86.5	87.4	116.5
5	141.7	91.0	17.1	17.6	102.2	30	697.1	323.1	112.9	173.5	41.1
6	156.9	84.5	16.3	165.0	102.7	31	774.7	180.0	56.7	24.5	56.0
7	179.2	105.0	14.0	178.2	11.6	32	850.4	243.6	61.3	32.2	112.0
8	186.0	127.5	15.6	7.1	95.1	33	875.6	320.0	96.0	63.5	52.7
9	213.9	82.6	15.5	74.9	72.8	34	980.6	77.4	9.7	90.6	97.5
10	220.5	103.9	19.7	168.6	20.3	35	1062.2	500.4	32.1	104.2	85.1
11	243.3	94.1	16.5	68.8	72.7	36	1095.9	456.5	27.4	8.0	103.3
12	247.8	80.3	17.0	17.0	83.2	37	1099.9	456.1	18.3	170.6	171.3
13	251.0	158.3	31.4	170.8	26.3	38	1648.5	171.3	74.0	71.9	91.3
14	280.4	133.7	18.3	105.5	101.5	39	1651.8	96.8	59.6	172.7	7.7
15	416.3	221.0	49.7	31.5	23.6	40	1665.7	125.8	32.4	1.0	118.9
16	441.6	214.2	36.8	166.6	97.7	41	1681.7	63.5	19.3	145.1	43.0
17	467.6	218.6	55.8	82.1	57.3	42	3102.5	754.6	201.3	95.2	72.3
18	485.1	127.7	33.4	0.8	44.6	43	3112.3	637.8	194.6	89.0	142.1
19	541.0	162.4	61.6	175.4	178.6	44	3158.2	757.8	184.3	17.4	109.2
20	551.1	402.0	111.0	14.0	80.1	45	3185.0	261.6	71.9	63.0	161.0
21	555.6	191.0	63.6	87.9	83.4	46	3210.5	569.3	126.0	80.9	50.7
22	581.0	208.7	36.7	173.2	71.6	47	3305.3	641.6	194.5	0.4	179.3
23	600.8	151.2	25.6	10.7	107.4	48	3330.9	486.5	176.8	179.0	94.9
24	605.8	143.2	18.0	52.9	90.8	49	3345.2	491.6	148.1	86.8	93.9
25	617.8	117.0	18.0	92.3	82.0	50	3475.8	236.8	43.7	161.0	84.3

$$\varepsilon_\infty = \begin{pmatrix} 2.25 & -0.01 & 0.01 \\ -0.01 & 2.15 & 0 \\ 0.01 & 0 & 2.22 \end{pmatrix}$$

Table 4.1. Calculated oscillator parameters resonance wavenumber $\tilde{\nu}_j$, strength S_j and damping constant γ_j, given in wavenumbers and orientation angles Φ_j and Θ_j given in degree. The components of the dielectric background tensor ε_∞ do not have units.

although with very low intensity. The remaining oscillators are overlapping modes of librational, translational and internal modes of the sulfate and water molecules and the $Cu(H_2O)$ complex, of which the librational modes occur in the low wavenumber region of the spectra [57]. All in all, the resonance wavenumbers calculated by dispersion analysis agree with the wavenumbers given by Berger in [57], except for oscillators 31, 36 and 39. Oscillators 19-34 have no counterpart in [57] as Berger did not give values in this spectral region at all.

The 12 measured reflection spectra from the cube-shaped $CuSO_4{\cdot}\,5H_2O$ single crystal together with the fitted spectra are depicted in fig 4.1. The left side of fig 4.1 shows the spectra recorded with polarization direction of the incoming light parallel to the cube edges, on the right side the spectra recorded with polarization direction of the incident light parallel to the cube face diagonal are presented. The cubes in the figure resemble the cube shaped sample of $CuSO_4{\cdot}5\,H_2O$, the numbers 1, 2 and 3 label the measured cube faces. The blue and red double arrows of the cube in the left part of the figure illustrate the polarization state of the incoming light that produced the spectra of the cube edges, which are assigned by the according blue and red arrow.

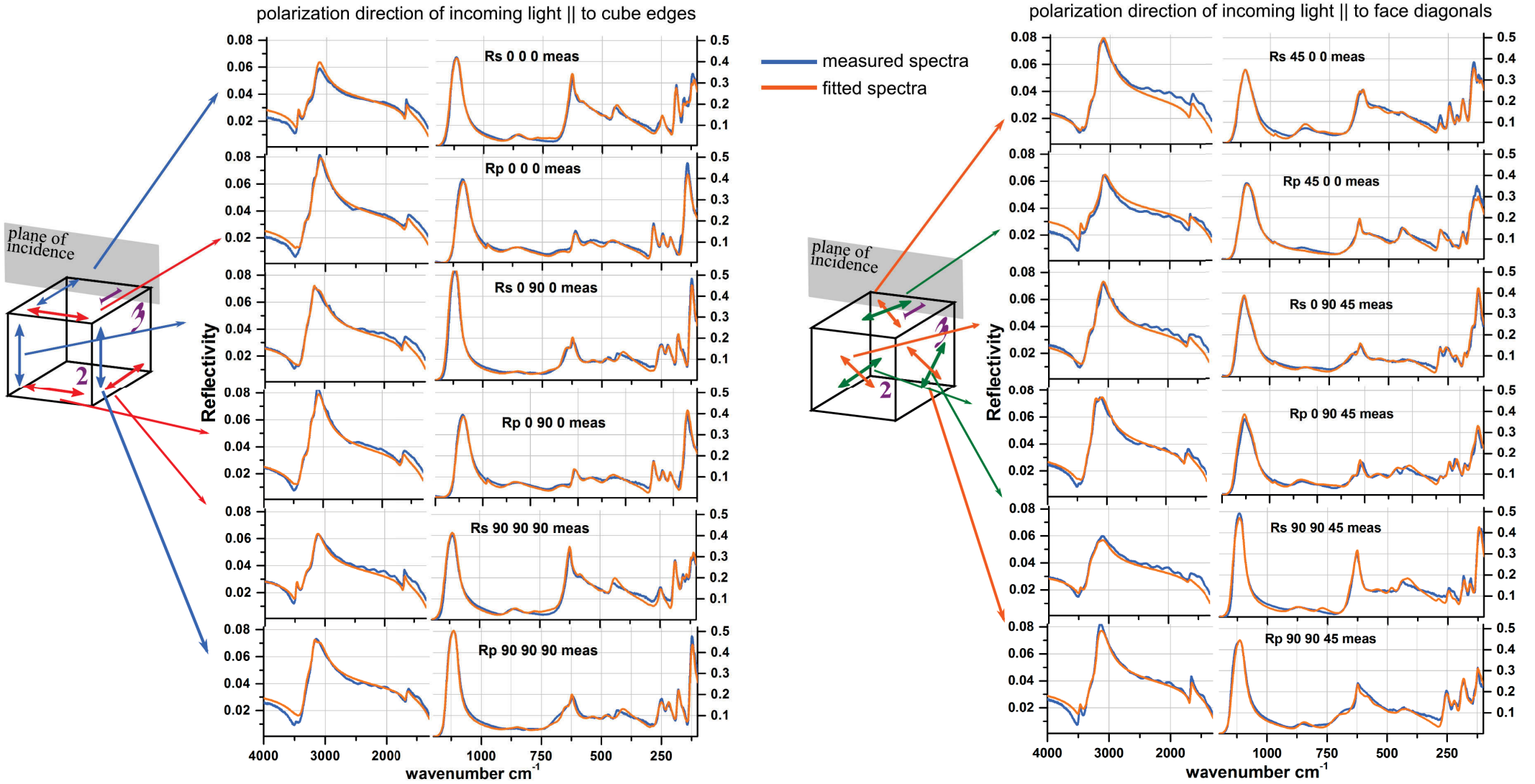

Fig. 4.1. Experimental (blue) and modeled (orange) spectra of the single crystal $CuSO_4 \cdot 5\,H_2O$ cube. Left: polarization direction of the incoming light parallel to the cube edges, right: polarization direction of the incoming light parallel to the cube face diagonals (for R_p-spectra the polarization direction has a small component normal to the surface due to incidence angle $>0°$).

The green and orange double arrows of the cube in the right part of the figure illustrate the polarization state of the incoming light to record the spectra of the cube face diagonals. The spectrum originating from each crystal face with corresponding polarization direction are assigned by the green and orange arrows.
Of the spectra it is noticeable that the spectra R_s 0 0 0 and R_s 90 90 90, R_p 0 0 0 and R_p 0 90 0 and R_s 0 90 0 and R_p 90 90 90 look pairwise very similar. This corresponds to orthorhombic spectral behavior, which indicates that $CuSO_4 \cdot 5\,H_2O$ is only "weakly" triclinic. An orthorhombic crystal with orientation of the crystal axes normal to cube faces shows the same pairwise identical spectra, but for an orthorhombic crystal also the spectra $R_{s/p}$ 45 0 0, $R_{s/p}$ 0 90 45 and spectra $R_{s/p}$ 90 90 45 are identical (for normal incidence and within misalignment errors). From the spectra of only the $CuSO_4 \cdot 5\,H_2O$ cube edges the crystal could be identified to be orthorhombic with the crystal axes more or less parallel to the cube edges, only the spectra of the face diagonals allow to differentiate the spectra of $CuSO_4 \cdot 5\,H_2O$ from spectra of an orthorhombic crystal.
Overall, there is a good agreement between measured and calculated spectra, but for some spectra there is a small discrepancy between measured and modeled spectra in the region from 400-300 cm^{-1}. Maybe this discrepancy originates from the polarizers, as both polarizers have their specification limit in this spectral region. Also is the interference pattern in the region at 1500-3000 cm^{-1} most probably introduced by the polarizers. For some other spectra there is a small discrepancy between measured and fitted spectra in the water region at 4000-1500 cm^{-1}. This discrepancy is most probably a systematic error as the reflectance of the cube faces is quite low (<10%).
Several test measurements concerning that problem showed that for low reflective samples the high wavenumber region the decrease of the reflectance is disproportionately higher than for the lower wavenumber region of the spectra.

4.2 Results of dispersion analysis for $K_2Cr_2O_7$

With $CuSO_4 \cdot 5\,H_2O$ we investigated a representative of a triclinic crystal which shows almost orthorhombic-like behavior in the IR spectral region due to only weakly distorted SO_4^{2-} tetrahedra. In contrary, $K_2Cr_2O_7$ single crystals showed much stronger anisotropic behavior as there are no high symmetry structural elements and therefore no triply degenerate vibrations. The oscillator parameters and dielectric background tensor found by dispersion analysis for $K_2Cr_2O_7$ are presented in tab. 4.2. The two crystallographic distinct dichromate ions cause pairs of vibrations like oscillators 13-20. According to [58] oscillators 9-12 in tab. 4.2 represent overlapping symmetric bending and scissor deformations of CrO_3, oscillators 13+14 can be assigned to the Cr-O-Cr symmetric bridge stretching vibration and oscillators 15+16 to the asymmetric bridge

	$\tilde{\nu}_j$	S_j	γ_j	Φ_j	Θ_j		$\tilde{\nu}_j$	S_j	γ_j	Φ_j	Θ_j
1	105.9	82.6	8.1	106.0	92.2	17	883.4	144.6	3.0	22.2	19.7
2	112.6	116.8	10.0	46.6	116.6	18	891.1	115.1	2.7	116.2	74.3
3	122.5	119.5	9.8	136.4	109.6	19	901.8	136.0	2.8	108.5	90.3
4	130.9	93.7	9.0	2.7	35.6	20	908.3	116.1	1.7	46.0	104.0
5	132.1	113.6	10.2	27.3	93.1	21	922.5	215.2	2.9	180.7	57.7
6	138.2	82.5	10.2	74.0	67.0	22	930.6	302.5	2.3	51.2	101.9
7	158.7	84.1	10.1	133.0	160.0	23	936.5	129.2	3.8	113.7	117.0
8	163.9	115.2	14.8	162.8	60.1	24	937.8	247.8	4.3	159.1	90.7
9	363.7	65.0	7.5	22.6	25.2	25	942.7	210.1	4.1	183.6	159.3
10	366.7	100.1	15.0	157.3	43.6	26	943.4	258.1	4.6	107.8	106.7
11	371.9	87.4	7.2	80.0	61.2	27	948.1	228.7	3.2	35.3	122.8
12	376.0	115.4	8.2	163.8	153.7	28	954.3	124.3	4.6	28.0	60.8
13	555.8	96.1	7.1	1.2	91.3	29	964.5	110.4	3.1	114.6	97.4
14	566.6	85.6	5.4	112.8	92.9						
15	744.1	480.5	11.4	33.1	29.9						
16	795.2	250.5	8.8	123.6	86.9						

$$\varepsilon_\infty = \begin{pmatrix} 2.90 & 0.13 & 0.06 \\ 0.13 & 2.76 & -0.13 \\ 0.06 & -0.13 & 2.37 \end{pmatrix}$$

Table 4.2. Oscillator parameters for a single $K_2Cr_2O_7$ crystal found by dispersion analysis. Resonance wavenumber $\tilde{\nu}_j$, strength S_j, damping constant γ_j are given in wavenumbers and the orientation angles Φ_j and Θ_j in degree. The dielectric background tensor is unitless.

stretching vibration. The symmetric out-of-phase and symmetric in-phase vibration of the CrO_3 compound are assigned to oscillators 17+18 and 19+20, respectively. The subsequent oscillators 21-29 with higher resonance wavenumbers include the CrO_3 asymmetric stretching vibrations. In the spectral region of the CrO_3 rocking and bending modes at ≈200-250 cm^{-1} no modes could be identified in the measured spectra, although Carter and Bricker [58] identified them with "very weak" intensity.
Of the 42 internal modes predicted by symmetry analysis at least 20 were found by dispersion analysis, as in the lower spectral region below oscillator 9 lattice modes overlap the internal modes, so further internal modes are not unambiguously identified. Here again the missing oscillators are either located outside the investigated spectral region below 100 cm^{-1} or could not be resolved by the fit routine either due to overlapping by other bands or due to too low intensity. The same holds for the 29 predicted external or lattice modes. Nevertheless, the resonance wavenumbers calculated by dispersion analysis agree well with the wavenumbers determined by Carter and Clark, except for oscillators 2, 4, 8, 22 and 23. As Carter and Clark showed no measured spectrum in their work, it is difficult to estimate why these oscillators have no counterpart in [58]
The 12 measured and fitted spectra of the single $K_2Cr_2O_7$ crystal are presented in fig 4.2. The left side of fig 4.2 shows the spectra recorded with polarization direction of the incoming light parallel to the cube edges, the spectra of the right side are recorded with polarization of the incident light parallel to the cube face diagonals.

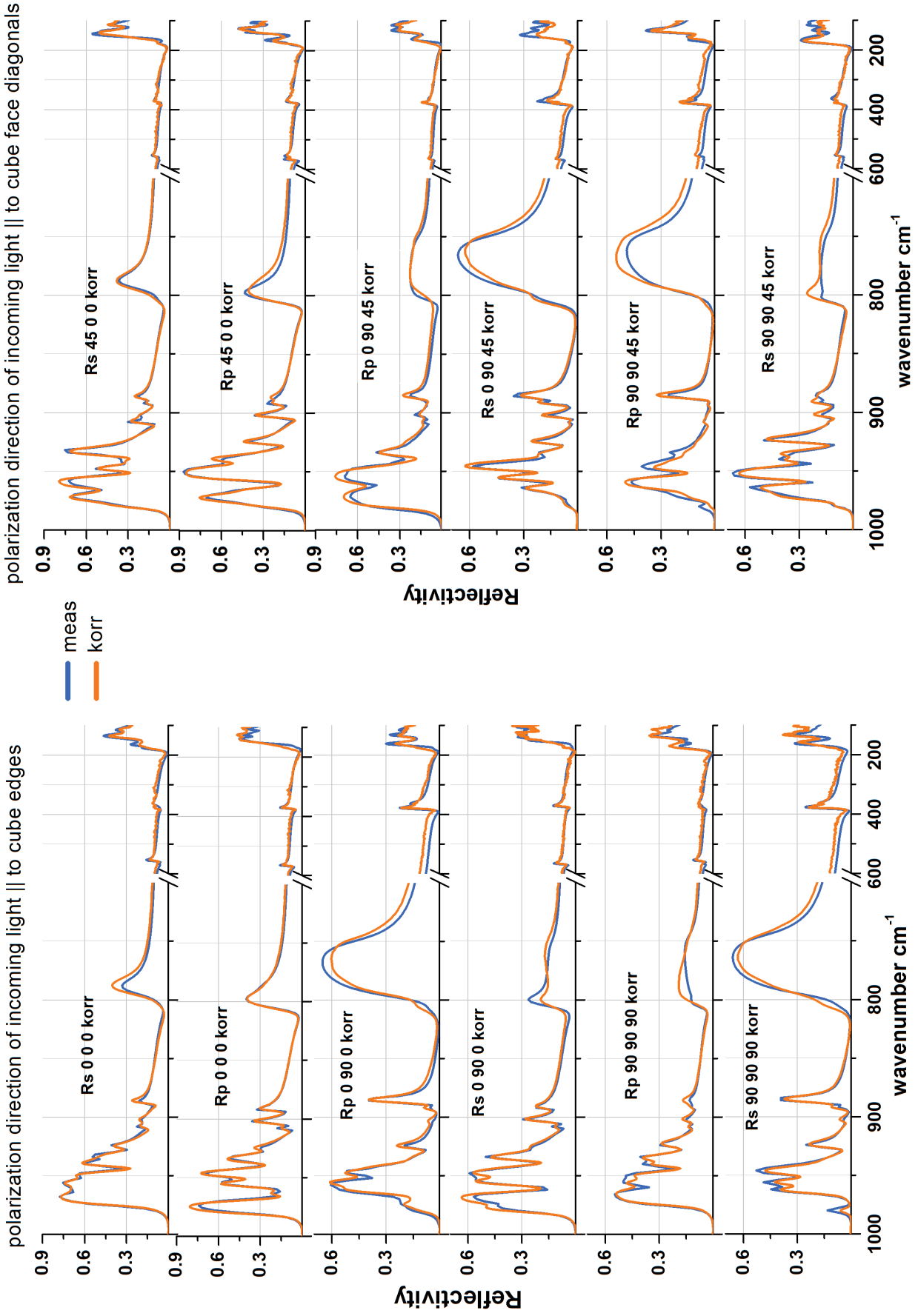

Fig. 4.2. Experimental (blue) and modeled (orange) spectra of the single crystal $K_2Cr_2O_7$ crystal. Left: polarization direction of the incoming light parallel to the cube edges, right: polarization direction of the incoming light parallel to the cube face diagonals.

To achieve a better agreement between the measured and fitted spectra (R_{fit}) a correction factor f_{corr} for the fitted spectra was introduced, according to $R_{corr}=f_{corr}\cdot R_{fit}$. In fig. 4.2 the corrected spectra R_{corr} are shown. The correction factor is a frequency independent, individual multiplication factor for each of the 12 spectra. They are employed to level out influences due to different surface qualities as the crystal faces were not polished or treated in any other way. The correction factors also support the fit to find more suitable values for the oscillator strength. For each of the spectra a different factor had to be introduced, not one for each of the four spectra originating from one crystal face, as it might seem intuitive. A possible reason for this necessity could be that on a rough surface scattering processes depend on the polarization state of the incoming light [59]. The correction factors for each spectrum are given in tab. 4.3. The correction factors can be integrated into the fit routine by two different ways: they can be fitted iteratively with the oscillator parameters, which is the better way if the reflectivities of the spectra recorded from one face vary as pronounced as it is the case for the $K_2Cr_2O_7$ crystal. They can also be fitted after having finished the optimization process of the oscillator parameters to improve the agreement between the fitted and measured spectra, which is the better way if the reflectivity of the spectra from one face vary less pronounced.
In contrary to the $CuSO_4{\cdot}5\,H_2O$ spectra each of the 12 measured spectra of the $K_2Cr_2O_7$ crystal is individual, the eigenvalues of the dielectric background tensor also show more anisotropy than for the $CuSO_4{\cdot}5\,H_2O$ crystal. Whereas the spectra of the $CuSO_4{\cdot}5\,H_2O$ crystal are dominated by the SO_4^{2-} ion, whose structure is not far from the original high symmetric tetrahedral structure, the spectra of the $K_2Cr_2O_7$ crystal are dominated by the dichromate ion $Cr_2O_7^{2-}$, which has C_{2v} symmetry as free molecule, a symmetry class with per se lower symmetry compared to tetrahedral symmetry.

spectrum	Rs 0 0 0	Rs 0 90 0	Rs 90 90 90	Rs 45 0 0	Rs 0 90 45	Rs 90 90 45
f_{corr}	1.10	1.02	0.76	1.11	0.92	0.76
spectrum	Rp 0 0 0	Rp 0 90 0	Rp 90 90 90	Rp 45 0 0	Rp 0 90 45	Rp 90 9045
f_{corr}	1.20	0.93	1.11	1.28	1.18	1.06

Table 4.3. Correction factors f_{corr} for the optimized spectra of $K_2Cr_2O_7$.

4.3 Comparison of orientation angles and dielectric function

Another aspect that identifies $K_2Cr_2O_7$ to be more anisotropic than $CuSO_4{\cdot}5\,H_2O$ is the distribution of the orientation angles Φ and Θ of the transition moments.
Fig 4.3 shows the histogram of the orientation angles within a step range of 10°, left for the transition moments of $CuSO_4{\cdot}5\,H_2O$, on the right side for the transition moments for $K_2Cr_2O_7$. The histogram for the angle Φ for $CuSO_4{\cdot}5\,H_2O$ shows a pronounced accumulation of counts for the angles 0°and 90°(Φ=180°equals to Φ=0°if the sign of the corresponding angle Θ is reversed). The histogram for the angle Θ still shows an accumulation at Θ=90°. The histogram of an orthorhombic crystal with the crystal axes parallel to the cube edges would show counts only at 0° and 90° for both Φ and Θ. In contrary, the histogram for $K_2Cr_2O_7$ the angle Θ shows a less pronounced accumulation at Θ=90°, and the values for the angle Φ cover roughly the complete angle range from 0-180°.

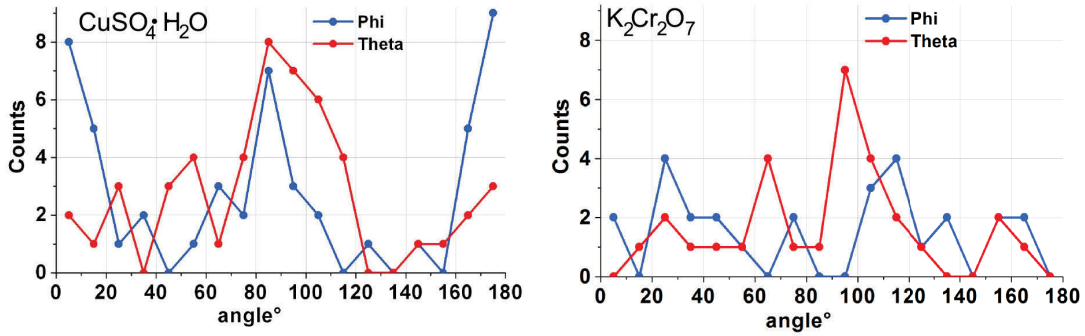

Fig. 4.3. Histogram of the orientation angles Φ and Θ of the transition moments for $CuSO_4{\cdot}5\,H_2O$ (left) and $K_2Cr_2O_7$ (right). The histogram shows the number of angles within an interval step of 10°.

Figures 4.4 and 4.5 show the components of the (relative) dielectric tensor function $\varepsilon/\varepsilon_0$ for $CuSO_4{\cdot}5\,H_2O$ and $K_2Cr_2O_7$. The off-axis elements of the dielectric function for $K_2Cr_2O_7$ are in the same range as the principal elements. For $CuSO_4{\cdot}5\,H_2O$ the real parts of the off-axis elements are roughly in the order of 10% of the values for the real parts of the principal elements. The imaginary parts of the off-axis and principal elements are in the same range.
Also, for $K_2Cr_2O_7$ the imaginary part of the principal elements resembles the form of the reflection spectra. For $CuSO_4{\cdot}5\,H_2O$ only the lower wavenumber region below $1200\,cm^{-1}$ is resembled by the imaginary part. The higher wavenumber region above $1200\,cm^{-1}$ is better resembled by the real part of the principal elements.
This behavior of the dielectric tensor functions is a measure for anisotropy and is an additional indication for $K_2Cr_2O_7$ being less orthorhombic than $CuSO_4{\cdot}5\,H_2O$.

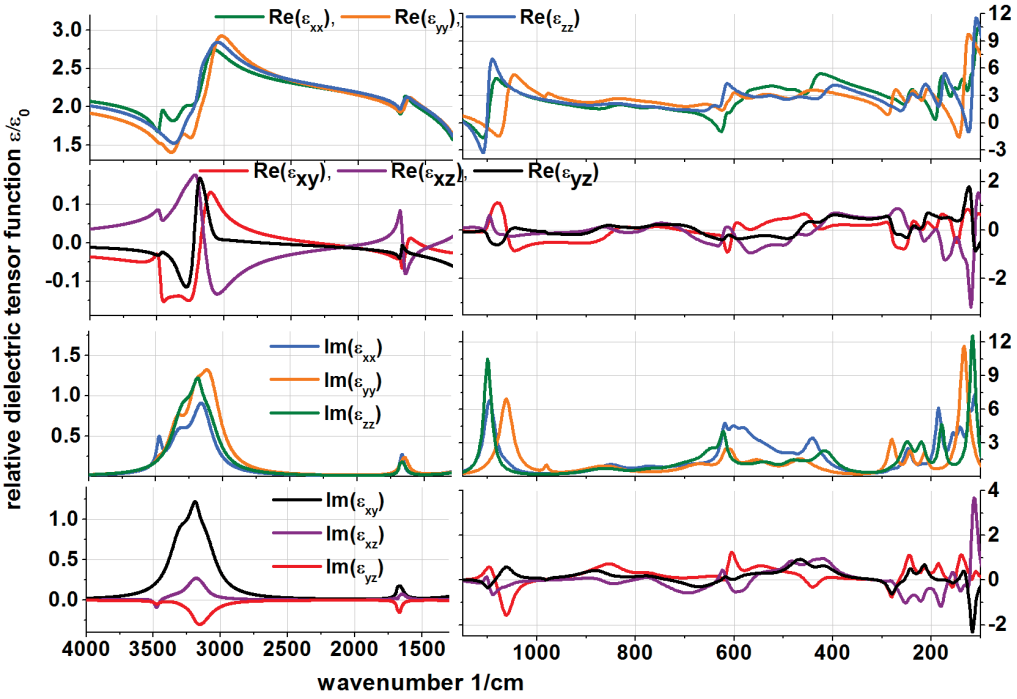

Fig. 4.4. Real and imaginary parts of the (relative) dielectric tensor function $\varepsilon/\varepsilon_0$ for $CuSO_4{\cdot}5\,H_2O$

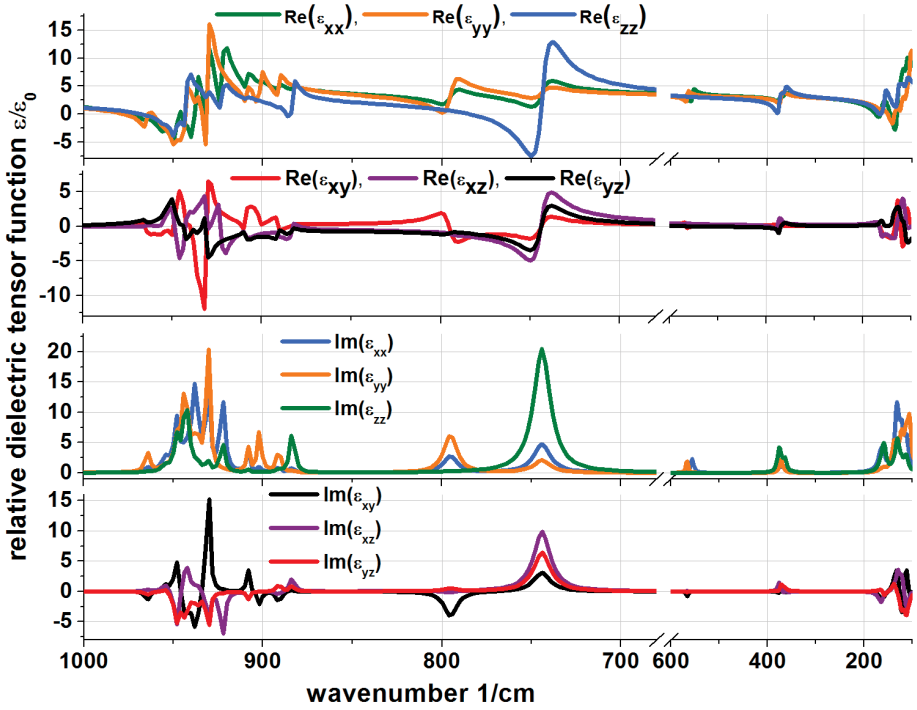

Fig. 4.5. Real and imaginary parts of the (relative) dielectric tensor function $\varepsilon/\varepsilon_0$ for $K_2Cr_2O_7$

4.4 Verification of oscillator parameters

To verify the dispersion parameters and therefore the dielectric tensor function, the dispersion parameters can be employed to simulate or predict other spectra. The predicted spectra can then be compared to the experimental ones. To do so a method relying on the comparison of simulated and measured spectra of polycrystalline samples especially developed and tested for low-symmetry materials [60] was used. Accordingly, fragments of both the $K_2Cr_2O_7$ and $CuSO_4{\cdot}5\,H_2O$ crystals were milled to powder with a mortar and pressed into a pellet. The advantage of a polycrystalline sample is that no further extensive orientation via x-ray analysis needs to be done and that all orientations contribute. Of these pellets the reflectance spectra R_s and R_p were measured. As expected for random orientations of the crystallites and low angle of incidence, the R_s and R_p spectra are very similar, therefore for fig. 4.6 and 4.7 only the R_s spectra of the pellets were chosen.

To model the R_s and R_p spectra, average spectra of the single crystal employing the dispersion parameters from tab. 4.1 and 4.2 were calculated on the one hand assuming large crystals with crystallite diameter $> \lambda/10$ and on the other hand assuming small crystals with crystallite diameter $< \lambda/10$. For large crystallites the reflection spectra were modeled with Average Reflection and Transmittance Theory (ARTT, [61]), which calculates the average over the individual reflections. For small crystallites the spectra were modeled with Average Refractive Index Theory (ARIT [60]), which is an average over the indices of refraction. Both modeling theories were applied using a large number of orientations.

For $CuSO_4{\cdot}5\,H_2O$ the modeled spectra with ARTT (red) and ARIT (black) differ in the intensity of the sulfate bands in the region of 1200-1000 cm^{-1} relative to the other

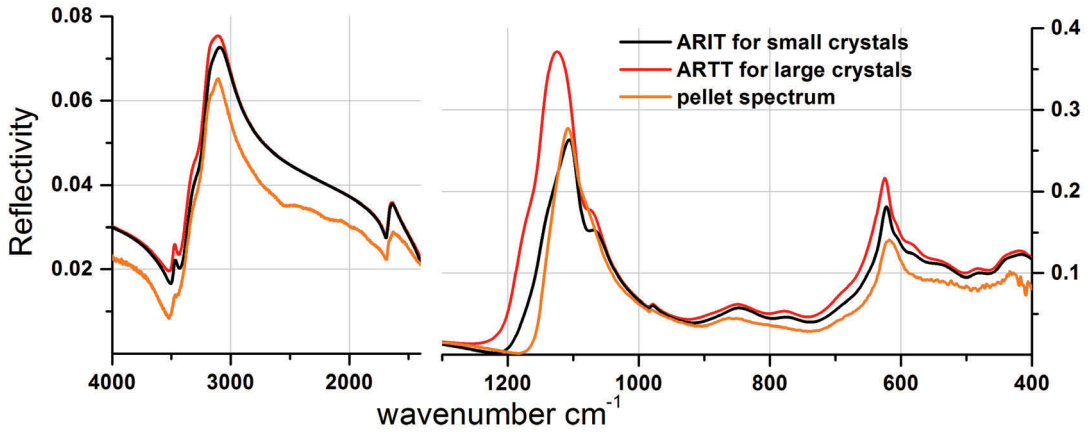

Fig. 4.6. Polycrystalline spectrum (orange) of a pressed pellet of $CuSO_4{\cdot}5\,H_2O$. The pellet spectrum corresponds more to the simulated ARIT spectrum (black) for small crystallites than to the ARTT spectrum (red) for large crystallites. To simulate the spectra the dispersion parameters of tab. 4.1 were employed.

bands (fig. 4.6), so the pellet spectrum is better resembled by ARIT. Therefore, the milled powder basically consists of small crystallites compared to the wavenumber.
For $K_2Cr_2O_7$ the ARTT and ARIT spectra differ in the band shape between 800 and 620 cm^{-1} (fig. 4.7). The $K_2Cr_2O_7$ pellet could not be modeled by averaging only over either the individual reflectances or by averaging only over the indices of refraction. Instead, the measured spectrum is modeled by a weighted average of small and large crystallite spectra. In this case the pellet consisted in a simplified assumption of roughly 70% small crystallites and 30% large crystallites. The multiplication factor 1.2 is to level out the different surface qualities of the pellet and the untreated crystal, since to the high pressure the surface of the pellet had a much better optical quality.
Band positions and shapes as well as relative intensities are satisfactorily captured for both the $CuSO_4 \cdot 5\,H_2O$ and $K_2Cr_2O_7$ pellet. The good agreement between measured and calculated spectra proves the dispersion parameters and thereby the dielectric tensor function as valid.
A comparison between the spectra of the polycrystalline sample and the spectra of the single crystals shows the necessity of the investigation of the single crystals, as the spectra of the polycrystalline samples show far less features than the spectra of the single crystals. In addition, all information concerning the directions of the transmission moments is naturally lost and can only be gained by proper dispersion analysis of a set of spectra of a single crystal sample.

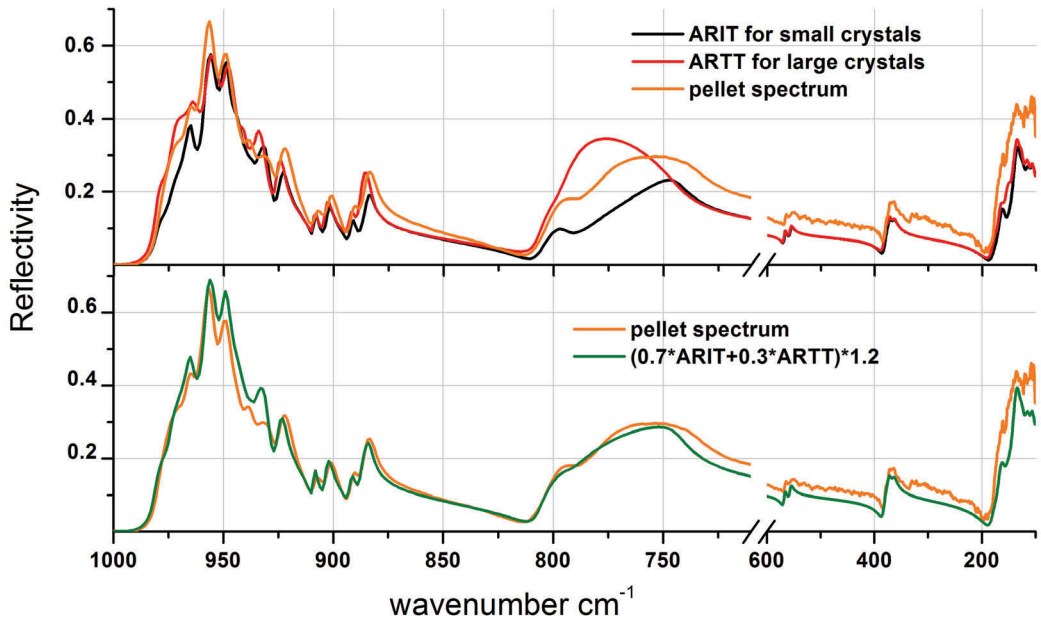

Fig. 4.7. Polycrystalline spectrum (orange) of a pressed pellet of $K_2Cr_2O_7$. The pellet spectrum corresponds neither completely to the ARIT (black) nor to the ARTT (red) spectrum, but is resembled approximately by a linear combination of both simulated spectra.

In summary, dispersion analysis of triclinic crystals can be successfully performed although due to the absence of any conditions concerning the orientation of transition moments large uncertainties of the fitted orientation angles depending on the proximity of the resonance wavenumbers are to be expected. Dispersion analysis can also distinguish between the degree of anisotropy. The fitted dispersion parameters predict the spectra of polycrystalline samples very well, yet it can happen that a polycrystalline sample needs to be described by a combination of ARTT and ARIT.
Inspired by the results found for triclinic crystals the measurement and evaluation scheme developed for triclinic crystals was extended to determine dispersion parameters for uniaxial, orthorhombic and monoclinic crystals with unknown arbitrary orientation. Since in such crystals the transition moments are oriented parallel to certain symmetry elements (rotation axes and mirror planes), it should be possible to find out by dispersion analysis not only the dispersion parameters, but simultaneously the crystal orientation and symmetry. Therefore, it should be possible to perform dispersion analysis without prior knowledge of structure and orientation, and without the necessity to orient the crystal prior to dispersion analysis. This kind of generalized dispersion analysis is introduced in the following chapters, starting the dispersion analysis of uniaxial crystals.

Chapter 5

Dispersion analysis of arbitrarily cut uniaxial crystals

5.1 Adaption of fit routine to uniaxial crystals

As described in chapter 2.4 the optical axis of an uniaxial crystal is the main symmetry axis with sixfold symmetry for hexagonal, threefold symmetry for trigonal and fourfold symmetry for tetragonal crystals. The main symmetry axis is the optical axis with the non-degenerate oscillators parallel to the axis. In the plane normal to the optical axis the degenerate oscillators are located, the oscillators of a twofold degenerate vibration being perpendicular to each other. For a crystal in principal cut, the dielectric tensor function can be split into two independent main components, $\varepsilon_{\perp}$ (dielectric function normal to the c-axis) and $\varepsilon_{||}$ (dielectric function parallel to the c-axis). As both spectral orientations are independent from each other and the spectra get evaluated separately, no orientation angles are necessary for the transition moments.
If however the crystal has *general* orientation, both degenerate and non-degenerate oscillator types create mixed spectra, that are not independent anymore, and the dielectric tensor function $\varepsilon_{x,y,z}$ takes on the same form as for triclinic crystals (cf. chapter 2.4)

$$\varepsilon_{x,y,z}(\tilde{\nu}) = \begin{pmatrix} \varepsilon_{\infty,xx} & \varepsilon_{\infty,xy} & \varepsilon_{\infty,xz} \\ \varepsilon_{\infty,yx} & \varepsilon_{\infty,yy} & \varepsilon_{\infty,yz} \\ \varepsilon_{\infty,zx} & \varepsilon_{\infty,zy} & \varepsilon_{\infty,zz} \end{pmatrix} + \sum_{j=1}^{N} \frac{S_j^2}{(\tilde{\nu}_j^2 - \tilde{\nu}^2) - i\gamma_j\tilde{\nu}} \times \mathbf{M}(\Phi_j, \Theta_j).$$

Due to the mutual dependency of the spectra the off-axis elements of the dielectric background tensor are different from zero now. For the oscillators the orientation angles have to be given again.
Nevertheless, some constraints still hold for the uniaxial crystals. In an arbitrarily cut uniaxial crystal the non-degenerate oscillators must have the same values for Φ and

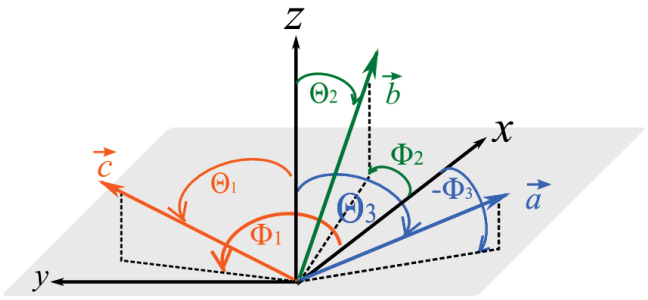

Fig. 5.1. Arrangement of oscillators in an arbitrarily cut uniaxial crystal. Orange: non-degenerate oscillators parallel to the c-axis, green and blue: pair of twofold degenerate oscillators perpendicular to each other and to the c-axis.

Θ, as they all point into the same direction. The twofold degenerate transition moments are oriented on the plane normal to the c-axis, both members of the degenerate oscillator pair have the same values for resonance wavenumber, strength and damping constant and are orthogonal to each other.

Translated to the optimization routine each pair of degenerate oscillator must fulfill an orthogonality condition with the oscillators perpendicular to the c-axis. Fig. 5.1 shows the arrangement of a non-degenerate oscillator (orange) parallel to the optical axis and a twofold degenerate oscillator pair with the two transition moments (green and blue) perpendicular to each other and the optical axis.

The transition moments parallel to the c-axis are represented by the vector $\vec{c}$ with orientation angles Φ_1 and Θ_1, the two members of the degenerate oscillator pair are represented by the vector $\vec{a}$ with orientation angles Φ_3 and Θ_3 and vector $\vec{b}$ with Φ_2 and Θ_2, respectively. The components of the orientation angles in spherical coordinates are (neglecting the magnitude of the vectors):

$$\vec{c} = \begin{pmatrix} \sin\Theta_1 \cdot \cos\Phi_1 \\ \sin\Theta_1 \cdot \sin\Phi_1 \\ \cos\Theta_1 \end{pmatrix}, \vec{a} = \begin{pmatrix} \sin\Theta_3 \cdot \cos\Phi_3 \\ \sin\Theta_3 \cdot \sin\Phi_3 \\ \cos\Theta_3 \end{pmatrix}, \vec{b} = \begin{pmatrix} \sin\Theta_2 \cdot \cos\Phi_2 \\ \sin\Theta_2 \cdot \sin\Phi_2 \\ \cos\Theta_2 \end{pmatrix} \tag{5.1}$$

The orthogonality condition requires that the dot product between the three vectors vanishes

$$\frac{\vec{a}\cdot\vec{b}}{|\vec{a}|\cdot|\vec{b}|} \stackrel{!}{=} 0, \qquad \frac{\vec{a}\cdot\vec{c}}{|\vec{a}|\cdot|\vec{c}|} \stackrel{!}{=} 0, \qquad \frac{\vec{c}\cdot\vec{b}}{|\vec{c}|\cdot|\vec{b}|} \stackrel{!}{=} 0. \tag{5.2}$$

Solving equation (5.2) leads to expressions for the orientation angles Θ_2, Φ_3 and Θ_3 as function of the angles Φ_1, Θ_1 and Φ_2. The index k indicates the kth degenerate oscillator pair,

$$\begin{aligned} \Theta_{2k} &= \arctan\left(\frac{-1}{\tan\Theta_1 \cdot \cos(\Phi_{2k} - \Phi_1)}\right) \\ \Phi_{3k} &= \arctan\left(\frac{\tan\Theta_1 \cdot \cos\Phi_1 - \tan\Theta_{2k} \cdot \cos\Phi_{2k}}{\tan\Theta_{2k} \cdot \sin\Phi_{2k} - \tan\Theta_1 \cdot \sin\Phi_1}\right) \\ \Theta_{3k} &= \arctan\left(\frac{-1}{\tan\Theta_1 \cdot \cos(\Phi_{3k} - \Phi_1)}\right). \end{aligned} \tag{5.3}$$

The angles that get optimized by the optimization routine are Φ_1, Θ_1 of the non-degenerate oscillators and the one orientation angle of the degenerate oscillators, Φ_2. The angles Θ_2, Φ_3 and Θ_3 are fixed by equation 5.3. In uniaxial crystals there is no predominant direction for the vibrations normal to the c-axis, each pair of oscillators corresponding to a degenerate vibration has different angles (Φ_2, Θ_2) and (Φ_3, Θ_3).
In the first step the fit is performed without constraints, like for a triclinic crystal (cf. chapter 2.8). This first step is done to get an overview over the number of oscillators in the spectra and find suitable values for their parameters.
During the optimization process in the first step two different classes of oscillators emerge: One class of oscillators occurs singly, but mostly pointing into arbitrary directions. These oscillators are assumed to be the oscillators parallel to the optical axis. The second class of oscillators occurs in pairs with roughly the same values for resonance wavenumber, strength and damping constant. These oscillators are treated as the degenerate oscillators, although they do not necessarily have to be mutual orthogonal or orientated normal to the single oscillators.
In the second step the constraints of equation 5.3 derived from the symmetry of uniaxial crystals are applied to the fit. All the oscillators that are assumed to be non-degenerate are fitted with the same angle pair Φ_1 and Θ_1. Each of the oscillator pair is fitted with the same resonance wavenumber, strength and damping constant, respectively. The orientation angles are constrained to being normal to the non-degenerate oscillators and mutual orthogonal. The arrangement of the oscillators in the unconstrained and constrained fit is schematically depicted in fig 5.2. During the unconstrained fit procedure it also appears that two oscillators that come out as pair and a third oscillator also has the same parameters as the degenerate oscillator pair, so they belong to an originally threefold degenerate vibration.

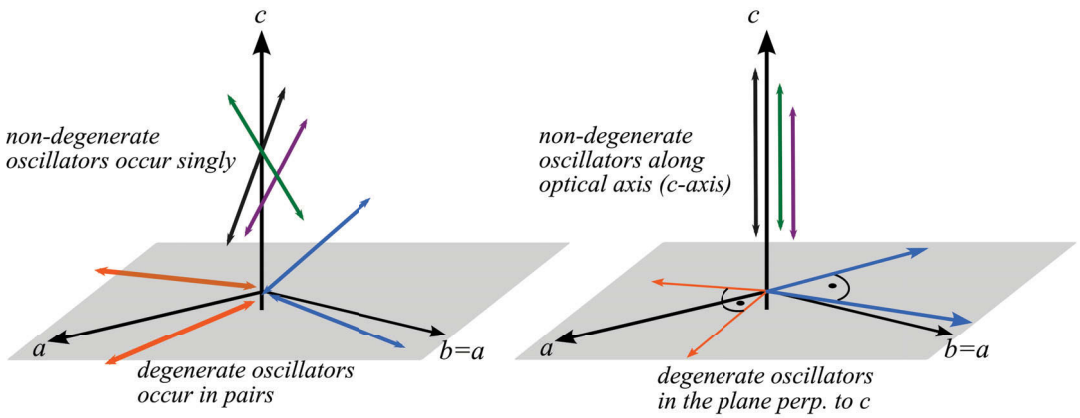

Fig. 5.2. Arrangement of oscillators in the unconstrained (left) and constrained (right) fit routine. The non-degenerate oscillators found by the unconstrained routine do not necessarily have to be parallel to each other, as well as the degenerate oscillators need not to be arranged in the plane normal to the internal z-axis.

This case occurs for e.g. the asymmetric stretching vibration of SiO_4^{2-} in quartz. Of such an oscillator triple any of the oscillators can be chosen to be parallel to the optical axis, the other two are then sorted into the twofold degenerate oscillator class.
Also the dielectric background tensor must fulfill now certain constraints. As the constrained fit routine gives the orientation of the c-axis, the crystal is treated as being a principal cut. Therefore for the dielectric background tensor the conditions $\varepsilon_{xx} = \varepsilon_{yy}$ and vanishing off-axis elements are introduced. To respect the arbitrary cut of the crystal the dielectric background tensor in diagonal form is transformed by a rotation matrix $\mathbf{M}_{rot}$ that rotates the dielectric background tensor back into the orientation of the arbitrary cut with the optical axis aligned parallel to c.
For this, equation (5.1) takes the form

$$\begin{aligned}\varepsilon_{x,y,z}(\tilde{\nu}) &= \mathbf{M}_{rot} \cdot \begin{pmatrix} \varepsilon_{\infty,\perp} & 0 & 0 \\ 0 & \varepsilon_{\infty,\perp} & 0 \\ 0 & 0 & \varepsilon_{\infty,||} \end{pmatrix} \cdot \mathbf{M}_{rot}^{-1} \\ &\quad + \sum_{j=1}^{N} \frac{S_j^2}{(\tilde{\nu}_j^2 - \tilde{\nu}^2) - i\gamma_j\tilde{\nu}} \cdot \mathbf{M}(\Phi_j, \Theta_j) \end{aligned} \tag{5.4}$$

with the rotation matrix

$$\mathbf{M}_{rot} = \begin{pmatrix} \cos\Phi & -\sin\Phi\cos\Theta & \sin\Theta\sin\Phi \\ \sin\Phi & \cos\Theta\cos\Phi & -\sin\Theta\cos\Phi \\ 0 & \sin\Theta & \cos\Theta \end{pmatrix}. \tag{5.5}$$

The rotation matrix describes a rotation around the internal z-axis (describes by the angle Φ) followed by a rotation around the internal x-axis (described by the angle Θ). The angles Φ and Θ of $\mathbf{M}_{rot}$ are the orientation angles of the optical axis. As the oscillator strength and the values for the dielectric background tensor influence each other, also the constrained fit should be performed by alternately optimizing the dielectric background and the oscillator parameters.

5.2 Results of dispersion analysis for quartz

Tab. 5.1 shows the oscillator parameters for the unconstrained fit, in which the crystal is treated like a triclinic crystal without conditions concerning the orientation of the transition moments. The angles in the last column are the angles between the two members of a degenerate oscillator pair.
The oscillators are listed in two groups, oscillators given in italic are the ones that occur singly with no complementary partner. Already in the unconstrained fit these

	$\tilde{\nu}_j$ cm^{-1}	S_j cm^{-1}	γ_j cm^{-1}	$\Phi_j{}^\circ$	$\Theta_j{}^\circ$	angle of deg. oscillator pair
1	*1070.9*	*873.7*	*7.5*	*45.1*	*43.9*	
2	*775.9*	*255.0*	*6.3*	*40.7*	*52.2*	
3	*494.6*	*424.2*	*4.0*	*39.4*	*50.0*	
4	*363.3*	*299.2*	*4.5*	*41.4*	*52.4*	
5	1160.6	109.0	8.7	119.9	124.1	
	1160.7	111.9	10.2	-1.0	117.8	96.5°
6	1065.2	889.5	10.7	97.6	120.4	
	1063.3	873.5	7.0	-11.1	118.3	90.2°
7	794.7	274.2	7.4	-12.6	125.7	
	795.1	271.0	6.5	103.0	121.2	90.0°
8	694.7	102.5	7.0	-9.3	128.3	
	694.0	96.3	7.8	91.9	131.8	72.5°
9	449.7	409.8	3.0	-6.9	130.3	
	449.6	413.8	3.4	107.0	115.7	89.9°
10	393.0	240.5	2.4	98.3	123.7	
	393.6	228.2	2.2	-16.9	123.0	89.7°
11	263.5	60.4	6.0	-9.6	119.4	
	262.6	60.3	6.0	88.3	116.0	83.8°

Eigenvalues of ε_∞=2.33, 2.50, 2.55

Table 5.1. Oscillator parameters wavenumber $\tilde{\nu}_j$, strength S_j and damping constant γ_j of calculated with the unconstrained fit routine. The eigenvalues of the ε_∞ give the tensor in principal form. The two almost identical values describe the dielectric background $\varepsilon_{\infty,\perp}$ normal to the c-axis, the third describes the dielectric background $\varepsilon_{\infty,||}$ parallel to the c-axis.

oscillators show the same orientation within a few degrees. The other oscillators occur in pairs and also have very similar values for resonance wavenumber, strength and damping constant. Except for oscillator 8 they already are mutually orthogonal. Oscillator 8 has a comparatively low intensity; oscillators with low intensities are generally more difficult to catch in the fitting process than intense oscillators.

Tab. 5.2 gives the oscillator parameters as they resulted from the constrained fit routine. Of the 12 IR active vibrations only the librational vibration at $128\,\mathrm{cm}^{-1}$ was not visible [62] in the reflection spectra. The calculated orientation of the c-axis with $(\Phi, \Theta)=(39\pm2^\circ, 51\pm2^\circ)$ of the constrained fit is in good agreement with the orientation found by x-ray analysis with $(\Phi, \Theta)=(42\pm2^\circ, 51\pm2^\circ)$. The error in the orientation angles also includes inaccuracies of the crystal cut. In tab. 5.3 some reference values determined by Spitzer and Kleinman using the same oscillator model [63] for comparison with the fitted parameters are given. Spitzer et al. fitted the spectra by the method of successive trials and adjustment of parameters and used three redundant oscillators to obtain a best possible agreement between their fitted and measured spectra. As no significant improvement of the fit including more oscillators was detectable, the additional oscillators from Spitzer and Kleinman have no corresponding oscillators in tab. 5.1 and 5.2. The fitted oscillators in tab. 5.2 and 5.3 are in very good agreement, the variation between some corresponding oscillators (e.g. the strength for oscillator 1) is within calculation errors.

The two eigenvalues of the dielectric background tensor in tab. 5.1 that describe $\varepsilon_{\infty,\perp}$

	$\tilde{\nu}_j$ cm^{-1}	S_j cm^{-1}	γ_j cm^{-1}	$\Phi_j{}^\circ$	$\Theta_j{}^\circ$
1	*1067.2*	*873.7*	*9.3*	*39.1*	*51.2*
2	*775.8*	*255.0*	*6.4*	*39.1*	*51.2*
3	*493.9*	*424.2*	*4.3*	*39.1*	*51.2*
4	*363.5*	*299.2*	*4.9*	*39.1*	*51.2*
5	1160.7	109.0	8.6	119.9	-78.7
6	1063.5	889.5	10.5	97.6	-57.0
7	795.0	274.2	7.4	-12.6	-52.4
8	694.8	102.5	7.0	-9.3	-50.5
9	450.4	409.8	3.0	-6.9	-49.1
10	393.0	240.5	2.7	98.3	-57.5
11	263.5	60.4	6.0	-9.6	-50.6

$\varepsilon_{\infty,||}$=2.37, $\varepsilon_{\infty,\perp}$=2.48

Table 5.2. Results of dispersion analysis performed with the constrained fit routine for quartz. The dielectric tensor is rotated during the fit routine into principal form, so the values for $\varepsilon_{\infty,||}$ and $\varepsilon_{\infty,\perp}$ are explicitly computed.

	$\tilde{\nu}_j$ cm^{-1}	S_j cm^{-1}	γ_j cm^{-1}
	1220	*128*	*183*
1	*1080*	*884*	*8*
2	*778*	*246*	*7*
	539	*42*	*22*
	509	*114*	*7*
3	*495*	*402*	*5*
4	*364*	*300*	*5*
	1227	116	135
5	1163	116	7
6	1072	877	8
7	797	246	7
8	697	93	8
9	450	407	4
10	394	226	3

$\varepsilon_{\infty,||}$=2.38, $\varepsilon_{\infty,\perp}$=2.36

Table 5.3. Dispersion parameters for quartz calculated by Spitzer and Kleinman [63]. As they investigated two independent spectra no orientation angles are given.

are equal within calculation errors ($\pm$0.1), and also agree with $\varepsilon_{\infty,\perp}$ found by the constrained fit, yet the values are too high compared to $\varepsilon_{\infty,\perp}$ given by Spitzer and Kleinman. The dielectric backgrounds $\varepsilon_{\infty,||}$ of the three tables agree well with each other. Comparing oscillators 1 and 6 in tab. 5.2 and 5.3, the resonance wavenumbers for these oscillators differs by 13 cm^{-1} and 10 cm^{-1}. As they are very intense oscillators, this difference in wavenumber is sufficient to increase the fitted value for the dielectric background from 2.38 to 2.5.

The measured spectra together with the spectra calculated with the oscillator parameters of tab. 5.2 are presented in fig. 5.3. Band assignment of the SiO_4 vibrations in the figure is taken from Williams [64]. With the help of the spectra some conclusions about the orientation of the optical axis can also be made without any calculations. The spectra recorded with the polarization direction of the incoming light parallel to the cube edges (left spectra of fig. 5.3) look very similar, which means that the optical axis is most probably oriented parallel to a cube space diagonal. With this two spectra of the cube face diagonals must be recorded with polarization direction of the incident light parallel and normal to the projection of the optical axis.

The spectra also reveal which oscillators belong to the same class. The vibrations at 360, 520 and 780 cm^{-1} (red framed) are present in spectra R_s 45 0 0, R_p 0 90 45 and R_s 90 90 45 and are vanished in the spectra recorded with orthogonal polarization of the incident light to that spectra, namely spectra R_p 0 90 45, R_s 0 90 45 and R_p 90 90 45. These vibrations appear in all spectra recorded with polarization direction of the incident light parallel to the cube face diagonals with the same varying intensity. As these vibrations show the same spectral behavior, they belong to the same class.

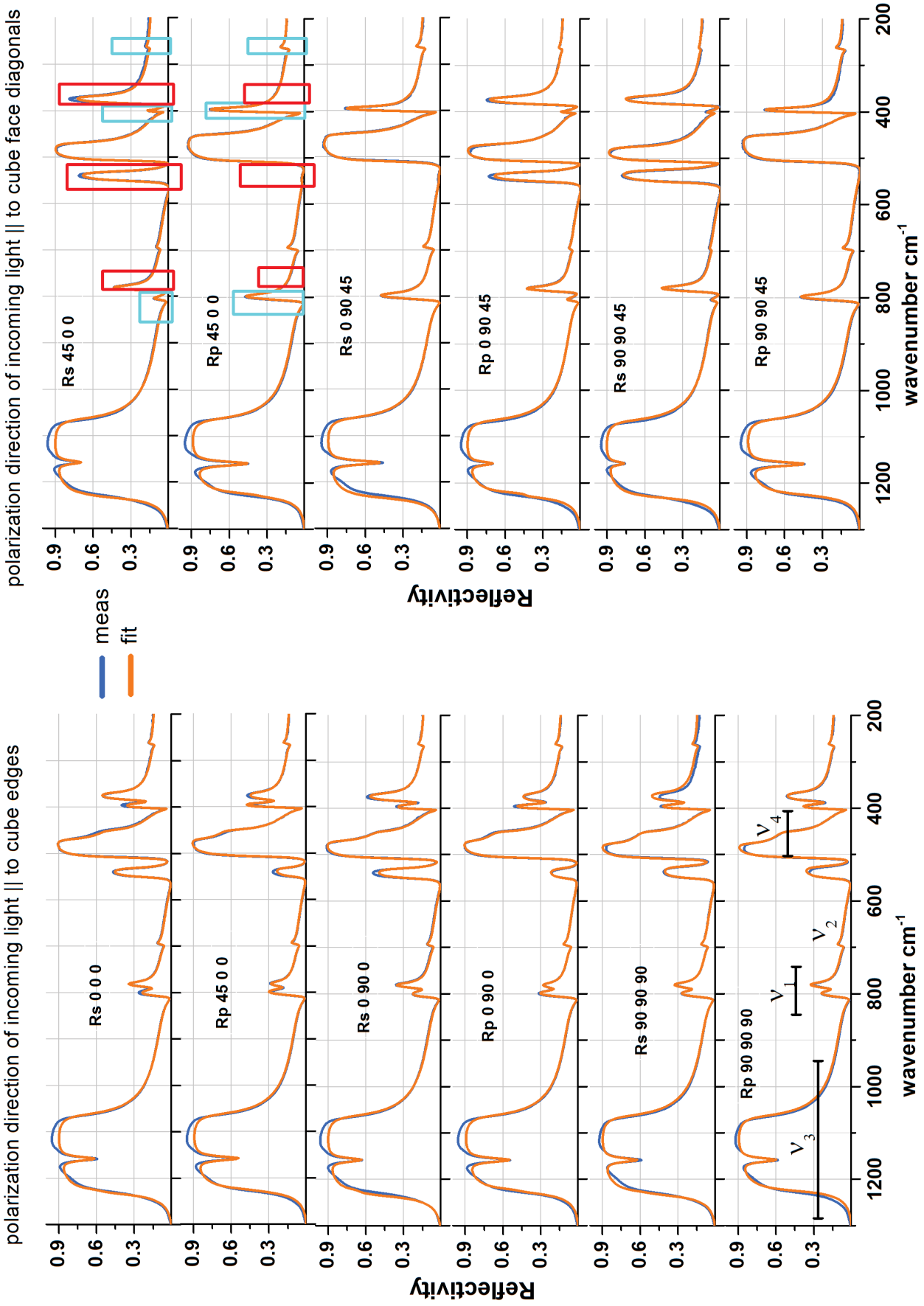

Fig. 5.3. Measured (blue) and calculated (orange) reflection spectra for quartz. Left: polarization direction of the incoming light parallel to the cube edges, right: polarization direction of the incoming light parallel to the cube face diagonals.

The transition moments of the vibrations at 260, 400 and 800 cm^{-1} (blue framed) must be oriented normal to the transition moments of the vibrations at 360, 520 and 780 cm^{-1} as they are present in the spectra the latter vibrations vanish, and vice versa. Although one cannot derive if a vibration is non- or twofold degenerate by the visual evaluation of the spectra, the assignment of vibrations that belong to the same group is very helpful to rate the fit results. That the blue framed vibrations do not vanish completely in spectra R_s 45 0 0, R_p 0 90 45 and R_s 90 90 45 may be a hint that the vibrations are the twofold degenerate vibrations, but this can also be result of the optical axis not being exactly oriented along a cube space diagonals.
The nearly isotropic spectral region between 840 and 1300 cm^{-1} is created by the (originally) threefold degenerate ν_3 asymmetric stretching vibration of the SiO_4^{2-} tetrahedron. This vibration is generated by the oscillators 1 and 6 in tab. 5.2. The same holds for the ν_4 asymmetric bending vibration at 400-500 cm^{-1} which is represented by oscillators 3 and 9 in tab. 5.2. Due to the asymmetric shape of Lorentz bands oscillator 5 of tab. 5.2 seems to contribute a negative strength and creates a dip in the spectral region of the ν_3 vibration (cf. chapter 2.8).
The free SiO_4 ion with T_d symmetry has 4 normal modes which are described in tab. 5.4, but environments with non-tetrahedral symmetries can also cause IR-activity of modes, that are only Raman-active for the free molecule [65]. The resonance wavenumbers of the SiO_4 vibrations in quartz are given in tab. 5.4 (also marked in the figure).

number	symmetry	motion	spectral range free ion	spectral range in quartz
ν_1	A_1 (Raman)	symmetric stretching	800-950 cm^{-1}	780-800 cm^{-1}
ν_2	E, δ_s (Raman)	symmetric bending	300-500 cm^{-1}	695 cm^{-1}
ν_3	F_2, ν_{as} (IR+Raman)	asymmetric stretching	850-1200 cm^{-1}	1080-1175 cm^{-1}
ν_4	F_2, δ_{as} (IR+Raman)	asymmetric bending	400-600 cm^{-1}	494 cm^{-1}

Table 5.4. Wavenumbers of the normal modes of the free SiO_4 ion and the SiO_4 in quartz.

5.3 Results of dispersion analysis for calcite

The oscillator parameters of the constrained fit for calcite are listed in tab. 5.6. The orthogonality condition has pulled the fit into the right direction, the correct orientation of the c-axis was found although the results of the unconstrained fit lack any information concerning the orientation.

To compare the fitted results to some literature values the parameters found by Lane, who also used the Lorentz oscillator model [66], are given in tab. 5.7. Lane also fitted three redundant oscillators with very low strength to gain a better agreement between fitted and measured spectra, therefore they have no counterpart in tab. 5.6. The calculated resonance wavenumbers in tab. 5.6 are in very good agreement with the wavenumbers found by Lane, only the oscillator strengths and damping constants vary a little for some oscillators. Also the values for $\varepsilon_{\infty,||}$ and $\varepsilon_{\infty,\perp}$ found by dispersion

$\tilde{\nu}_j$ cm^{-1}	S_j cm^{-1}	γ_j cm^{-1}	$\Phi_j{}^\circ$	$\Theta_j{}^\circ$
1403.0	1034.6	12.3	113.5	116.7
1404.4	1035.6	13.7	4.3	-56.6
870.1	247.7	1.9	44.1	48.7
301.7	345.6	10.5	3.6	-35.5
302.9	347.3	11.7	98.1	96.3
307.4	351.9	13.7	7.2	57.9
225.0	184.7	7.9	-34.6	-75.2
226.7	179.9	7.9	66.1	132.2
98.2	163.2	4.7	4.9	-20.0
100.9	159.0	5.1	87.2	84.2
98.9	164.1	5.0	-2.9	67.3

Eigenvalues of ε_∞=2.05, 2.58, 2.63

Table 5.5. Oscillator parameters and eigenvalues of dielectric background tensor calculated by unconstrained fit routine for calcite. The eigenvalues of the tensor are equivalent to the tensor in diagonal form.

	$\tilde{\nu}_j$ cm^{-1}	S_j cm^{-1}	γ_j cm^{-1}	$\Phi_j{}^\circ$	$\Theta_j{}^\circ$
1	*870.1*	*245.1*	*2.0*	*52.4*	*45.2*
2	*303.9*	*351.1*	*16.3*	*52.4*	*45.2*
3	*99.0*	*167.4*	*3.5*	*52.4*	*45.2*
4	1404.2	1032.8	12.6	26.4	-47.9
5	712.5	76.8	2.9	52.4	-43.5
6	303.2	351.3	10.5	42.4	-45.3
7	224.3	196.2	8.6	25.3	-48.2
8	100.2	158.3	5.0	-21.7	-74.6

$\varepsilon_{\infty,||}$=2.10, $\varepsilon_{\infty,\perp}$=2.58

Table 5.6. Oscillator parameters and principal values of dielectric background calculated by the constrained fit

	$\tilde{\nu}_j$ cm^{-1}	S_j cm^{-1}	γ_j cm^{-1}
1	*871*	*246*	*2*
	848	*53*	*6*
2	*305*	*355*	*9*
3	*95*	*203*	*7*
4	1404	1070	9
	891	28	4
5	712	90	5
	380	43	228
6	298	388	10
7	223	223	11
8	102	188	6

$\varepsilon_{\infty,||}$=2.21, $\varepsilon_{\infty,\perp}$=2.75

Table 5.7. Oscillator parameters and dielectric background for calcite found by Lane [66].

analysis of both the unconstrained and constrained fit routine agree with each other, yet they are a little lower than those given by Lane. But they reflect the much more pronounced birefringence in calcite than in quartz. The little lower values for the dielectric background is still in the region of calculation accuracy. In tab. 5.6 and 5.7 the strength for the very intense oscillator at $\approx$1404 cm^{-1} differ by 40 cm^{-1}, which also influences the fitted values for the dielectric background.

The calcite spectra are characterized by two different spectral regions. The region from 600 to 100 cm^{-1} seems quite isotropic, the other part of the spectra from 1600-600 cm^{-1} shows some anisotropy. This is reflected in the oscillator parameters found by the unconstrained fit in tab. 5.5. In contrary to quartz no predominant direction developed during the fitting process. Only one oscillator occurs singly, two oscillators occur in pairs and the remaining six oscillators seem to belong to two oscillator triples. The single oscillator must definitely be a non-degenerate oscillator, as the spectral distance to the neighbor oscillators is too large to form a pair or triple of degenerate vibrations.

The measured and fitted spectra using the parameters of the constrained fit in tab. 5.6 are depicted in fig. 5.4. The spectra clearly show vibrations that are orthogonal to each other. For example in the R_s 0 90 45 spectrum the intense vibration centered at $\approx$ 1450 cm^{-1} creates a strong signal, which almost vanishes if the polarization of the incoming light is rotated by 90°for the R_p 0 90 45 spectrum (marked in the figure). The vibration at 870 cm^{-1} shows a strong signal in R_p 0 90 45, which is vanished in spectrum R_s 0 90 45.

Analogously to the quartz spectra some information about the orientation of the c-axis can be gained without performing dispersion analysis. The calcite spectra recorded parallel to the cube edges bear more resemblance to each other than the spectra recorded with the polarization direction parallel to the face diagonals, so the c-axis must lie in the vicinity of the cube diagonal. The three IR-active internal modes of CO_3^{2-} [32] are the twofold degenerate deformation vibration (δ) at 712 cm^{-1}, the asymmetric stretching vibration (ν_{as}) at 1404 $\mathrm{cm}^{-1}$and the out-of-plane deformation (γ) at 870 cm^{-1}. The vibrations are also depicted in fig. 5.4. This is in accordance with the results of the optimization routine, that sorted the oscillators correctly into the degenerate and non-degenerate classes. The remaining vibrations are combinations of librational and translational modes [43]. The twofold degenerate asymmetric stretching vibration of the CO_3^{2-} molecule is, contrary to the asymmetric stretching vibration of SiO_4^{2-}, a two dimensional vibration and therefore more sensitive to misalignment errors. Nevertheless, the calculated orientation of the c-axis with (Φ, Θ)=(52$\pm$2°, 45$\pm$2°) is in absolute agreement with the orientation determined by x-ray analysis (Φ, Θ)=(51$\pm$2°, 44$\pm$2°).

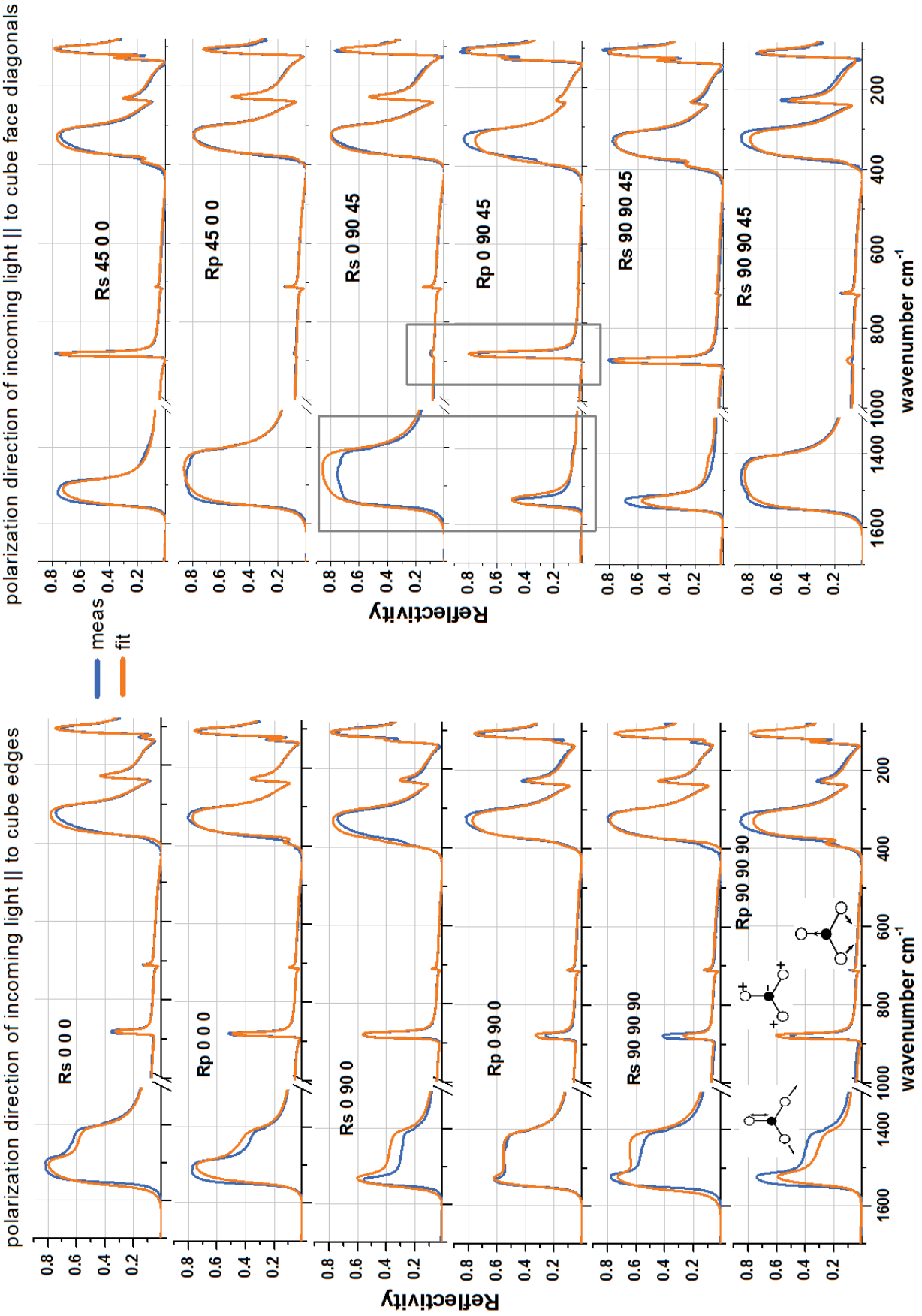

Fig. 5.4. Measured (blue) and calculated (orange) reflection spectra for calcite. Left: polarization direction of the incoming light parallel to the cube edges, right: polarization direction of the incoming light parallel to the cube face diagonals.

5.4 Results of dispersion analysis for lithium niobate

The crystal structure of $LiNbO_3$ is dominated by octahedral units, which is reflected by the oscillator parameters found by dispersion analysis. The parameters of the unconstrained fit are presented in tab. 5.8. The octahedral compounds cause mainly intense and broad bands, e.g. by oscillator pairs 7, 11, 13 or oscillators 2 and 4. The parameters of the non-degenerate oscillators found by the unconstrained fit do not even rudimentary point into the same direction. The variation of the parameters of a degenerate oscillator pair is also much more pronounced as it is the case for quartz or calcite. Nevertheless, most of the oscillator pairs are mutual orthogonal already in the unconstrained fit routine.

	$\tilde{\nu}_j$ cm^{-1}	S_j cm^{-1}	γ_j cm^{-1}	$\Phi_j{}^\circ$	$\Theta_j{}^\circ$	angle of deg. oscillator pair
1	*726.1*	*156.1*	*43.0*	*96.4*	*83.5*	
2	*616.5*	*1044.6*	*43.2*	*41.9*	*116.0*	
3	*324.3*	*233.3*	*13.7*	*79.2*	*90.0*	
4	*257.5*	*976.4*	*27.0*	*44.6*	*120.1*	
5	837.1	24.6	15.3	8.7	88.9	
	829.7	30.4	15.5	0.0	0.6	88°
6	685.6	235.1	36.1	-11.5	106.1	
	687.2	287.3	38.0	-0.7	-7.0	113°
7	579.5	1013.9	47.6	-55.9	107.0	
	584.6	1013.9	38.1	11.0	30.5	93°
8	432.8	110.8	10.8	-5.1	22.5	
	434.6	133.0	5.6	32.4	63.6	46°
9	363.9	485.8	39.9	-65.2	80.9	
	369.0	567.9	37.9	36.6	40.9	89°
10	321.1	419.1	15.4	-50.8	96.4	
	321.2	446.8	10.6	6.7	26.7	82°
11	258.1	572.2	8.1	-37.5	114.7	
	263.6	577.2	9.0	2.7	18.9	99°
12	231.5	442.7	19.4	-32.4	96.0	
	247.2	317.9	28.6	-1.4	2.4	93°
13	142.8	789.6	14.1	-59.0	88.6	
	145.6	703.3	5.5	27.3	46.1	86°
Eigenvalues of ε_∞=4.54, 4.72, 4.85						

Table 5.8. Dispersion parameters of $LiNbO_3$ calculated with the unconstrained fit routine. The last column gives the angle between the two members of a degenerate oscillator pair. The eigenvalues of the dielectric background are equivalent to the tensor in diagonal form.

This distinct variation in parameters and angle orientation is the result of the close spectral proximity of intense oscillators. The unconstrained fit routine found an oscillator pair (number 5 in tab. 5.8) with very low intensity, which could not be reproduced by the constrained fit routine. The fit routine found four vibrations parallel to the optical axis as predicted by symmetry analysis, yet according to Barker and Loudon [46] there have to be five modes as $LiNbO_3$ exhibits an additional very intense combination band parallel to the *c*-axis. The calculated oscillator parameters agree well with the values found by Barker and Loudon (cf. tab. 5.10), who also used the Lorentz-

	$\tilde{\nu}_j$ cm^{-1}	S_j cm^{-1}	γ_j cm^{-1}	$\Phi_j{}^\circ$	$\Theta_j{}^\circ$
1	*666.6*	*251.8*	*23.5*	*176.4*	*43.2*
2	*622.7*	*1057.2*	*44.7*	*176.4*	*43.2*
3	*305.4*	*555.4*	*34.3*	*176.4*	*43.2*
4	*256.2*	*825.4*	*10.9*	*176.4*	*43.2*
6	680.9	285.9	40.5	0.5	46.9
7	576.2	974.9	32.6	5.7	47.2
8	431.5	149.9	9.4	0.2	46.8
9	366.1	485.7	21.4	0.2	46.8
10	320.7	490.4	14.8	1.0	46.9
11	262.0	606.7	10.3	2.3	46.9
12	230.6	299.2	38.4	0.4	46.9
13	147.2	745.6	4.0	1.2	46.9

$\varepsilon_{\infty,||}$=4.67, $\varepsilon_{\infty,\perp}$=4.75

Table 5.9. Dispersion parameters of $LiNbO_3$ calculated with the constrained fit routine.

	$\tilde{\nu}_j$ cm^{-1}	S_j cm^{-1}	γ_j cm^{-1}
1	*692*	*49*	*250*
2	*628*	*34*	*1003*
3	*307*	*25*	*123*
	274	*14*	*274*
4	*248*	*21*	*992*
6	670	47	299
7	586	35	1064
8	431	12	182
9	363	33	550
10	322	11	477
11	265	12	621
12	236	12	211
13	152	14	712

$\varepsilon_{\infty,||}$=4.6, $\varepsilon_{\infty,\perp}$=5.0

Table 5.10. Oscillator parameters and dielectric background determined by Barker and Loudon [46].

parameter model and calculated the spectra via Kramers-Kronig relation.

The calculated values for $\varepsilon_{\infty,||}$ agree within calculation errors (± 0.1) with $\varepsilon_{\infty,||}$ given by [46], only the calculated $\varepsilon_{\infty,\perp}$ is too low compared to $\varepsilon_{\infty,\perp}$ from Barker and Loudon in tab. 5.10. This issue is most probably the effect of the one missing mode for the non-degenerate oscillators as the tail of an intense oscillator also influences the fitted value for the dielectric background tensor. The measured reflection spectra with the corresponding fitted spectra of lithium niobate are depicted in fig. 5.5. There seems to be a weak oscillator hidden at $\approx$850 cm^{-1}, marked in the R_s 0 0 0 spectrum, yet this weak vibration could not be resolved by the fit. There also seems to be a band below 100 cm^{-1}, but this is only an effect caused by the polarizers, that have their transmission limit in this spectral region.

Of the 12 spectra 11 spectra look very similar at first sight, which is a result of many intense oscillators with close resonance wavenumbers and, on the other hand, on the orientation of the *c*-axis in the vicinity of a cube face diagonal. The R_p 90 90 45 spectrum is the only spectrum, that looks significantly different from the others, which indicates that the spectrum must be oriented either parallel or normal to the *c*-axis. Accordingly, also spectrum R_s 90 90 45 must be oriented either parallel or normal to the *c*-axis, as it is recorded with orthogonally polarized incident light. The remaining 10 spectra are mixed spectra with varying contribution from non-degenerate and degenerate oscillators.

Band assignment of $LiNbO_3$ is difficult due to the strong oscillators in close spectral proximity. The high intensity of the oscillators cause the overlap of the bands to be more pronounced. Basically, the vibrations can be assigned to the vibrations of the NbO_6 octahedra.

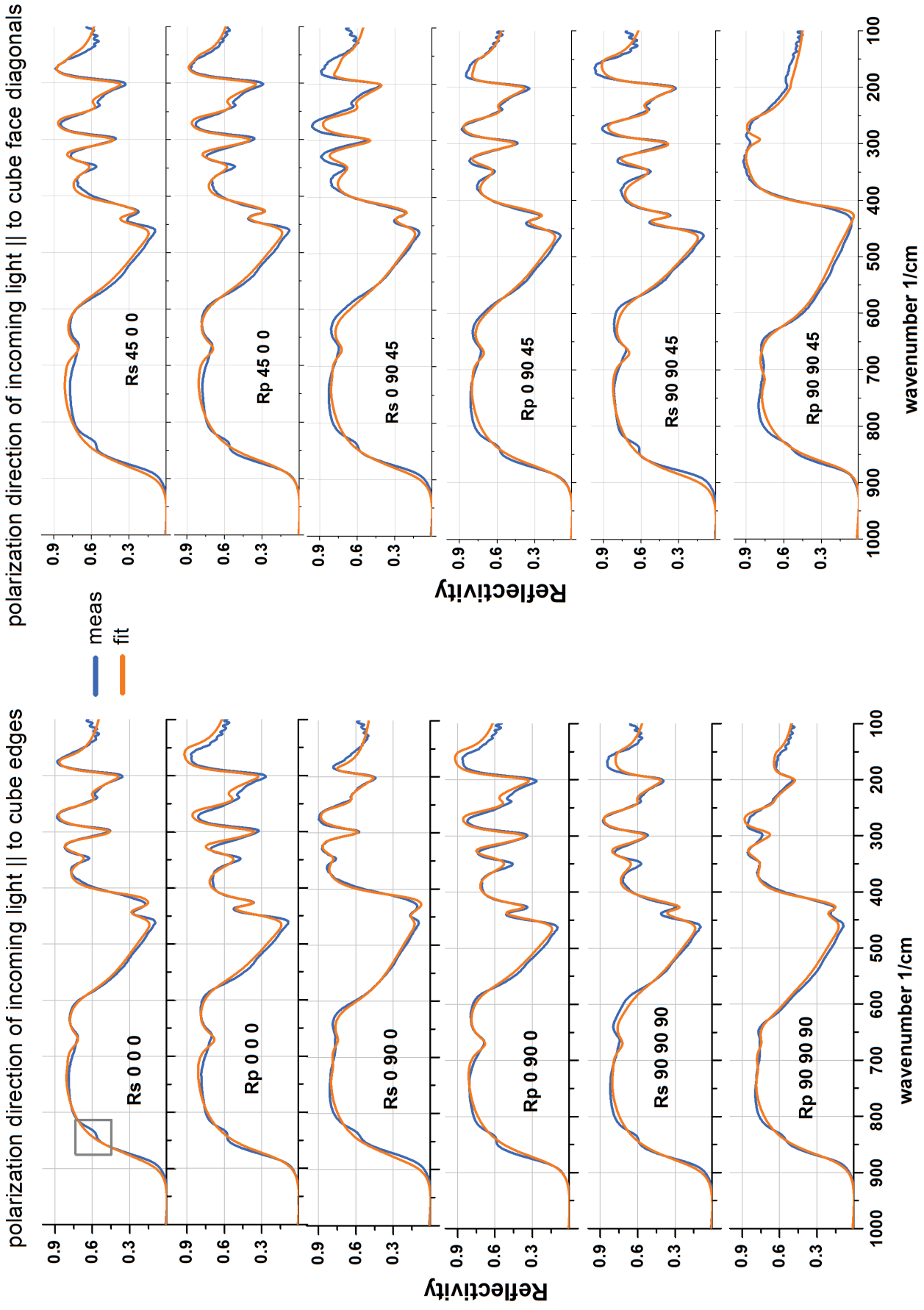

Fig. 5.5. Measured (blue) and calculated (orange) reflection spectra for lithium niobate. Left: polarization direction of the incoming light parallel to the cube edges, right: polarization direction of the incoming light parallel to the cube face diagonals.

A free NbO_6 molecule has 15 internal or 6 normal modes, $\nu_1 - \nu_6$, which are summarized in tab. 5.11 [11]. The asymmetric ν_3 bending vibrations occur at the higher wavenumber spectral region, the ν_5 bending vibrations at the lower wavenumber region [11].

number	symmetry	active in	motion
ν_1	A_{1g}	Raman	symmetric stretching (breathing) vibration
ν_2	E_g	Raman	symmetric stretching vibration of equatorial O-Nb-O bonds
ν_3	F_{1u}	IR	asymmetric O-Nb-O stretching vibration
ν_4	F_{1u}	IR	asymmetric bending vibration of axial O-Nb-O bands
ν_5	F_{2g}	Raman	symmetric in plane O-Nb-O bending vibration (scissoring) of the oxygen ions in equatorial plane
ν_6	F_{2u}	-	asymmetric out-of-plane O-Nb-O bending vibration

Table 5.11. Internal modes of a NbO_6 molecule.

5.5 Verification of oscillator parameters

As quartz, calcite and lithium niobate are colorless and transparent in the visible spectral region, there are no electronic transitions that contribute to the dielectric background tensor and therefore dielectric function for the IR spectral region. With this, the refractive indices can be given by $n_{||/\perp} = \sqrt{\varepsilon_{\infty,||/\perp}}$ and compared to literature values. The results are summarized in tab. 5.12. There is a good agreement between the refractive indices gained by dispersion analysis and the reference values. The values for $n_{||}$ for $LiNbO_3$ differ a little more due to the already discussed reasons.
To verify the results found by dispersion analysis for the constrained fits the so gained oscillator parameters were employed to predict spectra of crystals in principal cuts. The crystal cubes in principal cut were measured the same way as the arbitrarily cut samples according to fig. 2.8, meaning of each of the three mutual orthogonal cube faces four reflection spectra were recorded. Of the 12 spectra measured for a sample in principal cut there exist three different types of spectra that look identical. For six spectra the polarization direction of the incoming light will be oriented perpendicular to the optical axis. For two spectra the polarization direction of the incoming light will be oriented parallel to the optical axis. These spectra are R_p 0 0 0 and R_p 0 90 0 if the initial orientation of the optical axis is parallel to the internal y-axis (cf. fig. 2.9), R_s 0 90 0 and R_s 90 90 90 for the initial orientation of the optical axis parallel to the internal x-axis, or R_s 0 0 0 and R_s 90 90 90 for the initial orientation of the optical axis parallel to the internal z-axis. The remaining four spectra are mixed spectra with

crystal (reference wavenumber	calculated value	reference value
quartz (λ=589.3 nm)	$n_{||} = 1.54$, $n_\perp = 1.57$	$n_{||} = 1.54$, $n_\perp = 1.55$ [67]
calcite (λ=589.3 nm)	$n_{||} = 1.45$, $n_\perp = 1.60$	$n_{||} = 1.48$, $n_\perp = 1.66$ [67]
lithium niobate (λ=1064 μm)	$n_{||} = 2.16$ $n_\perp = 2.18$	$n_{||} = 2.23$ $n_\perp = 2.16$ [68]

Table 5.12. Calculated refractive indices of the uniaxial crystals

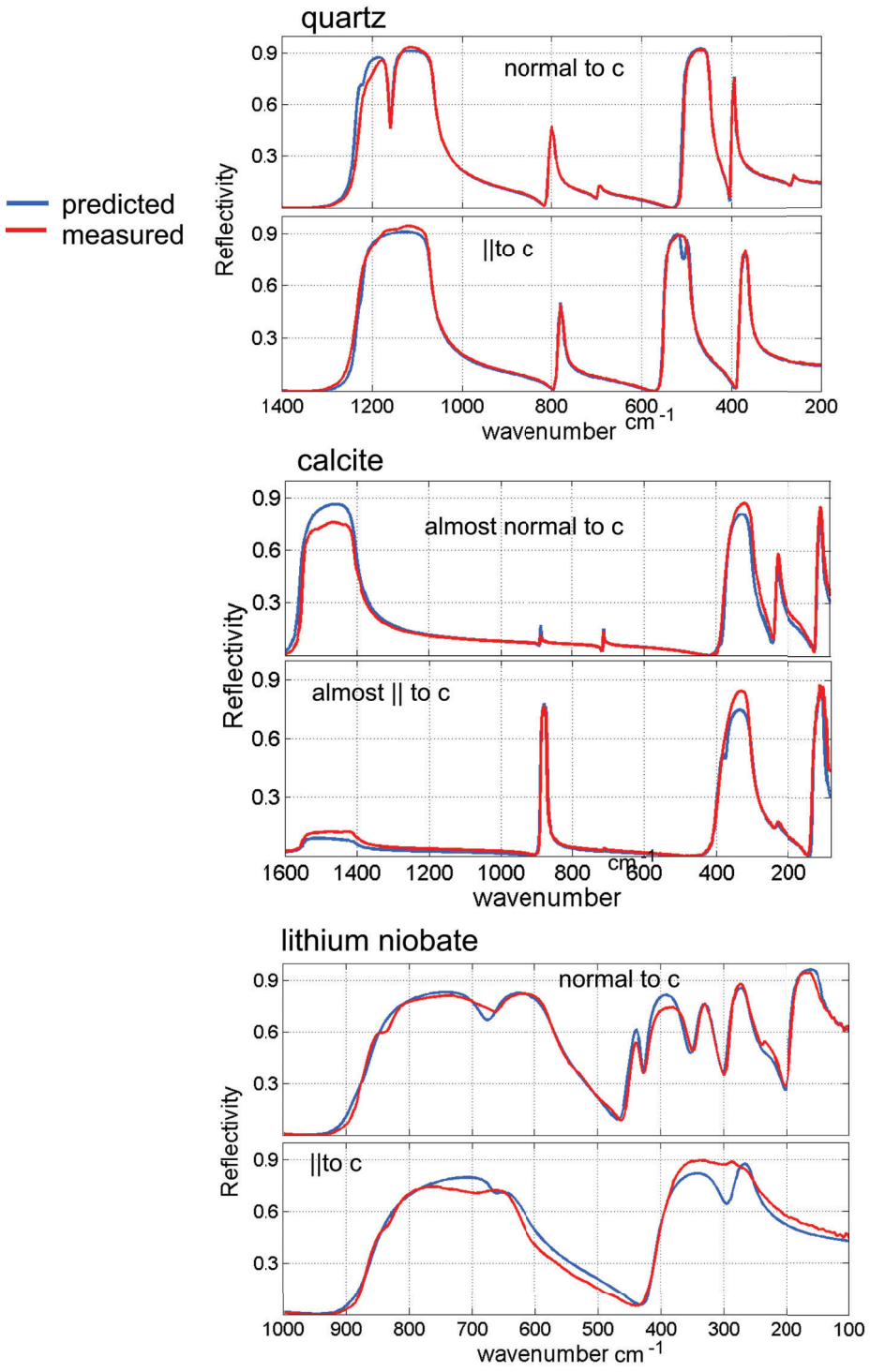

Fig. 5.6. Validation of the oscillator parameters calculated by the constrained fits by predicting spectra of the crystals in principal cut. The orientation angles have to be adapted to respect the different orientation of the optical axis in the arbitrarily and principally cut crystals.

equal contributions from both the oscillators normal and perpendicular to the c-axis. The other way around, if an unknown sample shows this distribution of recorded spectra, the sample is oriented in principal cut with the orientation of the c-axis parallel to the two identical spectra.

For the verification of the oscillator parameters it is sufficient to predict the two spectra recorded with s-polarized incident light and orientation of the optical axis parallel and normal to the polarization direction of the incident light, respectively. Fig. 5.6 shows these two measured spectra (red line) together with the predicted spectra (black line) for each crystal employing the oscillator parameters of the constrained fits given in tables 5.2, 5.6 and 5.9. As the oscillator parameters of the constrained fit refer to a non-principal cut, the orientation angles Φ and Θ were adapted considering the orientation of the optical axis of the principal cuts.

This is simply done by substituting the orientation angles of the non-degenerate oscillators by (Φ, Θ)=(0°, 0°) if the optical axis is oriented parallel to the internal z-axis (or by (Φ, Θ)=(0°, 90°) if the optical axis is parallel to the x-axis or by (Φ, Θ)=(90°, 90°) if the optical axis is parallel to the y-axis) and the angles for degenerate oscillators by (Φ, Θ)=(0°, 90°) for the one member of the degenerate oscillator pair and by (Φ, Θ)=(90°, 90°) for the second member. Accordingly the degenerate oscillator pairs have the angles (Φ, Θ)=(0°, 0°), (90°, 90°) for the orientation of the optical axis parallel to the internal x-axis and (Φ, Θ)=(0°, 0°), (0°, 90°) for the orientation of the optical axis parallel to the internal y-axis.

Overall, there is a satisfying agreement between the measured spectra of the principal cut predicted spectra employing the oscillator parameters gained from the constrained fit routine, even for the lithium niobate crystal in spite of the missing band (cf. tab. 5.9). As the tip of the naturally grown calcite crystal was not polished away exactly normal to the c-axis, but with an angle of 95° to the c-axis, both measured spectra contain contributions of the other oscillator class.

To summarize this chapter, with suitable constraints that reflect the symmetry of uniaxial crystals dispersion analysis can successfully be applied to these crystals. The oscillators parallel and normal to the optical axis, as well as the orientation of the optical axis itself are identified correctly, even if the crystal is built of only slightly distorted high symmetric entities. The calculated dispersion parameters also predict the measured spectra of principally cut samples correctly. If in the uniaxial optimization routine the degeneracy of the oscillators normal to the optical axis is lifted, this leads over to the case of orthorhombic crystals.

Chapter 6

Dispersion analysis of arbitrarily cut orthorhombic crystals

6.1 Adaption of fit routine to orthorhombic crystals

For a crystal in principal cut which has the crystal edges parallel to the crystallographic axes, the principal axes of the the dielectric tensor function are also aligned parallel to the cube edges and the dielectric tensor function is then of diagonal form. If the crystal is in *general* cut, there are no non-zero elements anymore and the dielectric function takes on the familiar form of the generalized dielectric tensor function as is given for the triclinic crystals (cf. chapter 2.4). The orientation of the oscillators must fulfill certain constraints referring to the symmetry of orthorhombic crystals, namely the parallel alignment of an oscillator to one of the three crystal axes. Translated to the fit routine there are three classes of oscillators with each class being orthogonal to the other two classes. The oscillators within a certain class are oriented parallel to each other. Fig. 6.1 shows the arrangement of the three oscillator classes in a crystal with arbitrary

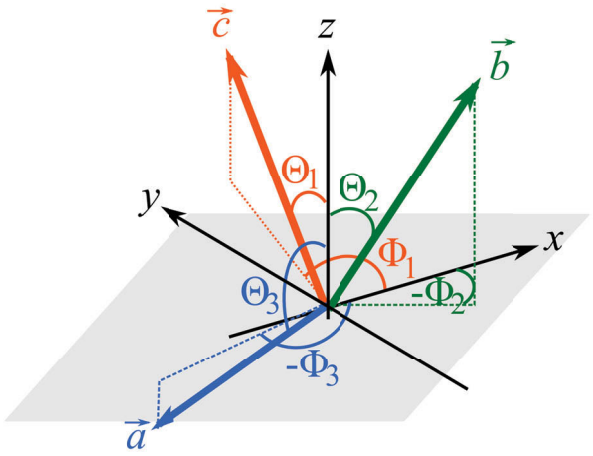

Fig. 6.1. Arrangement of transition moments in an arbitrarily cut orthorhombic crystal represented by the vectors $\vec{a}, \vec{b}$ and $\vec{c}$. The transition moments are aligned parallel to the crystal and dielectric axes.

cut. The orientations of the vectors $\vec{a}, \vec{b}$ and $\vec{c}$ represent the transition moments and therefore the orientation of the crystal axes a, b, c. To fulfill the orthogonality condition the dot product of the three vectors must vanish:

$$\frac{\vec{a}\cdot\vec{b}}{|\vec{a}|\cdot|\vec{b}|} \stackrel{!}{=} 0, \qquad \frac{\vec{a}\cdot\vec{c}}{|\vec{a}|\cdot|\vec{c}|} \stackrel{!}{=} 0, \qquad \frac{\vec{c}\cdot\vec{b}}{|\vec{c}|\cdot|\vec{b}|} \stackrel{!}{=} 0. \tag{6.1}$$

The solutions of equation 6.1 leads to expressions for the angles Φ_3, Θ_2 and Θ_3 as function of Φ_1, Φ_2, and Θ_1.

$$\begin{aligned} \Theta_2 &= \arctan\left(\frac{-1}{\tan\Theta_1\cdot\cos(\Phi_2-\Phi_1)}\right) \\ \Phi_3 &= \arctan\left(\frac{\tan\Theta_1\cdot\cos\Phi_1-\tan\Theta_2\cdot\cos\Phi_2}{\tan\Theta_2\cdot\sin\Phi_2-\tan\Theta_1\cdot\sin\Phi_1}\right) \\ \Theta_3 &= \arctan\left(\frac{-1}{\tan\Theta_1\cdot\cos(\Phi_3-\Phi_1)}\right) \end{aligned} \tag{6.2}$$

This constraint reduces the number of orientation angles that have to be fitted to the three angles Φ_1, Θ_1 and Φ_2 as the other three orientation angles are fixed by the orthogonality condition in equation 6.2.
During the fitting procedure based on the 12 spectra it turned out that for orthorhombic crystals the orientation of the crystal axes could not be unambiguously determined. Especially the spectra of the neodymium gallate sample could even be fitted with a very good agreement between measured and calculated spectra, but with completely wrong orientation angles for the oscillators. This is mainly due to intense and broad vibrations of only slightly distorted high symmetric structures with the resonance frequency of the transition moments in close spectral proximity. Furthermore, in contrary to the uniaxial crystals, whose 12 spectra are a combination of only two independent spectra, for the orthorhombic crystals the fit routine has to separate three independent spectra. For topaz the phenomenon of several close and intense oscillators is not that distinct compared to neodymium gallate, but also for topaz a suitable fit can be performed with wrong orientation angles. Obviously, to find the correct orientation the 12 spectra measured with only one polarizer are not sufficient.
Therefore, to support the fit routine additional cross polarization spectra were recorded by inserting an analyzer into the beam line behind the sample holder with crossed transmission direction compared to the polarizer. If the transmission direction of the polarizer is set to s-polarization, the transmission direction of the analyzer is set to p-polarization and vice versa. With this setup 12 cross polarization spectra were recorded in the same way that is given in fig. 2.9. The advantage of the cross polarization spectra is that they very reliably reveal wether a spectrum is recorded with polarization direction of the incoming light parallel or normal to a crystal axis. This

is the case if the signal of the corresponding spectrum is reduced to noise because the cross-polarization terms represented by the off-diagonal elements of the dielectric tensor function are zero for the principal orientation. The disadvantage is the usually low intensity and therefore an increased signal-to-noise ratio. In fig. 6.2 the crystal is oriented in a way that one axis is aligned parallel to a cube face diagonal and the other two crystal axes point toward the left and right cube edges, but with an angle β_2 and β_3 between the axes and the surface.

The polarization direction of a s-polarized wave is normal to the vibration direction of oscillators 2 and 3, so only oscillator 1 gets excited and reacts as a dipole that emits a wave with the same polarization state as the incoming wave (fig. 6.2 left). Therefore, the analyzer that is rotated to p-transmittance blocks the signal of oscillator 1 and the cross polarization spectrum is a zero line. A p-polarized incoming wave will excite oscillators 2 and 3 with a component z depending on the angle of incidence α and the angle of the oscillator β to the crystal face, $z \propto \sin(90°-\alpha-\beta)$. As the polarization state of the reflected wave will also be in the plane of incidence, no signal passes the analyzer in s-position. For all other arbitrary orientation of the dielectric axes to the polarization direction of the incoming light the reflected light wave is not polarized purely normal or parallel to the plane of incidence and contains a polarization component parallel to the transmission direction of the analyzer. The component is at maximum if the oscillator is oriented parallel or normal to the plane of incidence and 45° to the transmission direction of the polarizer (then the oscillator is oriented 45° to the transmission direction of the analyzer as well). The intensity of the residual signal will be half of the signal of the original band (Malus' law, [69]) for ideal polarizers, but as some light is lost in the polarizer, the residual signal will be somewhat lower.

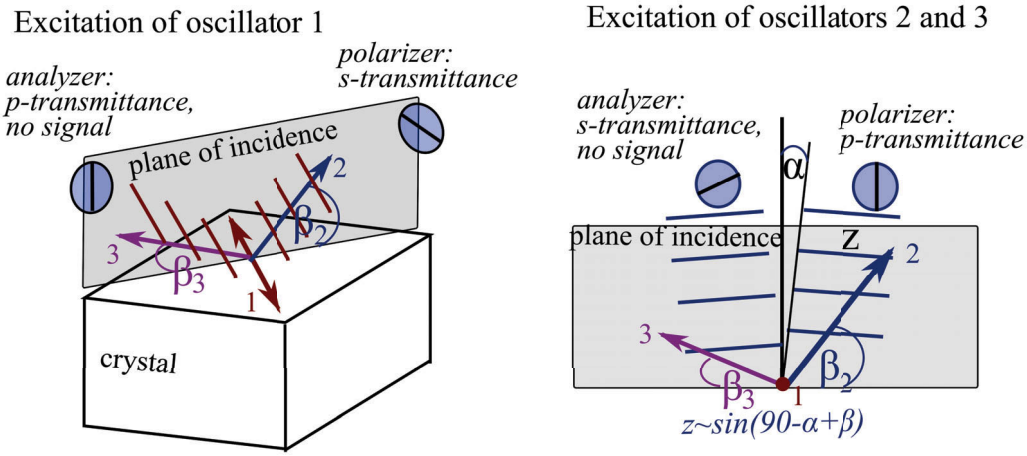

Fig. 6.2. Measurements with crossed polarizers for an orthorhombic crystal. If the spectrum is recorded with polarization direction of the incident light parallel or normal to a crystal axis no signal will pass the analyzer with contrary transmission state than the polarizer. Left: S-polarized incident light excites oscillator 1. Right: P-polarized incident light excites oscillators 2 and 3

cross polarization spectrum	orientation angles (Φ, Θ)	meaning
$R_{sp/ps}$ 0 0 0, $R_{sp/ps}$ 0 90 0, $R_{sp/ps}$ 90 90 90	0°,0°/ 90°,90°/ 0°,90°	principal cut
$R_{sp/ps}$ 0 0 0, $R_{sp/ps}$ 90 90 90, $R_{sp/ps}$ 0 90 45	0°,90°/ 90°,45°/ 90°,135°	rotation of principal cut 45° around x
$R_{sp/ps}$ 0 90 0, $R_{sp/ps}$ 90 90 90, $R_{sp/ps}$ 45 0 0	0°,0°/ 45°,90°/ 135°,90°	rotation of principal cut 45° around z
$R_{sp/ps}$ 0 0 0, $R_{sp/ps}$ 0 90 0, $R_{sp/ps}$ 90 90 45	90°,90°/ 180°,45°/ 0°,45°	rotation of principal cut 45° around y
$R_{sp/ps}$ 0 0 0, $R_{sp/ps}$ 0 90 0	90°,90°/ 0°,θ_1 / 180°,θ_2	rotation of principal cut $\neq$45° around y
$R_{sp/ps}$ 0 0 0, $R_{sp/ps}$ 90 90 90	0°,90°/ 90°,θ_1 / -90°,θ_2	rotation of principal cut $\neq$45° around x
$R_{sp/ps}$ 0 90 0, $R_{sp/ps}$ 90 90 90	0°,0°/ ϕ_1,90°/ ϕ_2,90°	rotation of principal cut $\neq$45° around z
$R_{sp/ps}$ 0 0 0	90°,90°/ 0°,θ_1 / 180°,θ_2 or 0°,90°/ 90°,θ_1 / -90°,θ_2	no special meanings
$R_{sp/ps}$ 0 90 0	90°,90°/ 0°,θ_1 / 180°,θ_2 or 0°,0°/ ϕ_1,90°/ ϕ_2,90°	
$R_{sp/ps}$ 90 90 90	0°,90°/ 90°,θ_1 / -90°,θ_2 or 0°,0°/ ϕ_1,90°/ ϕ_2,90°	
$R_{sp/ps}$ 45 0 0	45°,90°/ -45°,θ_1 / 135°,θ_2 or -45°,90°/ 45°,θ_1 / -135°,θ_2	
$R_{sp/ps}$ 0 90 45	one angle either 90°,45° or -90°,45°	
$R_{sp/ps}$ 90 90 45	one angle either 0°,45° or 0°,-45°	

Table 6.1. Information about orientation angles gained from cross polarization spectra of orthorhombic crystals that show a zero line. The index $R_{sp/ps}$0 0 0 is an abbreviation for "R_{sp}0 0 0 and R_{ps}0 0 0", and so on.

Depending on the number of the zero line cross polarization spectra orientation angles can either be constricted to few possibilities or be determined without performing further dispersion analysis. Since many crystals are only cleavable or can be grown in certain directions the information that can be gained from the zero line cross polarization spectra are summarized in tab. 6.1. If the orientation angles are not directly revealed by the cross polarization spectra, they have to be included into the fitting routine. This means, that both spectra sets, the 12 spectra recorded with the sole polarizer and the 12 cross polarization spectra are fitted simultaneously. As the fit routine calculates both spectra types anyway, this means no additional calculation time. Usually, the cross polarization spectra are of low intensity, so the fitting process starts with manually modeling the dielectric background and the one polarizer spectra without considering the cross polarization spectra, is described in chapter 2.8. To push the fit into the right direction, the orientation angles are fitted at first, including the orthogonality condition ab initio. For this, the error value needs to be weighted: the cross polarization spectra have to contribute almost completely to the error value while the one polarizer spectra contribute only minimally to the error value. This is realized by varying the power of the error values (cf. chapter 2.8). Fitting artificial spectra of an orthorhombic crystal showed that best results were achieved by leaving the errors of the cross polarization spectra squared and changing the power of the error

of the one polarizer spectra to 4. Then the oscillator strengths, resonance wavenumber and orientation angles are fitted iteratively in the usual way with the sole and cross polarization spectra contributing equally to the error value. To yield good results it is essential that the cross polarization spectra have to be measured with good precision concerning the alignment of the sample in the holder and with a sufficient number of scans that reduces the noise to a level that the residual spectrum becomes clearly visible.

For an arbitrarily cut orthorhombic crystal generally all elements of the dielectric background are different from zero. To yield the principal elements of the dielectric background for an orthorhombic crystal, there are two possibilities: Either the eigenvalues of the dielectric background tensor are calculated, which denote the values of the dielectric background parallel to the crystal axes, or the background tensor is sandwiched between a rotation matrix $\mathbf{M}_{rot}$ and its inverse. With the matrix $\mathbf{M}_{rot}$ the dielectric tensor of the arbitrarily cut crystal into principal form. The matrix $\mathbf{M}_{rot}$ is the same as for uniaxial crystals in chapter 5

$$\mathbf{M}_{rot} = \begin{pmatrix} \cos\Phi & -\sin\Phi\cos\Theta & \sin\Theta\sin\Phi \\ \sin\Phi & \cos\Theta\cos\Phi & -\sin\Theta\cos\Phi \\ 0 & \sin\Theta & \cos\Theta \end{pmatrix}. \tag{6.3}$$

Note that for orthorhombic crystals no predominant direction exists in contrast to uniaxial crystals. Therefore, each of the three orientation angle pairs are equivalent and can be inserted for Φ (rotation around internal z-axis) and Θ (rotation around internal x-axis), although they result in a different orientation of the dielectric background ellipsoid. Each of the three orientation angles result in another arrangement of the values $\varepsilon_{xx}, \varepsilon_{yy}$ and ε_{zz}. The element ε_{xx} always refers to the oscillators aligned parallel to the internal x-axis, the element ε_{yy} refers to oscillator oriented parallel to the y-axis and the element ε_{zz} refers to oscillators aligned parallel to the z-axis. If, for example, the matrix $\mathbf{M}_{rot}$ rotates the dielectric background tensor in a way that ε_{xx} does not correspond to the oscillators oriented parallel to the x-axis, another of the three orientation angle pairs must be inserted in $\mathbf{M}_{rot}$.

6.2 Results of dispersion analysis for neodymium gallate

The spectra measured with crossed polarizers for neodymium gallate are shown in fig. 6.3. The reflectivity of the cross polarization spectra is roughly 5-20% of the one polarizer spectra. Only the spectra $R_{sp/ps}$ 45 0 0 are a zero line which indicates that one of the crystal axes must be oriented parallel or perpendicular to a diagonal of cube face 1. In fig. 6.3 there is a certain spectral range of the zero line cross polarization spectra that drop below the zero line, which is due to a systematic error of the spec-

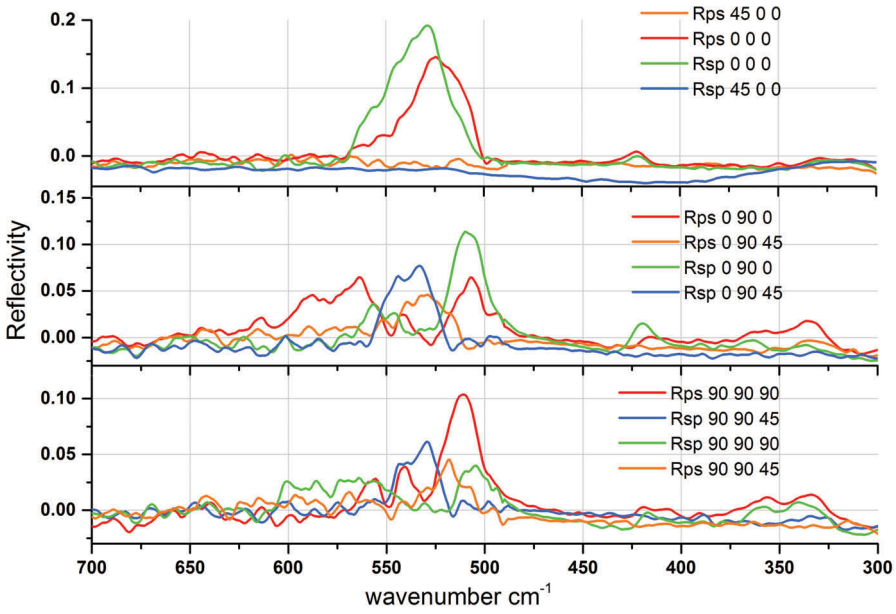

Fig. 6.3. Measured cross polarization spectra of neodymium gallate.

trometer. In combination with the orthogonality condition only the two possible angle combinations (Φ, Θ)=(45°, 90°), (-45°, θ_1), (135°, θ_2) and (Φ, Θ)=(-45°, 90°), (45°, θ_1), (-135°, θ_2) are left (cf. tab. 6.1).

This leaves only the two angles θ_1 and θ_2 left to be optimized. Now these conditions for the orientation angles are sufficient to continue with the fit without further consideration of the cross polarization spectra. The calculated oscillator parameters are given in tab. 6.2. The surfaces of the $NdGaO_3$ cube showed very different qualities, although all faces had been polished very carefully. Therefore the spectra had to be fitted with a correction factor as it was the case for the $K_2Cr_2O_7$ crystal (chapter 4.2). The correction factor for each spectrum is given in tab. 6.4. Although one angle pair is fixed to (Φ, Θ)=(135°, 45°) the angles were allowed to vary in the fit for compensation of misalignment and cutting errors.

Tab. 6.3 lists the calculated oscillator parameters of a neodymium gallate sample in principal cut. As these spectra are evaluated independently from each other with only three unknowns per oscillator, these values can serve as reference values for the oscillator parameters found for the arbitrarily cut crystal. Corresponding oscillators in both tables are numerated with the same number. The oscillator parameters for the arbitrarily and principally cut $NdGaO_3$ cube agree well with each other, only the strength of oscillator 5 differs by more than $100\,cm^{-1}$. The fit of the principally cut cube produced an additional oscillator parallel to the b-axis that did not occur in the fit for the arbitrarily cut sample. Also, the fitted resonance wavenumbers agree with the wavenumbers measured and calculated by Suda et al [70].

	$\tilde{\nu}_j$ cm^{-1}	S_j cm^{-1}	γ_j cm^{-1}	$\Phi_j{}^\circ$	$\Theta_j{}^\circ$
1	612.9	237.9	24.4	133.8	43.7
2	372.9	615.9	20.5	133.8	43.7
3	350.9	221.7	9.9	133.8	43.7
4	302.2	390.6	22.9	133.8	43.7
5	276.9	491.7	7.5	133.8	43.7
6	253.3	304.4	6.8	133.8	43.7
7	173.3	376.9	5.7	133.8	43.7
8	581.2	261.4	38.1	-40.3	46.4
9	541.1	192.4	9.4	-40.3	46.4
10	429.5	195.3	11.0	-40.3	46.4
11	306.7	713.0	26.8	-40.3	46.4
12	279.8	486.3	8.5	-40.3	46.4
13	239.2	280.3	8.5	-40.3	46.4
14	175.8	334.2	3.8	-40.3	46.4
15	118.2	97.6	8.2	-40.3	46.4
16	594.3	299.7	25.4	46.8	92.9
17	343.6	659.0	20.8	46.8	92.9
18	290.5	375.3	10.6	46.8	92.9
19	271.1	494.6	4.5	46.8	92.9
20	168.5	435.5	10.3	46.8	92.9

Eigenvalues of ε_∞=4.08, 4.21, 4.01

Table 6.2. Calculated oscillator parameters for the cube shaped arbitrarily cut neodymium gallate sample.

		$\tilde{\nu}_j$ cm^{-1}	S_j cm^{-1}	γ_j cm^{-1}
||a	1	609.6	227.1	24.7
	2	366.9	585.0	16.8
	3	347.2	212.8	10.0
	4	303.1	383.6	20.8
	5	275.4	580.0	7.4
	6	252.3	354.2	8.1
	7	172.9	412.5	5.4
||b	8	577.2	279.2	38.5
	9	540.4	172.0	6.2
	10	428.9	197.7	11.2
		320.0	407.3	15.3
	11	296.3	638.4	16.1
	12	278.3	459.5	5.4
	13	239.0	282.7	9.0
	14	178.7	356.0	3.3
	15	117.5	99.2	8.8
||c	16	596.3	295.7	23.6
	17	346.3	664.5	15.7
	18	289.0	368.2	12.2
	19	272.1	472.9	4.1
	20	167.6	472.1	11.7

$\varepsilon_{\infty,a}$=4.28, $\varepsilon_{\infty,b}$=4.24, $\varepsilon_{\infty,c}$=4.36

Table 6.3. Calculated oscillator parameters for a cube shaped neodymium gallate sample in principal cut.

The oscillator parameters of tables 6.2 and 6.3 also reveal that most of the vibrations seem to originate from threefold degenerate vibrations, e.g. oscillators (1,8,16), (2,11,17) or (7,14,20). As the reflection spectra of neodymium gallate are characterized mainly by strong and broad bands with resonance wavenumbers in close proximity (similar to the spectra of lithium niobate, cf. chapter 5.4), the bands can only be tentatively assigned to the corresponding molecule vibrations. The structure of $NdGaO_3$ is built of GaO_6 octahedra in an only minimally distorted form compared to the free octahedral molecule [48]. The modes of a MO_6 moiety are already given in tab. 5.11. Usually, the ν_3 asymmetric stretching vibration occurs at the higher wavenumber region [11], so they are most probably assigned to oscillators 1, 8 and 16.
The 12 measured reflection spectra employed to perform dispersion analysis together with the calculated spectra are shown in fig. 6.4. The overall agreement between fitted and measured spectra is very good.

spectrum	Rs 0 0 0	Rs 0 90 0	Rs 90 90 90	Rs 45 0 0	Rs 0 90 45	Rs 90 90 45
f_{corr}	1.02	1.03	0.92	1.03	1.08	0.91
spectrum	Rp 0 0 0	Rp 0 90 0	Rp 90 90 90	Rp 45 0 0	Rp 0 90 45	Rp 90 9045
f_{corr}	1.06	1.02	0.93	1.10	1.06	0.89

Table 6.4. Correction factors f_{corr} for the optimized spectra of $NdGaO_3$ to support the fitting process

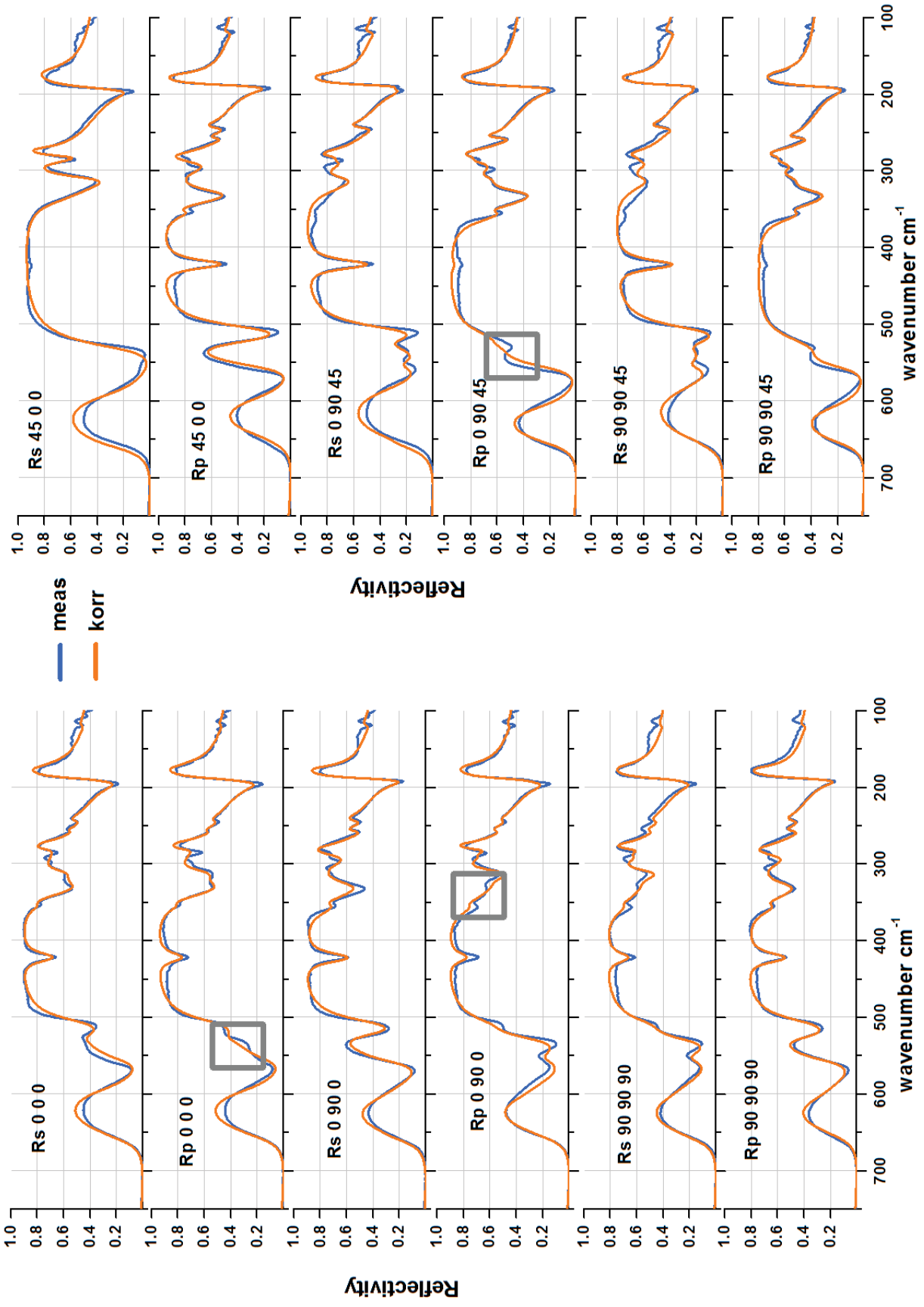

Fig. 6.4. Measured (blue) and calculated (orange) reflection spectra for neodymium gallate. Left: polarization direction of the incoming light parallel to the cube edges, right: polarization direction of the incoming light parallel to the cube face diagonals.

The spectral features at ≈540 cm^{-1} and ≈350 cm^{-1} (marked in Fig. 6.4) are not satisfactorily caught for every measured spectrum. In these spectral regions a weak oscillator occurs only as shoulder of a very intense oscillator.
Fig. 6.5 shows the three measured independent spectra (red) of a principal cut and the predicted spectra (black) employing the oscillator parameters given in tab. 6.2. To respect the different orientations of crystal (or equivalently dielectric) axes the orientation angles of the first, second and third block of tab. 6.2 were substituted by $(\Phi, \Theta)=(0°, 0°)$, $(90°, 90°)$ and $(0°, 90°)$, respectively. With this substitution the dielectric axes of the arbitrarily cut crystal cube are aligned parallel to the axes of the principal cut. The measured and predicted spectra show a good agreement, only the band at 300 cm^{-1} for the oscillators aligned parallel to the b-axis was not reproduced. For comparison in the figure also the fitted spectra (green) of the principally cut cube are shown, employing the oscillator parameters of tab. 6.3. In the principal cut the band at 300 cm^{-1} of the oscillators parallel to b is easily visible. Obviously it can happen that a crystal is cut in a way that conceals a band, although the measured spectra are reproduced very well by a fit.
There remains the question if the orientation can also be correctly found if the crystal axes do not take one of the special directions of tab. 6.1. Since no such crystal cut was at disposal, the dispersion parameters of tab. 6.2 (without the weak oscillator

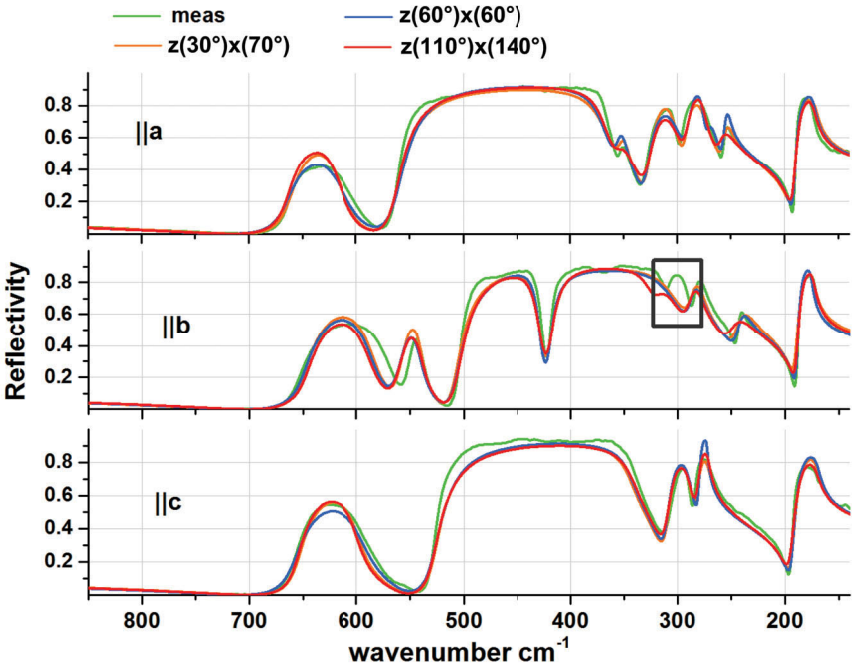

Fig. 6.5. Red: The three measured independent spectra of a neodymium gallate sample in principal cut. Black: forward calculated spectra with oscillator parameters found for the arbitrarily cut crystal. Green: Fitted spectra of the principal cut employing the dispersion parameters of tab. 6.3.

employed rotation	axis	resulting Φ, Θ	fitted Φ, Θ	# osc.	ε_∞
60° around x followed by	|| a	150°,120°	149.7°,120.1°	8	4.02
60° around z	|| b	-30°,-30°	-29.9°,-30.1°	7	4.08
	|| c	60°,90°	62.9°,89.2°	5	4.18
70° around x followed by	|| a	120°,110°	119.7°,109.9°	7	4.06
30° around z	|| b	-60°,-20°	-58.9°,-19.9°	7	4.09
	|| c	30°,90°	29.8°,89.5°	5	4.24
140° around x followed	|| a	20°,-40°	19.9°,-39.9°	7	4.02
by 110° around z	|| b	20°,50°	19.8°,50.0°	8	4.05
	|| c	110°,90°	109.7°,90.0°	5	4.18

Table 6.5. First column: applied rotation to the fitted spectra of the arbitrarily cut $NdGaO_3$ cube brought into principal orientation. Second and third columns: The oscillators aligned parallel to the axis of column 2 have after the rotation the orientation of column 3. Fourth column: fitted orientation angles. Fifth and last column: Number of oscillators found by the fit, and fitted dielectric background.

14 as it is located in the spectral limit of the FIR-polarizer) were at first brought into principal orientation and then rotated by the rotation matrix of equation 6.3 in a way that all cross polarization spectra are different from zero. The resulting spectra were then treated and fitted like an unknown set of spectra using no knowledge about the orientation or other oscillator parameters. The employed rotation angles, the the orientation angles resulting from that rotation, the numbers of oscillators found by the fit routine (#osc.) as well as the dielectric background are given in tab. 6.5. The orientation angles have been captured very well with the support of the cross polarization spectra, also the dielectric background has been well reproduced.

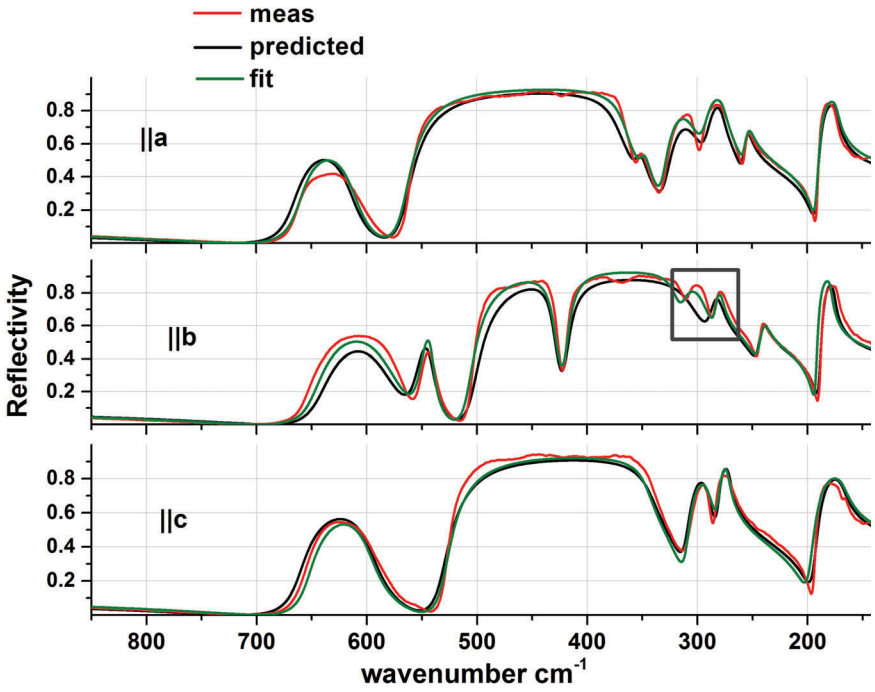

Fig. 6.6. Comparison of calculated spectra of different orientations of the neodymium gallate cube with the measured spectra of a principally cut sample.

The number of oscillators varies due to weaker oscillators too close to intense oscillators to be resolved by the fit routine. For comparison the three fitted different spectra sets were brought into principal orientation and plotted together with the measured spectra of the principally cut sample in fig. 6.6. The notation "z(30°)x(70°)" is an abbreviation for a rotation of 70° around the internal x-axis followed by a rotation of 30° around the internal z-axis. The same holds for the abbreviations "z(60°)x(60°)" and "z(110°)x(140°)". The calculated spectra of the different orientations were brought into principal orientation by substituting their orientation angles by (Φ, Θ)=(0°,0°) for the oscillators parallel to a, (90°,90°) for the oscillators parallel to b and (0°,90°) for the oscillators parallel to c. The fitted simulated spectra all look very similar, except for the spectral region at 280-320 cm^{-1} in the orientation parallel to the b-axis.
Most resonance wavenumbers of the oscillators were found within $\approx \pm 3\,\mathrm{cm}^{-1}$, most oscillator strengths within $\approx \pm 8\,\mathrm{cm}^{-1}$ and most damping constants within $\approx \pm 3\,\mathrm{cm}^{-1}$, but the comparison of the results of only three different orientations are a little too less to give a sensible standard deviation.

6.3 Results of dispersion analysis for topaz

Like for neodymium gallate, the fit routine to perform dispersion analysis of topaz was also supplemented by cross polarization spectra, which are shown in fig. 6.7. Six of the measured cross polarization spectra, $R_{sp/ps}$ 45 0 0, $R_{sp/ps}$ 0 90 0 and $R_{sp/ps}$ 90 90 90, show no signal which leaves only one possible angle combination given in

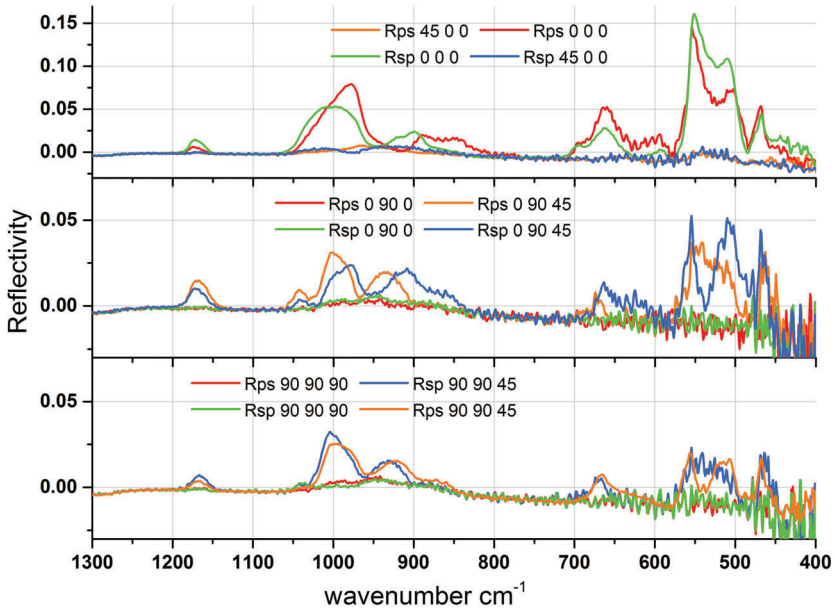

Fig. 6.7. Cross polarization spectra of the naturally grown topaz crystal. From the spectra the orientation angles of the crystal axes can directly be derived.

		$\tilde{\nu}_j$ cm^{-1}	S_j cm^{-1}	γ_j cm^{-1}	${\Phi_j}^\circ$	${\Theta_j}^\circ$
|| a_1	1	1156.1	145.3	15.0	133.2	89.6
	2	923.3	261.2	34.3	133.2	89.6
	3	851.4	589.1	23.0	133.2	89.6
	4	607.1	443.0	24.1	133.2	89.6
	6	565.7	179.6	19.0	133.2	89.6
	7	450.4	422.5	14.2	133.2	89.6
	8	391.2	377.3	17.9	133.2	89.6
	9	341.3	95.7	15.1	133.2	89.6
	10	312.7	148.6	7.0	133.2	89.6
	11	270.5	126.9	4.5	133.2	89.6
|| a_2	12	3640.0	150.0	15.0	43.2	-89.6
	13	1160.1	218.4	16.3	43.2	-89.6
	14	995.6	188.4	25.6	43.2	-89.6
	15	901.9	222.3	25.9	43.2	-89.6
	16	878.2	607.8	29.8	43.2	-89.6
	17	616.1	327.5	29.4	43.2	-89.6
	18	511.9	359.0	7.7	43.2	-89.6
	19	481.4	144.7	10.0	43.2	-89.6
	20	439.1	466.5	8.5	43.2	-89.6
	21	382.3	137.8	14.0	43.2	-89.6
|| c	22	856.0	653.2	37.1	-0.3	0.6
	23	610.8	402.9	21.8	-0.3	0.6
	24	555.1	205.8	13.5	-0.3	0.6
	25	472.9	557.0	28.4	-0.3	0.6
	26	371.9	137.3	12.5	-0.3	0.6
	27	333.4	159.0	6.5	-0.3	0.6
	28	289.8	142.7	7.6	-0.3	0.6
	29	3640.0	180.0	15.0	-0.3	0.6

Eigenvalues of ε_∞=2.27, 2.64, 2.48

Table 6.6. Calculated oscillator parameters for the naturally grown topaz sample.

tab. 6.1, namely (Φ, Θ)=(0°, 0°), (45°, 90°) (=(45°, -90°)), (135°, 90°). In tab. 6.6 the calculated oscillator parameters for the naturally grown topaz sample are listed. As it was unclear which of the crystal axes normal to c is the a- or b-axis they are labeled a_1 and a_2. The angles were not fixed to the angles derived by the cross polarization spectra but allowed to vary a little for correction of misalignment errors. The measured and with these oscillator parameters modeled spectra are shown in fig. 6.8. The measured and calculated spectra show a satisfying agreement for most of the spectral range. In the higher wavenumber region $\geq 2000\,\mathrm{cm}^{-1}$ the fitted dielectric background becomes too high compared to the measured signal, although the fitted and measured dielectric background agree for the spectral range with wavenumbers below $2000\,\mathrm{cm}^{-1}$. This is an effect depending on surface quality. Not every cube face could be polished with equal optical quality. The topaz crystal was transparent, yet contained several inclusions. In the case of not perfectly polished surfaces the registered intensity dropped non-proportionally, which lead to a too low signal for the dielectric background of the corresponding spectra. Therefore the oscillator parameters for the O-H stretching vibration at $3640\,\mathrm{cm}^{-1}$ may be only tentatively calculated.

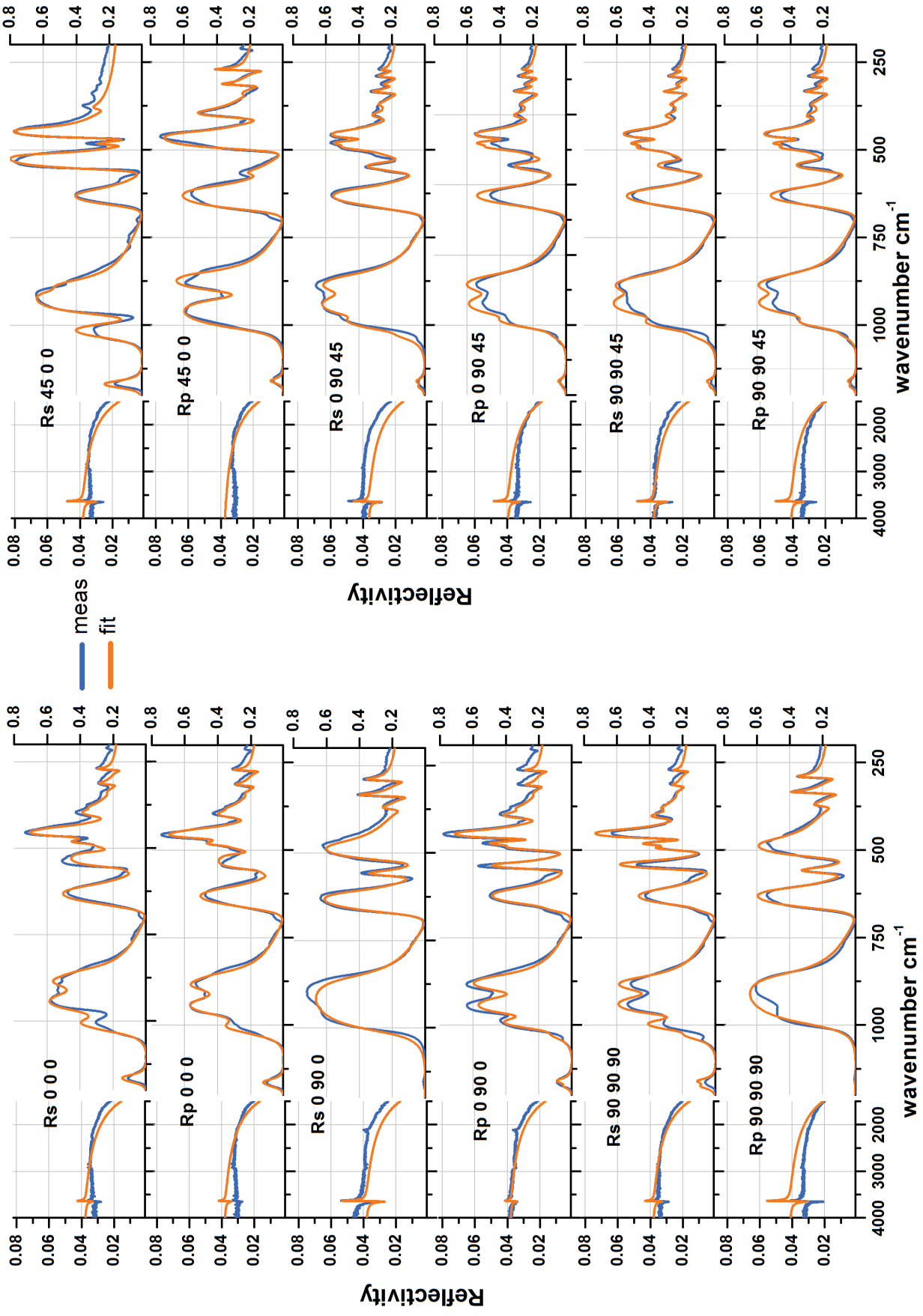

Fig. 6.8. Measured (blue) and calculated (orange) reflection spectra for topaz. Left: polarization direction of the incoming light parallel to the cube edges, right: polarization direction of the incoming light parallel to the cube face diagonals.

The spectral region between 1000 and 750 cm^{-1} contains several strong and close oscillators, which is the usual problem that makes it very difficult for the fit to catch all spectral features.

In contrary to the spectra for the neodymium gallate sample, the bands in the spectra of the topaz crystal are more differentiated, which allows a better band assignment. Similar to quartz, the structure of topaz consists of SiO_4 tetrahedra, that are only slightly distorted [71]. Consequently, the SiO_4 vibrations should be located roughly at the same spectral region as for quartz, so oscillators 3, 16 and 22 can be assigned to the ν_3 asymmetric stretching vibration of the SiO_4 tetrahedra [49]. The ν_4 asymmetric bending vibration occurs in the spectral region from 500 to 400 cm^{-1} and is most probably represented by oscillators 7, 18 and 25, as the vibration represented by these oscillators also has the highest intensity in this spectral region. The bands at 3640 cm^{-1} indicate that the topaz crystal contains a certain amount of Si-OH, which also cause the vibrations at 1160 cm^{-1} (oscillators 1+13) [49]. In the lower wavenumber region band assignment becomes difficult as this is also the spectral region of the lattice vibrations.

As it was not allowed to cut the borrowed topaz crystal, we could not produce a topaz sample in principal cut. Therefore, we brought the dispersion parameters of tab. 6.6 into principal orientation and compared the resulting spectra with the spectra of a principally cut topaz crystal recorded by Adams et al [71]. The spectra are shown in fig. 6.9.

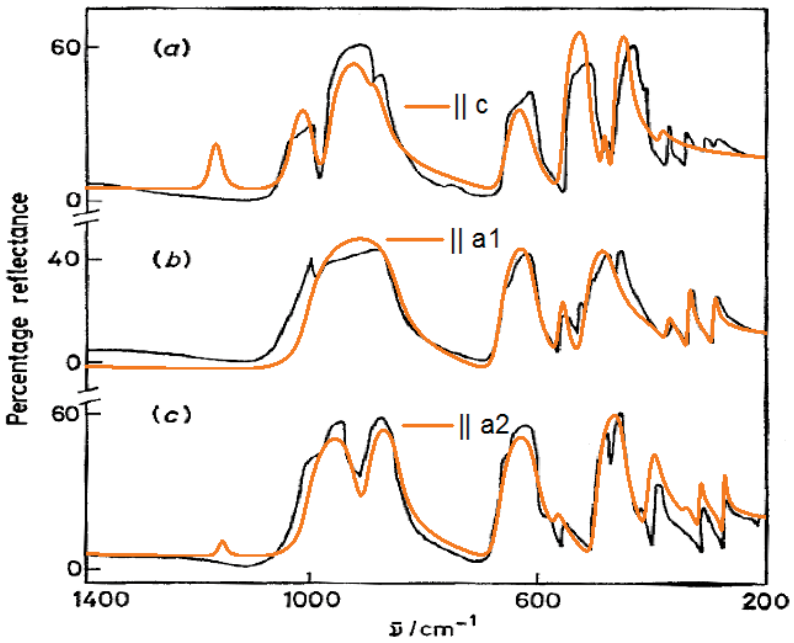

Fig. 6.9. Black graph: spectra of a topaz crystal in principal cut measured by [71]. Orange spectra: Forward calculated spectra of a principal cut using the dispersion parameters given in tab. 6.6, rotated into principal orientation.

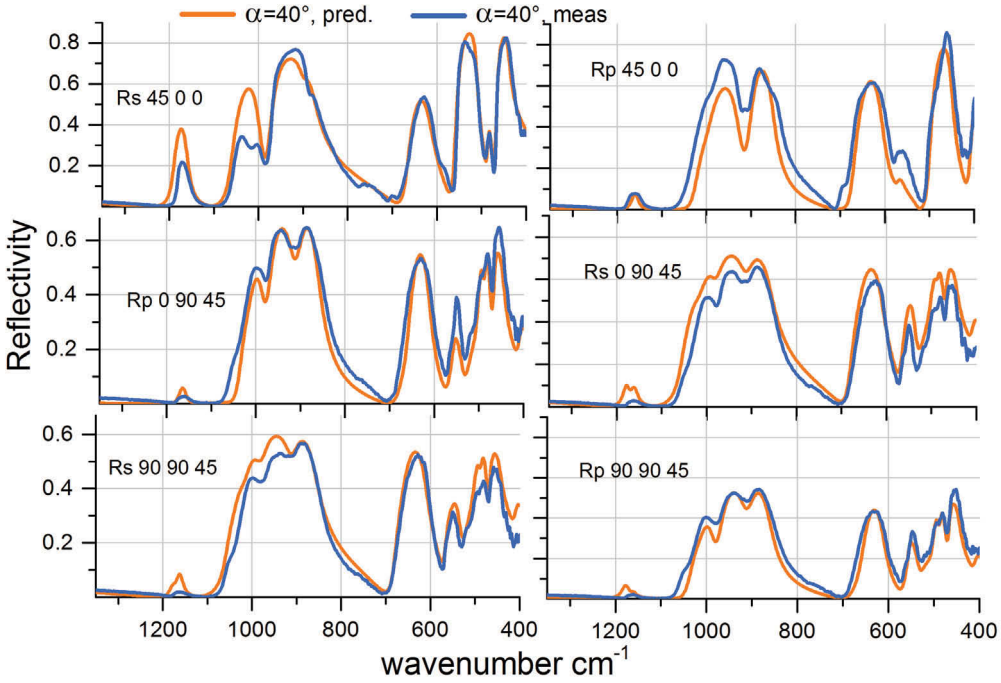

Fig. 6.10. Blue: Measured reflection spectra of topaz recorded with incidence angle α=40°. Red: predicted spectra employing the dispersion parameters given in tab. 6.6.

The general spectral features agree with each other, but as the O-H content of the sample investigated by Adams is below detection limit, a further comparison of the spectra seems inappropriate. As a consequence the oscillator parameters were also checked by recording spectra with higher incidence angles of α=20-70°and comparing those spectra to forward calculations based on the determined oscillator parameters. Although the measurements were performed with a larger pinhole diameter and a more sensitive detector, the intensity of the recorded spectra dropped for $\alpha \geq$40° rapidly, especially for the spectra recorded with p-polarized incident light. Due to the non-proportional intensity loss, which is not considered by the formalism, the spectra with incidence angle α=60° were not usable. Therefore only the spectra recorded with α=40° were chosen for fig. 6.10. Fig. 6.10 shows a satisfactory agreement between measured and predicted spectra. As the crystal had also to be mounted in another reflection unit, we were only able to measure the orientations shown in the figure.

Since finding the orientation of the dielectric axes in the topaz crystal is easily done with the help of the cross polarization spectra, there remains, like for $NdGaO_3$, the question, if dispersion analysis can also unambiguously performed if the axes are oriented in a way that generate no zero line cross polarization spectra. Therefore, the dispersion parameters of tab. 6.6 were treated in the same way as the dispersion parameters of $NdGaO_3$; they were brought into principal orientation and rotated by the same rotation matrices. The resulting spectra were also fitted pretending there was no prior knowledge about the number of oscillators or about any oscillator parame-

employed rotation	axis	resulting Φ, Θ	fitted Φ, Θ	# osc.	ε_∞
60° around x followed by	|| a_1	60°,90°	60.1°,90.3°	7	2.44
60° around z	|| a_2	-30°,-30°	-30.5°,-30.3°	10	2.19
	|| c	150°,120°=-30°,-60°	-29.6°,59.7°	9	2.35
70° around x followed by	|| a_1	30°,90°	29.8°,89.8°	7	2.44
30° around z	|| a_2	-60°,-20°	-59.7°,-20.1°	10	2.19
	|| c	120°,110°=-60°,70°	-60.3°,69.9°	8	2.39
140° around x followed	|| a_1	110°,90°=-70°,90°	-68.6°,91.7°	7	2.48
by 110° around z	|| a_2	20°,50°	22.4°,49.6°	10	2.26
	|| c	20°,-40°	19.8°,-40.4°	7	2.46

Table 6.7. First column: applied rotation to the fitted spectra of the topaz crystal brought into principal orientation. Second and third columns: The oscillators aligned parallel to the axis of column 2 have after the rotation the orientation of column 3. Fourth column: fitted orientation angles. Fifth and last column: Number of oscillators found by the fit, and fitted dielectric background.

ter. The applied rotation, the orientation for each of the crystal axes resulting from that rotation, the fitted orientation angles and the dielectric background values are summarized in tab. 6.7. The numbers of oscillators remains constant except for the oscillators that are aligned parallel to the c-axis. In spectral features that are generated by several close oscillators there will always remain uncertainties concerning oscillator parameters and number of oscillators.

To compare the fitted spectra they were also brought into principal orientation and plotted in fig. 6.11. The notation "z(30°)x(70°)" is again the abbreviation for a ro-

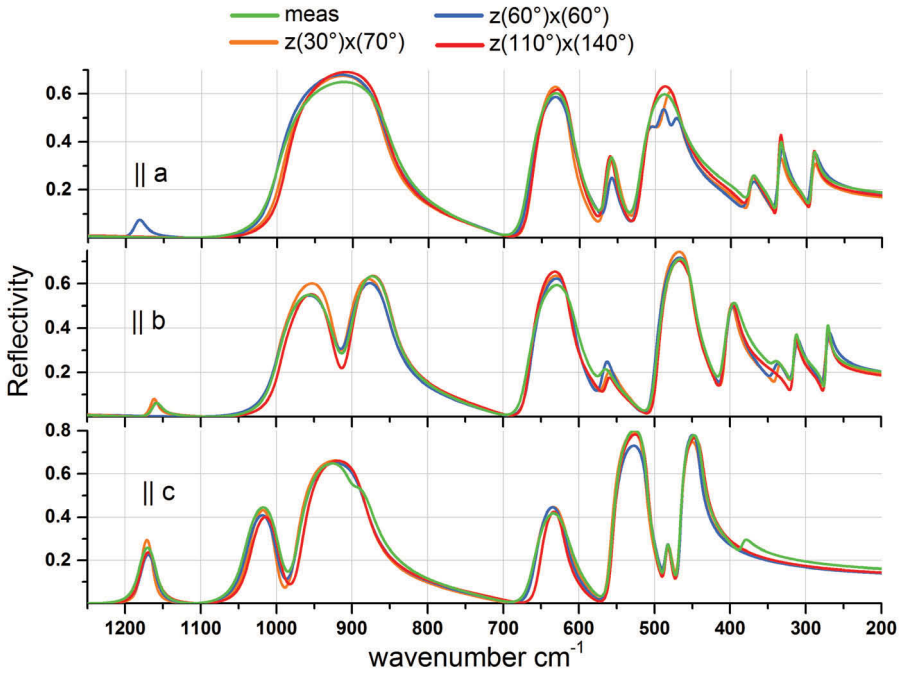

Fig. 6.11. Fitted spectra of different simulated orientations of the topaz crystal, all brought into principal orientation. The measured spectra of the crystal are also presented in principal orientation.

tation of 70° around the internal x-axis followed by the rotation of 30° around the internal z-axis. The spectra labeled with "meas" are the measured spectra of the topaz crystal also rotated into principal orientation. As topaz exhibits more vibrations than $NdGaO_3$, the differences between the fitted parameters are are little higher; most wavenumbers are found within$\approx \pm 5\,\mathrm{cm}^{-1}$, most strengths within $\approx \pm 8\,\mathrm{cm}^{-1}$and most damping constants within $\approx \pm 3\,\mathrm{cm}^{-1}$.

To conclude this chapter dispersion analysis of orthorhombic crystals is performed successfully if the optimization routine is complemented with constraints reflecting the symmetry of orthorhombic crystals plus an additional set of cross polarization spectra that fix the three different pairs of orientation angles of the transition moments. The evaluation scheme is also successful if the crystal is cut in a way that no cross polarization spectrum is reduced to a zero line. The number of fitted oscillators can vary by one or two for differently cut samples of the same crystal, which is an intrinsic uncertainty due to close resonance wavenumbers of oscillators.

If now the constraint of mutual orthogonality between the oscillators is lifted to orthogonality between only two oscillator classes, the optimization routine for orthorhombic crystals becomes the optimization routine for monoclinic crystals.

Chapter 7

Dispersion analysis of arbitrarily cut monoclinic crystals

7.1 Adaption of fit routine to monoclinic crystals

In contrary to orthorhombic crystals that have the dielectric axes oriented parallel to the crystal axes, in monoclinic crystals only one dielectric axis is oriented frequency independently parallel to a crystal axis, the b-axis. The b-axis is also parallel to one dielectric axis, the other two dielectric axes are normal to b with frequency dependent orientation on the a-c plane. The orientation additionally is different for the real and imaginary part of the dielectric tensor. Of the resulting two different symmetry types for the oscillators, the one type has its transition moments oriented parallel to the b-axis, the other type has its transition moments normal to the b-axis with arbitrary orientation in the a-c plane. For an arbitrarily cut monoclinic crystal the dielectric tensor function must be calculated employing the generalized form introduced in chapter 2, although also for monoclinic crystals there are some constraints to the fit routine that reflect the symmetry of the monoclinic crystal system. Fig. 7.1 shows a possible arrangement of transition moments for a monoclinic crystal. The transition moments oriented parallel to the b-axis are represented by the double arrow $\vec{b}$ (as the transition moments are orientation, but not direction dependent), the oscillators on the a-c plane are represented by the vectors $\vec{a}$ and $\vec{c}$. Orthogonality between $\vec{b}$ and $\vec{a}$ or $\vec{c}$ is the only condition the oscillators must fulfill, meaning the dot product must vanish,

$$\frac{\vec{a}\cdot\vec{b}}{|\vec{a}|\cdot|\vec{b}|}\stackrel{!}{=}0. \tag{7.1}$$

Translated to the fit routine this condition means that all oscillators that are oriented parallel to the b-axis are fitted with the same angle pair Φ_1 and Θ_1. The other oscillators have an angle pair Φ_k, Θ_k, of which Φ_k is fitted by the routine and Θ_k is

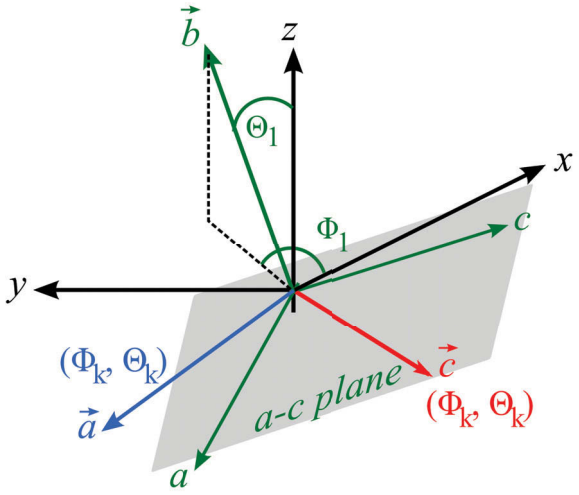

Fig. 7.1. Arrangement of oscillators in an arbitrarily cut monoclinic crystal. The green arrows a, b and c represent the unit cell parameters. Oscillators are oriented either parallel to the b-axis or normal to the b-axis on the a-c plane.

calculated according to the orthogonality condition resulting from equation 7.1

$$\Theta_k = \arctan\left(\frac{-1}{\tan\Theta_1 \cdot \cos(\Phi_1 - \Phi_k)}\right). \tag{7.2}$$

Since the spectra of monoclinic crystals are usually complex spectra with many bands due to the low symmetry, to perform dispersion analysis the one polarizer spectra also need to be supplemented by a set of cross polarization spectra. Fitting the spectra without any constraints to let the orientation of the b-axis reveal itself turned out to be not successful. Especially if the crystal is built of only slightly distorted high symmetric molecular entities which give rise to originally threefold degenerate vibrations, if undistorted. The fitted angles seems to be more or less arbitrary. Therefore, the fit routine had to be altered to a more suitable routine that was developed by fitting artificial simulated spectra of fictive monoclinic crystals.

The best approach found to handle the spectra of monoclinic crystals is at first to identify three of which two are recorded from a plane and third one is recorded with polarization direction of the incoming light normal to that plane. The other spectra with more bands are a combination of the spectra with the fewer bands. This selection of the spectra with the fewest bands prevents the generation of a higher number of initial oscillators than are necessary. For the three selected spectra starting values are generated manually, but the orientation angles for the starting values must reflect the orientation of the selected spectra. If for example the selected spectra are R_s 45 0 0, R_p 45 0 0 and R_s 0 90 0 the initial orientation angles are (Φ, Θ)=(45°,90°), (-45°,90°) and (0°,0°). For the dielectric background tensor it is sufficient to give each principal element a value estimated by the root of the reflected intensity in the higher wavenumber region.

In the next step the orientation angles of the 12 one polarizer spectra and 12 cross polarization spectra are fitted like for the spectra of orthorhombic crystals considering

the orthogonality condition for orthorhombic crystals ab initio until the error value decreases only marginally. The result of this first fit is analogously to the results for orthorhombic crystals, there are three groups of oscillators with all oscillators of one group having the same orientation angles. The trick is now that one of the three angle pairs is very close to the orientation of the b-axis.
To find out which angle pair represents the orientation of the b-axis the fit is now performed considering the monoclinic constraint given in equation 7.2. For this, the oscillators of each group are defined to be the oscillators parallel to the b-axis alternately, and the oscillators of the two other groups are considered as being parallel to the a-c plane. Each time the oscillator angles are fitted according to equation 7.2 until the error value does not decrease significantly any more. With the wrong oscillator group set parallel to the b-axis the error value decreases only minimally as the oscillators that are normally fanned out on the a-c plane are fixed to one orientation. With the right oscillator group set parallel to the b-axis the error value decreases much more as the oscillators parallel to the a-c plane can take on different angles now. The angle fit with the right group of oscillators oriented parallel to the b-axis is carried out until the error value converges. The orientation of the b-axis is now found with good accuracy. Now the orientation angles of the oscillator parameters need to be rotated into the orientation of a principal cut before the further fit routine is performed in the usual way as described in chapter 2.8.
The components (x, y, z) of a transition moment in spherical coordinates are

$$\begin{pmatrix} x \\ y \\ z \end{pmatrix} = \begin{pmatrix} \sin\Theta \cdot \cos\Phi \\ \sin\Theta \cdot \sin\Phi \\ \cos\Theta \end{pmatrix}. \tag{7.3}$$

To yield the new components (x', y', z') of the transition moment with the new orientation angles Φ', Θ' the rotation is performed by multiplying the components (x, y, z) with a rotation matrix $\mathbf{M}_{rot}^{-1}$ according to

$$\begin{pmatrix} x' \\ y' \\ z' \end{pmatrix} = \mathbf{M}_{rot}^{-1} \cdot \begin{pmatrix} x \\ y \\ z \end{pmatrix} \tag{7.4}$$

As the orientation of an arbitrarily cut cube is just a rotation out of the principal orientation, the rotation of an arbitrarily cut sample into a principal orientation needs to be described by the inverse of the matrix $\mathbf{M}_{rot}$. The rotation matrix $\mathbf{M}_{rot}$ is a combination of the rotations around the internal coordinates z, x and y, described by

$\mathbf{M}_x(\tau)$, $\mathbf{M}_y(\beta)$ and $\mathbf{M}_z(\sigma)$,

$$\begin{aligned}\mathbf{M}_{rot} &= \mathbf{M}_z(\tau)\cdot\mathbf{M}_x(\beta)\cdot\mathbf{M}_y(\sigma) \\ &= \begin{pmatrix}\cos\tau & -\sin\tau & 0\\ \sin\tau & \cos\tau & 0\\ 0 & 0 & 1\end{pmatrix}\cdot\begin{pmatrix}1 & 0 & 0\\ 0 & \cos\beta & -\sin\beta\\ 0 & \sin\beta & \cos\beta\end{pmatrix}\cdot\begin{pmatrix}\cos\sigma & 0 & \sin\sigma\\ 0 & 1 & 0\\ -\sin\sigma & 0 & \cos\sigma\end{pmatrix}\end{aligned} \tag{7.5}$$

For each desired orientation of the b-axis the matrix $\mathbf{M}_{rot}$ can be described by either a rotation around y and z or around x and z. Also does the form of the dielectric background tensor depend on the orientation of the b-axis. Tab. 7.1 summarizes the possible orientations of b in a principal cut, the spectra of the oscillators parallel to b, the form of the dielectric background tensor, and the form of the matrix $\mathbf{M}_{rot}$ to create that rotation. For the angles τ, β, σ the fitted orientation angles Φ and Θ found for the b-axis are inserted. For the rotation around the z-axis the angle Φ is employed, the rotation around the x or y axis is performed with the angle Θ. Since for the back rotation into principal cut the rotation around two axes is sufficient, the third rotation angle in $\mathbf{M}_{rot}$ is zero. The new angles in principal cut are then

$$\begin{aligned}&\Theta' = \arccos(z'), \\ &\Phi' = \arccos\left(\frac{x'}{\sin\Theta'}\right) \text{ and } \Phi' = 360 - \arccos\left(\frac{x'}{\sin\Theta'}\right) \text{ for } y' < 0.\end{aligned} \tag{7.6}$$

The distinction of cases for Φ' is necessary to level out rotations into different quadrants, when the sign of the sine or cosine functions is reversed. Otherwise the rotation yields wrong values for Φ', Θ'. The original non-principal orientation of the sample is respected by extending equation 7.7 with the orientation matrix $\mathbf{M}_{rot}$ used to calculate the components (x', y', z'),

$$\varepsilon_{X,Y,Z}(\tilde{\nu}) = A(\varphi,\theta,\psi)\cdot\varepsilon_{x,y,z}(\tilde{\nu})\cdot A^{-1}(\varphi,\theta,\psi) \tag{7.7}$$

becomes

$$\varepsilon_{X,Y,Z}(\tilde{\nu}) = A(\varphi,\theta,\psi)\cdot\mathbf{M}_{rot}\cdot\varepsilon_{x,y,z}(\tilde{\nu})\cdot\mathbf{M}_{rot}^{-1}\cdot A^{-1}(\varphi,\theta,\psi) \tag{7.8}$$

The advantage of the back rotation into principal orientation is that the number of angles that have to be fitted is reduced to only one orientation angle Φ or Θ of the oscillators normal to b. The calculation of the other orientation angle according to equation 7.2 drops out as this angle is fixed to either 0° or 90°. The remaining orientation angle φ or θ to be fitted for a certain orientation of b is given in the fourth column of tab. 7.1. Additionally, the dielectric background tensor can be fitted in its principal form and the fitted dispersion parameters can be directly compared to the parameters of a principal cut.

For example, in the initial position the b-axis of the principally cut spodumene was oriented parallel to the internal y-axis with (Φ,Θ)=(90°,90°). The fitted dispersion parameters of the principal cut were rotated by 15° around the z-axis followed by an rotation of 35° around the x-axis. The rotation matrix to perform that rotation is $\mathbf{M}_{rot}$=$\mathbf{M}_z(35°)\mathbf{M}_x(15°)\mathbf{M}_y(0°)$. The resulting orientation of the b-axis after the rotation is (Φ,Θ)=(-55°,-75°). To rotate the oscillators parallel to the b-axis back to (Φ,Θ)=(90°,90°) the inverse matrix $\mathbf{M}_{rot}^{-1}$=$\mathbf{M}_z$(90-55°)$\mathbf{M}_x$(90-75°)$\mathbf{M}_y(0°)$ according to tab. 7.1 is employed.

After this intermediate step the optimization is continued as usual. In the end the orientation angles of b in the Matrix $\mathbf{M}_{rot}$ are also included into the fit routine for a few cycles to find the orientation of b a little more accurate. The available monoclinic crystals were yttrium silicate and spodumene, but only in principal cut. Due to the lack of single crystal monoclinic samples in arbitrary cut the calculated dispersion parameters of the principally cut cubes were rotated into arbitrary orientation, using equations 7.3-7.7 with the matrix $\mathbf{M}_{rot}$ in its normal form and not as inverse matrix, since it is now a forward rotation outgoing from a principal orientation.

b || to	spectra of osc.|| to b	Φ,Θ of b	Φ,Θ $\perp$ to b	ε_∞	rotation matrix $\mathbf{M}_{rot}^{-1}$
z	R_s 0 90 0, R_p 90 90 90	0°,0°	ϕ,90°	$\begin{pmatrix} \varepsilon_{xx} & \varepsilon_{xy} & 0 \\ \varepsilon_{xy} & \varepsilon_{yy} & 0 \\ 0 & 0 & \varepsilon_{zz} \end{pmatrix}$	$\mathbf{M}_z(\Phi)\cdot\mathbf{M}_x(0°)\cdot\mathbf{M}_y(\Theta)$
y	R_p 0 0 0, R_p 0 90 0	90°,90°	0°,ϑ	$\begin{pmatrix} \varepsilon_{xx} & 0 & \varepsilon_{xz} \\ 0 & \varepsilon_{yy} & 0 \\ \varepsilon_{xz} & 0 & \varepsilon_{zz} \end{pmatrix}$	$\mathbf{M}_z(90°+\Phi)\cdot\mathbf{M}_x(90°+\Theta)\cdot\mathbf{M}_y(0°)$
x	R_s 0 0 0, R_s 90 90 90	0°,90°	90°,ϑ	$\begin{pmatrix} \varepsilon_{xx} & 0 & 0 \\ 0 & \varepsilon_{yy} & \varepsilon_{yz} \\ 0 & \varepsilon_{yz} & \varepsilon_{zz} \end{pmatrix}$	$\mathbf{M}_z(\Phi)\cdot\mathbf{M}_x(0°)\cdot\mathbf{M}_y(90°+\Theta)$

Table 7.1. First and second column: Of a spectra set consisting of 12 one polarization spectra two spectra originate from the oscillators parallel to the b-axis. Third column: There are three different orientations of b in a principally oriented sample. Fourth column: Remaining orientation angle to be fitted if the sample is in principal orientation. Fifth column: Form of dielectric background tensor depending on orientation of b. Last column: Rotation matrix that rotates an arbitrarily cut sample into the desired principal orientation.

7.2 Results of dispersion analysis of monoclinic crystals

As of the spodumene and yttrium silicate crystal only a principal cut was available, at first the dispersion parameters of the spodumene sample in principal cut are presented in tab. 7.2. The dispersion parameters of tab. 7.2 were rotated with $\mathbf{M}_{rot}$=$\mathbf{M}_z(35°)\mathbf{M}_x(15°)\mathbf{M}_y(0°)$ (rotation of 15° around internal x-axis followed by a rotation of 35° around internal z-axis) to simulate an arbitrarily cut sample. The so generated spectra set of an arbitrary cut were fitted as described previously, using now prior knowledge of any oscillator parameter. The fitted dispersion parameters of the simulated spectra are shown in tab. 7.3. The fitted orientation of the b-axis in the arbitrarily cut cube was (Φ, Θ)=(56.4°±3°,-73.3°±3°). The parameters were rotated back with $\mathbf{M}_{rot}^{-1}$=$\mathbf{M}_z$(90-56.4°)$\mathbf{M}_x$(90-73.3°)$\mathbf{M}_y(0°)$ into principal orientation so that both tables can be directly compared to each other.

		$\tilde{\nu}_j$ cm^{-1}	S_j cm^{-1}	γ_j cm^{-1}	Φ_j°	Θ_j°
||b	1	1096.8	574.0	29.5	90.0	90.0
	2	1067.0	479.0	16.3	90.0	90.0
	3	858.3	202.7	14.4	90.0	90.0
	4	572.5	254.8	21.3	90.0	90.0
	5	526.9	207.6	19.7	90.0	90.0
	6	484.2	451.5	15.3	90.0	90.0
	7	446.0	298.8	16.6	90.0	90.0
		316.4	74.8	9.1	90.0	90.0
	8	290.5	305.6	14.3	90.0	90.0
	9	223.7	258.9	5.7	90.0	90.0
⊥b	10	1078.5	338.7	22.8	0.0	169.6
	11	1016.0	751.2	21.0	0.0	83.4
	12	883.3	679.0	26.1	0.0	179.4
	13	620.9	371.5	17.0	0.0	21.3
		600.2	222.2	23.1	0.0	19.8
	14	468.3	573.1	22.5	0.0	73.6
	15	449.5	421.6	16.9	0.0	132.8
	16	403.0	191.7	8.6	0.0	91.9
	17	397.6	127.4	6.4	0.0	4.6
	18	381.6	201.4	19.6	0.0	90.1
	19	359.6	383.8	8.8	0.0	22.0
	20	333.5	197.5	10.1	0.0	5.7
	21	301.1	180.6	16.1	0.0	165.3
	22	269.8	294.8	11.0	0.0	71.5
	23	229.8	255.4	12.5	0.0	145.8
	24	226.3	281.0	8.9	0.0	111.6

$$\varepsilon_\infty = \begin{pmatrix} 2.56 & 0 & 0.15 \\ 0 & 2.42 & 0 \\ 0.15 & 0 & 2.49 \end{pmatrix}$$

Table 7.2. Calculated dispersion parameters of monoclinic spodumene in principal cut.

		$\tilde{\nu}_j$ cm^{-1}	S_j cm^{-1}	γ_j cm^{-1}	Φ_j°	Θ_j°
||b	1	1099.9	484.1	24.1	90.0	90.0
	2	1065.6	555.2	17.9	90.0	90.0
	3	858.3	205.2	11.7	90.0	90.0
	4	572.3	250.6	20.9	90.0	90.0
	5	527.2	187.3	14.8	90.0	90.0
	6	483.5	444.9	16.3	90.0	90.0
	7	446.1	313.2	14.7	90.0	90.0
	8	291.4	323.4	19.7	90.0	90.0
	9	224.2	253.2	5.8	90.0	90.0
⊥b	10	1082.1	324.9	17.6	0.0	170.3
	11	1020.9	727.3	18.6	0.0	84.4
	12	883.9	650.3	22.6	0.0	180
	13	618.8	413.3	18.4	0.0	21.4
	14	467.3	575.3	20.3	0.0	80.1
	15	451.2	344.8	16.6	0.0	149.2
	16	405.7	196.5	9.1	0.0	104.0
	17	397.4	137.1	6.8	0.0	35.8
	18	388.3	234.1	20.2	0.0	105.8
	19	358.6	349.6	10.2	0.0	23.1
	20	333.6	245.6	15.1	0.0	12.4
		315.5	88.7	8.0	0.0	78.1
	21	302.3	187.0	12.7	0.0	172.8
	22	271.3	265.1	10.8	0.0	79.0
		242.3	202.8	15.7	0.0	42.0
	23	234.5	289.6	10.0	0.0	122.3
	24	223.3	201.4	5.0	0.0	134.0

$$\varepsilon_\infty = \begin{pmatrix} 2.50 & 0 & 0.13 \\ 0 & 2.36 & 0 \\ 0.13 & 0 & 2.42 \end{pmatrix}$$

Table 7.3. Calculated dispersion parameters of spodumene in (an artificial) arbitrary orientation, rotated back into principal orientation.

		$\tilde{\nu}_j$	S_j	γ_j	Φ_j	Θ_j
||b	1	960.5	93.3	8.2	0.0	0.0
	2	913.8	426.9	9.6	0.0	0.0
	3	885.5	399.0	8.9	0.0	0.0
	4	594.7	231.0	11.9	0.0	0.0
	5	561.3	162.3	8.3	0.0	0.0
		511.4	109.3	13.8	0.0	0.0
	6	437.9	209.8	11.0	0.0	0.0
	7	347.0	417.8	7.2	0.0	0.0
	8	308.8	209.1	7.9	0.0	0.0
	9	269.6	83.5	4.4	0.0	0.0
	10	249.2	286.3	5.7	0.0	0.0
	11	223.3	186.8	6.4	0.0	0.0
	12	200.7	128.7	6.1	0.0	0.0
	13	188.5	274.0	4.2	0.0	0.0
⊥b	14	974.4	567.7	8.5	107.4	90.0
	15	971.7	192.4	6.3	103.8	90.0
	16	901.9	453.5	6.8	29.5	90.0
	17	871.8	396.9	7.6	11.1	90.0
	18	567.6	284.3	13.7	116.5	90.0
		540.5	47.9	18.4	93.4	90.0
	19	539.5	228.5	7.8	12.8	90.0
	20	514.0	426.9	9.5	125.0	90.0
	21	507.5	153.1	9.6	46.1	90.0
	22	461.5	215.2	19.1	142.4	90.0
	23	461.2	162.1	8.6	16.1	90.0
	24	412.1	199.1	13.9	132.3	90.0
	25	379.5	333.0	6.3	53.0	90.0
	26	312.5	439.9	8.7	13.0	90.0
	27	311.9	352.6	8.4	100.7	90.0
	28	265.5	180.8	7.7	2.1	90.0
	29	230.6	190.1	5.2	134.8	90.0
	30	230.6	288.1	9.9	4.9	90.0
	31	225.0	248.0	10.1	57.4	90.0
		217.1	272.2	4.7	79.0	90.0
	32	170.1	120.2	6.2	166.7	90.0
	33	145.2	119.7	5.0	165.5	90.0

$$\varepsilon_\infty = \begin{pmatrix} 2.38 & 0.03 & 0 \\ 0.03 & 3.09 & 0 \\ 0 & 0 & 3.13 \end{pmatrix}$$

Table 7.4. Calculated dispersion parameters of yttrium silicate of a principally cut cube.

		$\tilde{\nu}_j$	S_j	γ_j	Φ_j	Θ_j
||b	1	960.6	94.3	12.7	0.0	0.0
	2	912.9	428.1	11.2	0.0	0.0
	3	885.3	406.0	8.8	0.0	0.0
	4	593.3	235.4	15.0	0.0	0.0
	5	561.3	210.5	16.0	0.0	0.0
	6	436.3	204.8	14.6	0.0	0.0
		352.6	173.7	15.0	0.0	0.0
	7	345.4	384.6	9.8	0.0	0.0
	8	309.0	224.7	10.6	0.0	0.0
	9	270.4	91.6	8.1	0.0	0.0
	10	249.4	295.1	9.8	0.0	0.0
	11	224.2	196.2	10.1	0.0	0.0
	12	202.5	124.8	8.2	0.0	0.0
	13	189.8	284.0	8.5	0.0	0.0
⊥b	14	973.9	533.4	6.6	100.4	90.0
	15	986.3	212.1	9.2	106.4	90.0
	16	900.4	482.8	8.2	30.1	90.0
	17	869.6	400.6	13.2	-5.94	90.0
	18	566.6	277.8	15.0	111.5	90.0
	19	537.6	218.6	14.2	11.6	90.0
	20	512.3	435.9	14.9	119.6	90.0
	21	506.4	170.8	15.0	39.0	90.0
	22	463.9	232.4	16.0	133.9	90.0
	23	461.1	172.3	14.8	14.5	90.0
	24	412.4	216.0	15.8	133.4	90.0
	25	378.0	351.6	11.6	46.9	90.0
	26	316.2	274.1	10.5	14.8	90.0
		312.2	367.7	9.8	52.8	90.0
	27	311.1	370.9	14.1	141.8	90.0
	28	266.4	195.6	10.2	-0.75	90.0
	19	229.7	296.2	10.0	137.4	90.0
	30	230.5	310.1	10.1	28.3	90.0
	31	221.3	280.9	5.1	67.4	90.0
	32	171.0	147.2	9.4	189.5	90.0
	33	149.6	132.7	10.7	164.6	90.0

$$\varepsilon_\infty = \begin{pmatrix} 2.29 & 0.01 & 0 \\ 0.01 & 3.09 & 0 \\ 0 & 0 & 3.14 \end{pmatrix}$$

Table 7.5. Calculated dispersion parameters of an (simulated) arbitrarily cut cube of yttrium silicate.

The first block of both tables shows the oscillators oriented parallel to b, the second block show the oscillators normal to b. The unlabeled oscillator of the principal cut (tab. 7.2) at 316 cm^{-1} was not reproduced by the fit for the arbitrary cut (tab. 7.3). Instead this oscillator was given an orientation normal to the b-axis. Of the oscillators oriented normal to b the unlabeled oscillator of the principal cut was also not reproduced. Also, for the arbitrary cut the fit routine produced an oscillator at 242 cm^{-1} that is not part of the oscillators of the principal cut. Apart from this, the oscillator parameters of the principal cut could be satisfyingly reproduced with the (simulated) spectra of

an arbitrary cut, also the orientation angles match each other very well for most of the oscillators. The dielectric background tensors agree within calculation errors.
In tab. 7.4 the dispersion parameters of yttrium silicate in principal cut are listed. To generate the spectra of an arbitrarily cut cube the parameters were rotated by $\mathbf{M}_{rot}$=$\mathbf{M}_z(60°)\mathbf{M}_x(0°)\mathbf{M}_y(20°)$, which is an rotation of 20° around the internal y-axis followed by a rotation of 60° around the z-axis. The resulting orientation of the b-axis is (Φ,Θ)=(60°,20°). The so generated artificial spectra were also evaluated not using any prior knowledge about the dispersion parameters. The dispersion parameters resulting from the fit of the arbitrarily orientated cube are given in tab. 7.5. The fitted orientation of the b-axis for the arbitrary cut was (Φ,Θ)=(66.3°±4°,19.1°±4°). To compare the results with the dispersion parameters of the principal cut the dispersion parameters of tab. 7.5 were rotated with $\mathbf{M}_{rot}^{-1}$=$\mathbf{M}_z(66.3°)\mathbf{M}_x(0°)\mathbf{M}_y(19.1°)$ back into principal orientation of b with (Φ,Θ)=(0°,0°). The numbers of oscillators for both the principal and arbitrary cut differ by only one, which is a good result considering the total numbers of oscillators. Except for two unlabeled oscillators, all other oscillator parameters and the dielectric background tensors agree with each other, so the described approach to handle the spectra monoclinic materials also works for quite complex spectra.
Fig. 7.2 and 7.3 show the spectra of spodumene and yttrium silicate. The measured spectra of the principally cut cube are in red ("meas"). The corresponding fitted spectra employing tab. 7.2 and 7.4 are in blue ("original fit"). The fitted spectra of the simulated arbitrarily cut cube are shown in green ("sim. spec"), employing tables 7.3 and 7.5. Additionally, the cross polarization spectra are also inserted into the diagrams. The measured cross polarization spectra are in dark gray ("meas"), the corresponding spectra of the arbitrary cut are in purple ("original fit"). The fitted spectra of the (simulated) principal cut are in orange ("sim. spek"). As expected, the cross polarization spectra measured with polarization direction of the incident light parallel to the b-axis are zero. The first spectrum in both figures is the spectrum of the oscillators oriented parallel to the b-axis. The other spectra are the four spectra recorded from the surface normal to the b-axis.
Overall, the agreement between the fitted spectra of the principally cut cube and the fitted spectra of the arbitrarily cut cube is better than the agreement to the measured spectra, especially for the cross polarization spectra. This is due to the fact that the measured spectra contain effects resulting from different surface qualities and perhaps misalignment errors, whereas the spectra of the simulated sample are "perfect" spectra without any disturbing effects. The figures also show that in spite of some orientation angles being not correctly reproduced by the fit routine, the fitted spectra can still match the measured spectra very well. Oscillator parameters, especially the orientation angles, that go into the wrong direction are compensated by other oscillator

parameters. This is due to the intrinsic uncertainty created by many overlapping bands in the spectra.

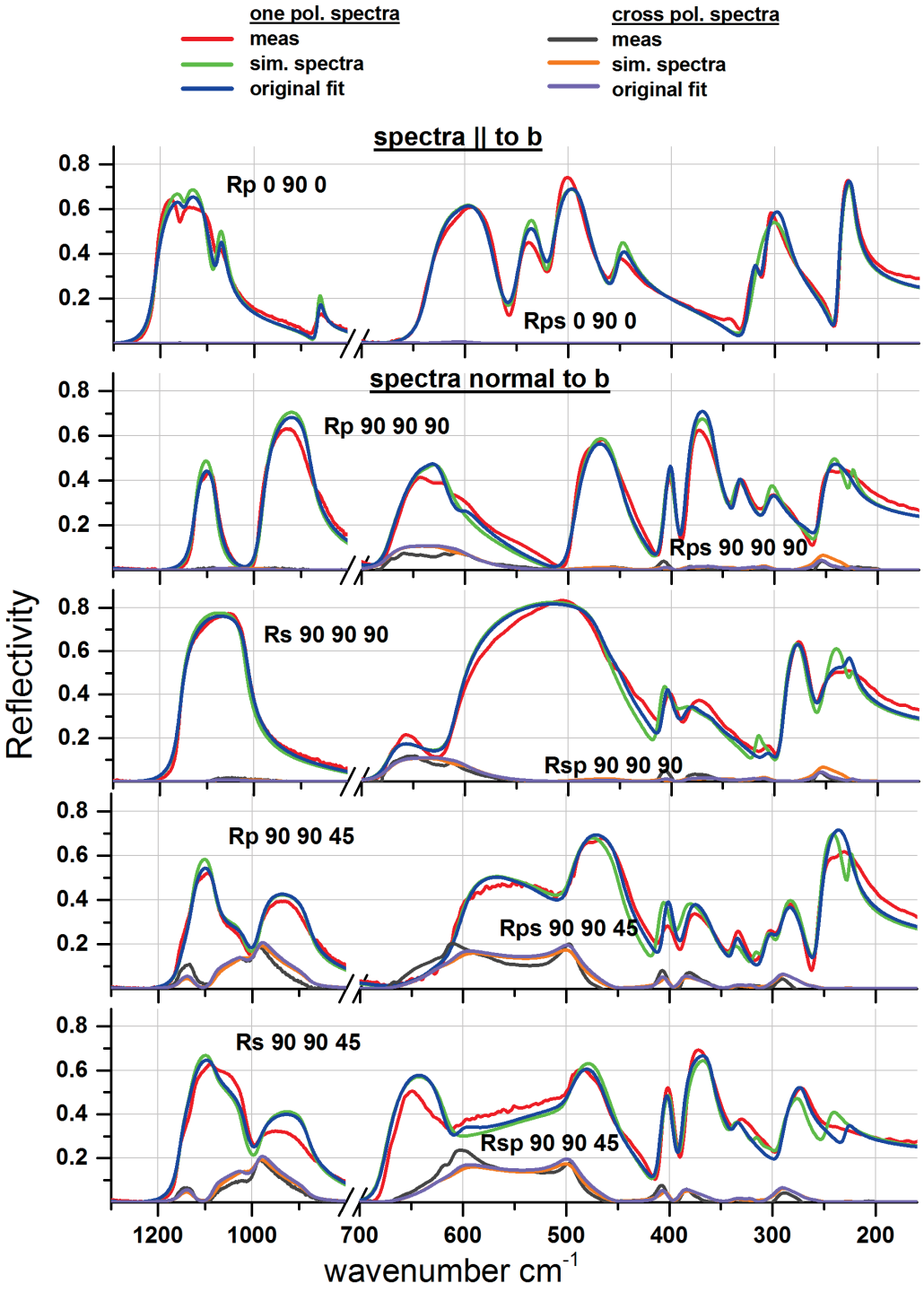

Fig. 7.2. Measured one polarizer (red) and cross polarization spectra (dark gray) with the fitted one polarizer (blue) and fitted cross polarization spectra (purple) of a spodumene cube in principal cut. The fitted one polarizer (green) and cross polarization spectra (orange) of an arbitrarily oriented cube are rotated back into principal orientation to compare them with the measured spectra.

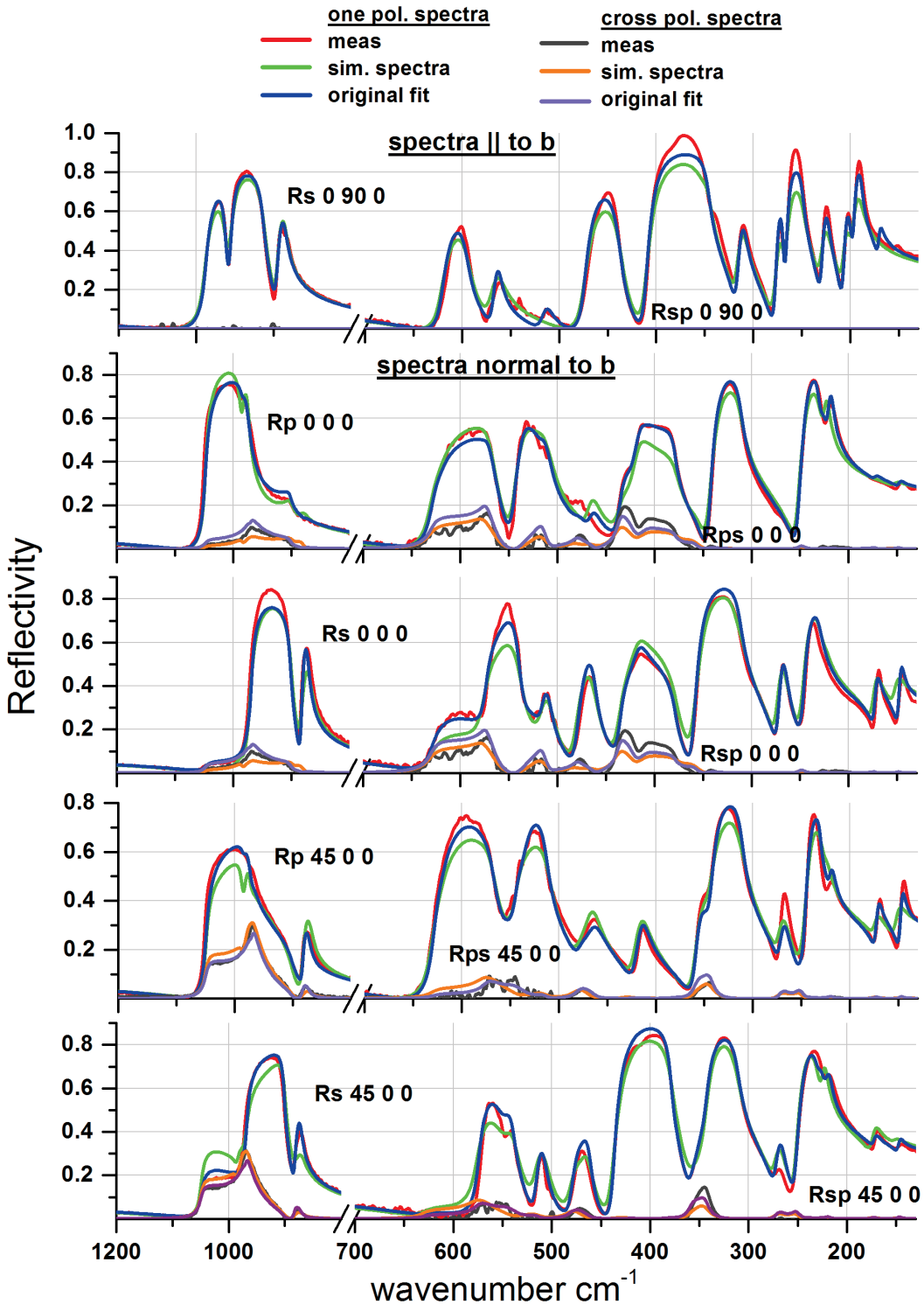

Fig. 7.3. Measured one polarizer (red) and cross polarization spectra (dark gray) with the fitted one polarizer (blue) and fitted cross polarization spectra (purple) of a yttrium silicate cube in principal cut. The fitted one polarizer (green) and cross polarization spectra (orange) of the arbitrarily oriented cube are rotated back into principal orientation to compare them with the measured spectra.

To conclude this chapter, the evaluation of a spectra set of monoclinic crystals is not as straight forward as the spectra sets of the other described crystal systems. To handle the spectra of monoclinic crystals the conditions concerning the orientation of the transition moments for orthorhombic crystals has to be included to the monoclinic fit routine in order to find the right orientation of the b-axis. An additional intermediate step that rotates the dispersion parameters of an arbitrary cut sample to principal orientation is necessary for the optimization routine to find the best oscillator parameters that represent the measured spectra.
Yet no arbitrarily cut monoclinic samples were available, dispersion analysis was successfully applied to artificially created reflection spectra. The measured spectra could be reproduced very well by a forward calculation using the fitted dispersion parameters of the artificially generated spectra of different cuts.

Chapter 8

Summary

Until now dispersion analysis of crystals with lower symmetry than cubic symmetry was only possible if spectra of the crystals were recorded in principal cut and orientation. To perform generalized dispersion analysis of arbitrarily cut crystals with a priori unknown orientation an appropriate set of spectra and evaluation scheme to reproduce the measured spectra is necessary. In this thesis a detailed procedure that respects the characteristic symmetries of each crystal system to perform generalized dispersion analysis and to calculate the dielectric tensor function is worked out. It is now no longer necessary to use the restriction of principal orientation as measurements on any crystal face of any orientation can be used as input for generalized dispersion analysis since the developed formalism is independent on the crystal symmetry. Generalized dispersion analysis can be performed now without any a priori knowledge about the orientation of the crystal in question.

The measurement scheme is kept relatively simple, except for a (FT)IR-spectrometer and the polarizers no special equipment is necessary. The optimization routine is written in Matlab runs on a standard PC, the speed of the optimization is only dependent on the processor performance. Therefore, generalized dispersion analysis on arbitrarily cut crystals is accessible to any institute equipped with a IR-spectrometer. To perform generalized dispersion analysis, the crystal in question does not need to be of utmost purity. Crystals with small inclusions or dislocations that cause the Laue reflexes to be diffuse or blurry instead of point-shaped can also be employed.

The sample preparation comprises the optical polishing of three different crystal faces that are not coplanar to each other. The cut of the crystal into a cube is not mandatory, yet it facilitates the subsequent calculations. The minimal size of the crystal is restricted by the sample holder and the ability of a decent orientation of the crystal in the spectrometer. If the recorded spectra are desired to be reproducible with other samples of the same crystal it is advisable to determine the Miller indices of the crystal faces first.

The most important step of the generalized dispersion analysis is a basis transformation from the laboratory frame to the one representing the principal axes of the crystal itself. The transformation is performed by applying an Euler matrix with three rotation angles to the dielectric tensor function. In this way, from enough measurements, the oscillator parameters can be determined and the dielectric tensor function in all directions can be calculated. The necessary number of spectra to gain reliable information about the dispersion parameters was investigated. The spectra set employed for generalized dispersion analysis is a combination of four spectra of each of three different faces of the crystal sample recorded with different polarization states of the incoming light. Additionally investigations about the uncertainties of dispersion parameters depending on the oscillator strength and proximity of the resonance wavenumbers of adjacent oscillators were carried out. Depending on the quality of the spectra (given by the surface quality of the sample and signal-to-noise ratio) and the overlap of adjacent reflection bands the precision of the calculated oscillator parameters varies from 5 to 20%.

The scheme to record the spectra of a crystal sample was standardized, so it can be applied independently to all crystal systems. Furthermore, generalized dispersion analysis is not restricted to reflection spectra recorded under normal incidence, but can be applied to reflection spectra of any angle of incidence (unless the overall reflected intensity does not drop too strongly for high incidence angles. For higher incidence angles the reflection spot of a beam increases, but due to the pinholes of the sample holder the probed sample area stays the same, only the intensity of the incident light drops). For spectra sets with varying reflectivity from one spectrum to the other due to surface imperfections also a way to integrate such spectra sets to the optimization routine was found by introducing constant multiplication factors for the respective spectra.

The two triclinic crystals $CuSO_4 \cdot 5\,H_2O$ and $K_2Cr_2O_7$ were used for proof-of-concept experiments as these crystals have no symmetry-forced conditions concerning the orientation of their transition moments. From the programming point of view they represent the easiest crystal system to evaluate with the generalized formalism. Outgoing from the results for triclinic crystals for the uniaxial, orthorhombic and monoclinic crystal systems the optimization routine was complemented by constraints concerning the orientation of the transition moments and form of dielectric background tensor that represent the symmetry of the crystal system in question. The constraints reduce the parameter space for the fit routine considerably. For orthorhombic and monoclinic crystals the evaluation scheme needs to be supported by including a set of cross polarization spectra into the optimization routine as otherwise the orientation angles of the transition moments are not fitted unambiguously. The formalism is designed in a way that the calculation of the additional cross polarization spectra does not require

extra computing capacity.
To develop the measurement and evaluation scheme for the different crystal systems already investigated crystals were chosen to compare the calculated results with the existing literature. At least two crystals with different properties as representative for each of the investigated crystal systems were employed to make the developed scheme more reliable. The calculated oscillator parameters were proven valid by using them to predict spectra of polycrystalline samples, spectra of different cuts or spectra recorded with different angles of incidence and compare the predicted spectra with experimental spectra.
With the developed scheme for generalized dispersion analysis thorough investigations of interesting materials are possible; e.g. the investigated $NdGaO_3$ is a widely used substrate for different applications, yet a dispersion analysis of $NdGaO_3$ has not been performed by now, or the monoclinic double tungstates, that are promising laser crystals. Also in-situ examinations of phase transitions become possible now. Although in-situ experiments of phase transitions are also possible with x-ray investigations, the dielectric tensor function remains only accessible with generalized dispersion analysis. The modified crystal structure after the phase transition will be identifiable by generalized dispersion analysis and dispersion analysis of such altered phases would be possible even if the orientation of the new phase would not be known a priori.
For example the orthorhombic and uniaxial crystal systems are distinguishable by the occurrence of degenerate oscillators in the uniaxial crystal system, that are no longer present in the orthorhombic system. The orthorhombic and monoclinic system would be distinguishable by the lifted condition of mutual orthogonality of the transition moments. While in the orthorhombic system the transition moments are aligned parallel to the crystal axes, in the monoclinic system the orientation of the transition moments fans out in a plane normal to the last remaining predominant direction. The monoclinic and triclinic system in turn can be distinguished by the vanished predominant direction that is present in the monoclinic system. Also an altered degree of distortion of high symmetric compounds like moieties in tetrahedral or octahedral coordination could be observed by an altered splitting of the former threefold degenerate vibration before and after the phase transition.
What is more, even if the starting point is a principal cut of an optically uniaxial or orthorhombic crystal, it is obvious that under a phase change to monoclinic or triclinic structure the advantage of allowing to separate dielectric tensor components with linear polarized radiation of this particular cut would necessarily cease to exist.
This work is an important step at being able to differentiate between cubic, uniaxial, orthogonal, monoclinic and triclinic crystal system by adapting the measurement and evaluation scheme developed for each of the crystal systems. To conclude this work with an outlook, it might be possible based on the results of this work, to develop a

generalized algorithm that does not only perform generalized dispersion analysis on crystal sample of unknown cut and orientation without intervention of the operator, but also determine the a priori unknown crystal system of that sample. This algorithm could be implemented in a way that only the measurements of the spectra have to the done manually while the optimization routine runs automatically without being supervised by the operator.

Chapter 9

Zusammenfassung

Bis jetzt war die Dispersionsanalyse von Kristallen mit niedrigerer Symmetrie als kubischer Symmetrie nur mit Spektren der betreffenden Kristalle im Hauptschnitt möglich. Um die verallgemeinerte Dispersionsanalyse an beliebig geschnittenen Kristallen mit unbekannter Orientierung durchzuführen, sind sowohl ein bestimmter Spektrensatz als auch ein passendes Auswerteprogramm notwendig, um die gemessenen Spektren zu reproduzieren. In dieser Dissertation wird ein detailliertes Verfahren ausgearbeitet, welches die charakteristischen Symmetrien eines Kristallsystems zur Durchführung der Dispersionsanalyse und Berechnung der dielektrischen Tensorfunktion berücksichtigt. Die Beschränkung auf den Hauptschnitt wird dadurch aufgehoben, da nun Reflexionsspektren beliebiger Kristallflächen in beliebiger Orientierung zur verallgemeinerten Dispersionsanalyse verwendet werden können. Der erarbeitete Formalismus ist unabhängig von der Kristallsymmetrie.
Das entwickelte Messverfahren ist relativ einfach gehalten, außer eines (FT) IR-Spektrometers und der Polarisatoren ist keine weitere Laborausstattung notwendig. Die Fitroutine ist in Matlab geschrieben und läuft auf einem gewöhnlichen PC. Die Geschwindigkeit der Optimierung ist lediglich von der Leistungsfähigkeit des Prozessors abhängig. So wird die verallgemeinerte Dispersionsanalyse beliebig geschnittener Kristalle für alle Institute zugänglich, die mit einem IR-Spektrometer ausgestattet sind. Um die verallgemeinerte Dispersionsanalyse durchzuführen, muss der Kristall auch nicht von äußerster Reinheit sein. Kristalle mit kleinen Einschlüssen oder Versetzungen, wodurch die sonst scharfen und punktförmigen Laue-Reflexe unscharf oder verwischt werden, sind ebenfalls geeignet.
Die Probenvorbereitung umfasst das Polieren dreier, nicht koplanarer Kristallflächen. Der Schnitt eines Kristalls in einen Würfel ist nicht zwingend notwendig, jedoch erleichtert ein solcher Schnitt die nachfolgenden Berechnungen. Die minimale Größe einer Kristallprobe ist einerseits durch den Probenhalter, und andererseits durch die Erhaltung der Möglichkeit einer genauen Ausrichtung des Kristalls im Spektrometer

gegeben. Falls die gemessenen Spektren eines Würfels oder sonstigen Probe in bestimmter Orientierung reproduzierbar sein sollen, ist es ratsam, zuerst die Miller-Indizes der Kristallflächen zu bestimmen um die Information über die Lage des Würfels oder der Probe im ursprünglichen Kristall zu erhalten.
Der wichtigste Schritt während der verallgemeinerten Dispersionsanalyse ist eine Transformation des Laborkoordinatensystem in das Koordinatensystem des Kristalls selbst. Die Transformation wird durchgeführt, indem eine Euler-Matrix mit drei Drehwinkeln auf die dielektrische Tensorfunktion angewendet wird. Auf diese Art können die Oszillatorparameter mit Hilfe einer ausreichenden Anzahl an Spektren bestimmt und die dielektrische Funktion in beliebiger Kristallrichtung berechnet werden. Die Anzahl an Spektren, die notwendig ist um zuverlässige Informationen über die Dispersionsparameter zu erhalten, wurde ebenfalls untersucht. Der zur verallgemeinerten Dispersionsanalyse angemessene Spektrensatz ist eine Kombination aus vier Spektren von drei unterschiedlicher, nicht koplanarer Kristallflächen, die mit unterschiedlicher Polarisationsrichtung der einfallenden Strahlung aufgenommen werden.
Zusätzliche Untersuchungen zur Unsicherheit der Dispersionsparameter in Abhängigkeit von der Oszillatorstärke und des Abstands der Resonanzwellenzahl benachbarter Oszillatoren wurden ebenfalls durchgeführt. In Abhängigkeit von der Qualität der Spektren (gegeben durch die Oberflächenqualität und das Signal-zu-Rausch-Verhältnis) und die Überlagerung benachbarter Reflexionsbanden variiert die Genauigkeit der berechneten Oszillatorparameter zwischen 5 und 20%.
Das Verfahren zur Messung der Reflexionsspektren wurde standardisiert, wodurch es unabhängig für alle Kristallsysteme angewendet werden kann. Weiterhin ist die verallgemeinerte Dispersionsanalyse nicht mehr auf Reflexionsspektren angewiesen, die unter (fast) senkrechtem Einfall gemessen wurden, sondern kann nun auch auf Reflexionsspektren, die mit beliebigem Einfallswinkel gemessen wurden, angewandt werden (solange die Gesamtintensität der Reflexionsspektren nicht zu sehr abfällt. Für größere Einfallswinkel wird zwar der Reflexionsfleck größer, jedoch bleibt die bestrahlte Fläche der Probe bedingt durch die Blende des Probenhalters die gleiche, nur die Intensität der einfallenden Strahlung auf der Kristallfläche sinkt).
Für einen Spektrensatz, in dem die reflektierte Intensität zwischen den einzelnen Spektren aufgrund von Oberflächenfehlern schwankt, wurde ebenfalls eine Lösung gefunden, um diesen Spektrensatz für die Fitroutine verwenden zu können. Für jedes dieser Spektren wird ein konstanter Multiplikationsfaktor eingeführt, der die unterschiedlichen Reflexionsvermögen ausgleicht. Mit den beiden triklinen Kristallen $CuSO_4{\cdot}5\,H_2O$ und $K_2Cr_2O_7$ wurde die prinzipielle Durchführbarkeit der verallgemeinerten Dispersionsanalyse erwiesen, da es für trikline Kristalle keine Symmetrie bedingten Einschränkungen bezüglich der Orientierung der Übergangsmomente gibt. Aus Sicht der Programmgestaltung stellt diese Kristallklasse die einfachste Klasse dar. Ausgehend von

den Ergebnissen für trikline Kristalle wurde die Fitroutine für jeweils optisch einachsige, orthorhombische und monokline Kristalle separat angepasst. Grundlage dabei sind die Bedingungen für die Orientierung der Übergangsmomente und Form des dielektrischen Hintergrundes, welche sich aus der jeweiligen Kristallsymmetrie ergeben. Die für jede Kristallklasse charakteristische Anordnung der übergangsmomente reduziert den Parameterraum für die Fitroutine ganz erheblich. Für orthorhombische und monokline Kristalle muss das Auswerteverfahren durch einen Satz von Kreuzpolarisationsspektren ergänzt werden, da anderenfalls die Orientierungen der übergangsmomente nicht eindeutig berechnet werden. Der Formalismus wurde so gestaltet, dass die Berechnung der Kreuzpolarisationsspektren keinen höheren Rechenaufwand bedeutet. Für die Entwicklung des Mess- und Auswerteverfahrens für die verschiedenen Kristallsysteme wurden bereits hinreichend untersuchte Kristalle ausgewählt, um die Ergebnisse dieser Arbeit mit der existierenden Literatur vergleichen zu können. Aus jeder Kristallklasse wurden mindestens zwei Kristalle mit unterschiedlichen Eigenschaften ausgewählt, um die Zuverlässigkeit des entwickelten Verfahrens zu erhöhen.
Um die berechneten Oszillatorparameter zu überprüfen, wurden diese zur Vorausberechnung von Spektren polykristalliner Proben, Spektren von unterschiedlichen Kristallschnitten sowie von Spektren, die mit unterschiedlichem Einfallswinkel gemessen wurden, verwendet. Die vorausberechneten Spektren wurden dann mit den entsprechenden gemessenen Spektren verglichen. Das vorgestellte Verfahren zur Dispersionsanalyse ermöglicht nun vollständige Untersuchungen von vielversprechenden Materialien, z.B. ist das verwendete $NdGaO_3$ ein häufig benutztes Substrat für verschiedene Anwendungen, dennoch wurde eine vollständige Dispersionsanalyse zur Charakterisierung des Materials noch nicht durchgeführt; oder die monoklinen Diwolframate als Laserkristalle.
Ebenso wird die in-situ Untersuchung von Phasenübergängen mit dieser Methode ermöglicht. Obwohl in-situ Experimente auch mit Röntgenstrahlung durchgeführt werden, bleibt die dielektrische Tensorfunktion nur mit der verallgemeinerten Dispersionsanalyse zugänglich. Mittels verallgemeinerter Dispersionsanalyse lässt sich die veränderte Kristallstruktur nach dem Phasenübergang identifizieren. Die Möglichkeit zur Dispersionsanalyse veränderter Strukturen bleibt sogar erhalten, wenn die Orientierung der neuen Phase nicht bekannt ist. Beispielsweise sind das optisch einachsige und orthorhombische Kristallsystem durch das Auftreten von entarteten Schwingungen im optisch einachsigen Kristallsystem unterscheidbar. Im orthorhombischen Kristallsystem existieren keine entarteten Schwingungen. Das orthorhombische und monokline Kristallsystem sind dadurch unterscheidbar, dass die Bedingung für die zueinander orthogonale Orientierung der Übergangsmomente im monoklinen System nicht mehr gilt. Das monokline und trikline Kristallsystem wiederum können durch die vorhandene Vorzugsrichtung im monoklinen System unterschieden werden, die im triklinen

System nicht mehr existiert. Durch eine veränderte Aufspaltung von ursprünglich dreifach entarteten Schwingungen wird ein veränderter Verzerrungsgrad von hoch symmetrischen Einheiten in tetraedrischer oder oktaedrischer Koordination vor und nach dem Phasenübergang sichtbar. Darüber hinaus ist es offensichtlich, dass, selbst wenn der Ausgangspunkt eines Phasenübergangs ein Hauptschnitt eines optisch einachsig oder orthorhombischen Kristalls ist, die Untersuchung einzelner Tensorkomponenten mittels polarisierter einfallender Strahlung bei einem Übergang in das monokline oder trikline System nicht mehr möglich ist.

Mit dieser Arbeit ist es gelungen, mit dem entwickelten Messverfahren und das für jedes Kristallsystem angepasste Auswerteverfahren der Unterscheidung zwischen kubischen, optisch einachsigen, orthorhombischen, monoklinen und triklinen Kristallen einen großen Schritt näher zu kommen. Die Ergebnisse dieser Arbeit stellen die Grundlage zur Entwicklung eines Algorithmus dar, der nicht nur die verallgemeinerte Dispersionsanalyse eines beliebig geschnittenen Kristalls unbekannter Orientierung ohne Kontrolle des Anwenders, sondern der auch das anfangs unbekannte Kristallsystem der Probe bestimmt. Der Algorithmus könnte so erweitert werden, dass nur noch die Reflexionsspektren gemessen werden müssen, während der Algorithmus ohne die jetzt noch notwendige Unterstützung des Anwenders automatisch läuft.

Bibliography

[1] W. G. Spitzer, D. A. Kleinman, and D. Walsh. Infrared Properties of Hexagonal Silicon Carbide. *Physical Review*, 113(1):127–132, 1959.

[2] M. Czerny. Messungen am Steinsalz im Ultraroten zur Prüfung der Dispersionstheorie. *Zeitschrift für Physik*, 65:600–631, 1930.

[3] C. H. Perry, D. J. McCarthy, and G. Rupprecht. Dielectric Dispersion of Some Perovskite Zirconates. *Physical Review*, 138:1537–1538, 1965.

[4] E. Wiesendanger. Dielectric, mechanical and optical properties of orthorhombic $KNbO_3$. *Ferroelectrics*, 6:1:263–281, 1973.

[5] E. E. Koch, A. Otto, and K. L. Kliewwer. Reflection spectroscopy on monoclinic crystals. *Chemical Physics*, 3(3):362–369, 1974.

[6] M. V. Belousov and V. F. Pavinich. Infrared reflection spectra of monoclininc crystals. *Optics and Spectroscopy*, 45:771–774, 1978.

[7] A. G. Emslie and J. R. Aronson. Determination of the complex dielectric tensor of triclinic crystals: theory. *Journal of the Optical Society of America*, 73(7):916–919, 1983.

[8] J. R. Aronson, A. G. Emslie, and P. F. Strong. Optical constants of triclinic anisotropic crystals: blue vitriol. *Applied Optics*, 24(8):1200–1203, 1985.

[9] S. Höfer, J. Popp, and Th. G. Mayerhöfer. Determination of the dielectric tensor function of triclinic $CuSO_4{\cdot}5H_2O$. *Vibrational Spectroscopy*, 67:44–45, 2013.

[10] S. Höfer, J. Popp, and Th. G. Mayerhöfer. Dispersion analysis of triclinic $K_2Cr_2O_7$. *Vibrational Spectroscopy*, 72:111–118, 2014.

[11] J. Weidlein, U. Müller, and K. Dehnicke. *Schwingungsspektroskopie - Eine Einführung*. Georg Thieme Verlag, 1988.

[12] W. Greiner. *Klassische Elektrodynamik*. Verlag Harri Deutsch, 2002.

[13] Hans J. Paus, editor. *Physik in Experimenten und Beispielen*. Hanser, 2002.

[14] H. Stroppe, editor. *Physik für Studenten der Natur- und Ingenieurwissenschaften*. Fachbuchverlag Leipzig, 2003.

[15] A. Yariv and P. Yeh. *Optical Electronics in Modern Communications*. Oxford University Press, 2007.

[16] D. M. Roessler. Kramers-Kronig analysis of reflection data. *British Journal of Applied Physics*, 16:1119–1123, 1965.

[17] D. W. Berreman. Optics in Stratified and Anisotropic Media: 4×4-Matrix Formalism. *Journal of the Optical Society of America*, 62:502–510, 1972.

[18] P. Yeh. Electromagnetic propagation in birefringent layered media. *Journal of the Optical Society of America*, 69:742–756, 1979.

[19] Pochi Yeh. *Optical Waves in Layered Media*. Wiley Interscience, 2005.

[20] K Kopitzki. *Einführung in die Festkörperphysik*. Teubner Studienbücher, 1993.

[21] D. M. Henderson. Euler angles, Quaternions, and Transformation Matrices - Working Relationships. *National Aeronautics and Space Administration, Mission Planning and Analysis Division*, 1977.

[22] Th. G. Mayerhöfer. Symmetric Euler orientation representations for orientational averaging. *Spectrochimica Acta A*, 61:2611–2621, 2004.

[23] P. Yeh. Optics of anisotropic layered media: A new 4×4 matrix algebra. *Surface Science*, 96(13):41–53, 1980.

[24] R. Adato, A. Artar, S. Erramilli, and H. Altug. Enginieered Absorption Enhancement and Induced Transparency in Coupled Molecular and Plasmonic Resonator Systems. *Nano Letters*, 13:2584–2591, 2013.

[25] W. Kleber. *Einführung in die Kristallographie*. Verlag Technik, 1998.

[26] Th. Hahn, editor. *International Tables for Crystallography A*. Springer Verlag, 2005.

[27] Walter Lovenberg. *Iron sulphur proteins, part 2*. Academic press, 1973.

[28] Th. G. Mayerhöfer, V. Ivanovski, and J. Popp. Dispersion analysis of non-normal reflection spectra from monoclinic crystals. *Vibrational Spectroscopy*, 63:396–403, 2012.

[29] Thermo Nicolet Corporation. *Introduction to Fourier Transform Infrared Spectrometry*. 2001.

[30] R. J. Marks. *Introduction to Shannon Sampling and Interpolation Theory*. Springer Verlag, 1991.

[31] http://www.mathworks.de/.

[32] D. L. Rousseau, R. P. Bauman, and S. P. S. Porto. Normal Mode Determination in Crystals. *Journal of Raman Specroscopy*, 10:253–290, 1981.

[33] W. C. Davidon. Variable Metric Method for Minimization. *SIAM Journal on Optimization*, 1:1–17, 1991.

[34] Lagarias, L. C. and Reeds, J. A. and Wright, M. H. and Wright, P. E. Convergence properties of the nelder-mead simplex method in low dimensions. *SIAM Journal on Optimization*, 9:112–147, 1998.

[35] *Inorganic Crystal Structure Database, Collection Code 60059.*

[36] *Inorganic Crystal Structure Database, Collection Code 21499.*

[37] J. K. Brandon and I. D. Brown. An accurate determination of the crystal structure of triclinic potassium dichromate, $K_2Cr_2O_7$. *Canadian Journal of Chemistry*, 46(6):933–941, 1968.

[38] G. S. Smith and F. E. Alexander. Refinement of the Atomic Parameters of α-Quartz. *Acta Crystallographica Section A: Foundations of Crystallography*, 16:462–471, 1963.

[39] W. Bragg and R. E. Gibbs. The Structure of α and β Quartz. *Proceedings of the Royal Society of London Series A*, 89:406–427, 1925.

[40] M. L. Huggins. The crystal structure of Quartz. *Physical Review*, 19:363–368, 1922.

[41] G. S. Smith and L. E. Alexander. Refinement of the Atomic Parameters of α-Quartz. *Acta Crystallographica A*, 16:462–471, 1963.

[42] H. D. Megaw. Thermal Vibrations and a Lattice Mode in Calcite and Sodium Nitrate. *Acta Crystallographica Section A: Foundations of Crystallography*, 26:235–244, 1969.

[43] A. Yamamoto, Y. Shiro, and H. Murata. Optically-active Vibrations and Elastic Constants of Calcite and Aragonite. *Bulletin of the Chemical Society of Japan*, 47:265–273, 1974.

[44] H. D. Megaw. A Note on the structure of Litium Niobate, $LiNbO_3$. *Acta Crystallographica Section A: Foundations of Crystallography*, 24:583–588, 1968.

[45] S. C. Abrahams, J. M. Reddy, and J. L. Bernstein. Ferroelectric Lithium Niobate 3. Single Crystal X-Ray Diffraction Study at 24° C. *Journal of Physics and Chemistry of Solids*, 27:997–1012, 1966.

[46] A. S. Barker and R. Loudon. Dielectric Properties and Optical Phonons in $LiNbO_3$. *Physical Review*, 158:433–445, 1967.

[47] *Inorganic Crystal Structure Database, Collection Code 83348.*

[48] L. Vasylechko, L. Akselrud, W. Morgenroth, U. Bismayer, A. Matkovskii, and D. Savytskii. The crystal structure of $NdGaO_3$ at 100 K and 293 K based of synchrotron data. *Journal of Alloys and Compounds*, 297:46–52, 2000.

[49] J. M. Beny and B. Piriou. Vibrational Spectra of Single-crystal Topaz. *Physics and Chemistry of Minerals*, 15:148–154, 1987.

[50] P. H. Ribbe and G. V. Gibbs. The crystal structure of topaz and its relation to physical properties. *The American Mineralogist*, 56:24–30, 1971.

[51] *Inorganic Crystal Structure Database, Collection Code 28021.*

[52] J. Felsche. The Crystal Chemistry of the Rare-Earth Silicate. *Structure and Bonding*, 13:99–197, 1973.

[53] J. Wang, S. Tian, G. Li, F. Liao, and X. Jing. Preparation and X-ray characterization of low-temperature phases of R_2SiO_5 (R=rare earth elements). *Material Research Bulletin*, 36:1855–1861, 2001.

[54] Spodumene, $LiAlSi_2O_6$. *Mineral Data Publishing, version 1.2.*

[55] F. C. Hawthorne and H. D. Grundy. Refinement of the crystal structure of $LiScSi_2O_6$ and structural variations in alkali pyroxenes. *Canadian Mineralogist*, 15:50–58, 1977.

[56] M. Cameron, Sh. Sueno, C. T. Prewitt, and Papike J. J. High-Temperature Crystal Chemistry of Acmite, Diopside, Hedenbergite, Jadeite, Spodumene, and Ureyite. *American Mineralogist*, 58:594–618, 1973.

[57] J. Berger. Infrared and Raman spectra of $CuSO_4{\cdot}5H_2O$, $CuSO_4{\cdot}5D_2O$ and $CuSeO_4{\cdot}5D_2O$. *Journal of Raman Spectroscopy*, 5:103–114, 1976.

[58] R. L. Carter and C. E. Bricker. Vibrational Spectrum of triclinic Potassium Dichromate. *Spectroscopy Letters*, 2:247–253, 1969.

[59] K. A. O'Donnell and M. E. Knotts. Polarization dependence of scattering from one-dimensional rough surfaces. *Journal of the Optical Society of America, A*, 8:1126–1131, 1991.

[60] Th. G. Mayerhöfer and J. Popp. Employing spectra of polycrystalline materials for the verification of optical constants obtained from corresponding low-symmetry single crystals. *Applied Optics*, 46:327–334, 2007.

[61] Th. G. Mayerhöfer and J. Popp. Modelling IR spectra of polycrystalline materials in the large crystallites limit-quantitative determination of orientation. *Journal of Optics A*, 8:657–671, 2006.

[62] J. F. Scott and S. P. S Porto. Longitudinal and Transverse Optical Lattice Vibrations in Quartz. *Physical Review*, 161:903–910, 1967.

[63] W. G. Spitzer and D. A. Kleinman. Infrared Lattice Bands of Quartz. *Physical Review*, 121(5):1324–1335, 1961. PR.

[64] Q. Williams. *Infrared , Raman and Optical Spectroscopy of Earth Minerals - A Handbook of physical constants*. Amerian Geophysical Union, 1995.

[65] Bh. J. Saikia, G. Parthasarathy, and N. C. Sarmah. Fourier transform infrared spectroscopic estimation of crystallinity in SiO_2 based rocks. *Bulletin of Material Sciences*, 31:775–779, 2008.

[66] D. M. Lane. Midinfrared optical constants of calcite and their relationship to particle size effects in thermal emission spectra of granular calcite. *Journal of Geophysical Research*, 104:14.099–14.108, 1999.

[67] J.-Ph. Pérez. *Optik*. Spektrum, 1996.

[68] Inrad Optics. Datasheet on Lithium Niobate.

[69] Edward Collett. *Field Guide to Polarization*. Spie Press Book, 2005.

[70] J. Suda, T. Mori, H. Saito, O. Kamishima, T. Hattori, and T. Sato. First order Raman spectra and lattice dynamics of a $NdGaO_3$ crystal. *Physical Review B*, 66:174302–1 – 174302–9, 2002.

[71] D. M Adams and D. J. Hills. Single-crystal Vibrational Spectrum of Topaz and some Comments on Spodumene. *Journal of the Chemical Society, Dalton Transactions*, 16:1562–1565, 1977.

Index of symbols

Code for vibration symmetries

A	symmetry to axis with highest symmetry (principal axis) is preserved during vibration
B	symmetry to principal axis is not preserved during vibration
E	twofold degenerate vibration (neither symmetric nor asymmetric to principal axis)
F	threefold degenerate vibration (neither symmetric nor asymmetric to principal axis)
index g	center of inversion (if present) is preserved during vibration
index u	center of inversion (if present) is not preserved during vibration
indices 1,2,3	symmetry to other axes than principal axis is preserved during vibration

Other symbols

A, B, C	amplitudes of incident, reflected and transmitted wave
A(ϕ, θ, Ψ)	Euler Matrix as function of ϕ, θ, Ψ, rotation around new axes
(a, b, c)	crystal unit cell axes
D	differential propagation matrix
$\vec{D}$	dielectric displacement field
$\vec{E}$	external electric field
d	traveled distance of the mobile mirror in the FTIR-spectrometer
f_{corr}	constant multiplication factor for reflection spectra
$\vec{H}$	magnetic field
Im{number}	imaginary part of an complex quantity
(h, k, l)	Miller indices of normals to a crystal plane
[h, k, l]	Miller indices of crystal axes
{h, k, l}	Miller indices of crystal faces; h,k,k values get permuted to address all faces that are described by that numbers
i	imaginary unit
$\vec{k}$	wave vector
M	linking matrix of A, B and C

$\mathbf{M}_{rot}$	rotation matrix (rotation around fixed axes)
m_e	electron mass
N	number of atoms or molecules per volume or number of oscillators (context)
$\vec{p}$	induced dipole moment
R	measured reflectivity=$r \cdot r^*$
R_{mir}	reflection spectrum of gold mirror
R_{ru}	reflection spectrum of reflection unit
R_{spec}	reflection spectrum of sample
$\mathrm{R}_{spec'}$	corrected reflection spectrum of sample
indices s,p	transmission direction of polarizer in relation to the plane of incidence
indices ss,sp,pp,ps	transmission direction (first index) of polarizer and analyzer (second index) in relation to plane of incidence
Re{number}	real part of an complex quantity
r	reflection coefficient
S_j	strength of the jth oscillator
t	time
t, j, g, n	running variables of sums
(X, Y, Z)	coordinates of external (laboratory) coordinate system
(x, y, z)	coordinates of internal (crystal) coordinate system
x	excitation of an electron at a certain time
$\Delta\nu$	resolution of FTIR-spectrometer
Φ, Θ / ϕ, ϑ	orientation angles of transition moments in spherical coordinates
$\vec{\Psi}$	field vector
χ_e	dielectric susceptibility
α	angle of incidence
α, β, γ	angles between crystal axes
β, τ, σ	angles of rotation matrix for monoclinic crystals
γ_j	damping constant of jth oscillator
ε_0	vacuum permittivity $8.854{\cdot}10^{-12}$ $\mathrm{A^2s^4/kg\,m^3}$
ε_∞	dielectric background tensor
$\varepsilon_{X,Y,Z}(\tilde{\nu})$	dielectric tensor function in external coordinates
$\varepsilon_{x,y,z}(\tilde{\nu})$	dielectric tensor function in internal coordinates
(ϕ, θ, Ψ)	rotation angles in Euler matrix
λ	wavelength
μ	magnetic permeability
$\tilde{\nu}_j$	resonance wavenumber of jth oscillator
ω	frequency
∇	operator for partial derivatives

Publications resulting from this thesis

- S. Höfer, J. Popp and Th. G. Mayerhöfer. Determination of the dielectric tensor function of triclinic $CuSO_4 \cdot 5\,H_2O$. *Vibrational Spectroscopy*. 67:44-54, 2013
- S. Höfer, J. Popp and Th. G. Mayerhöfer. Dispersion analysis of triclinic $K_2Cr_2O_7$. *Vibrational Spectroscopy*, 72:111-118, 2014
- R. M. Almeida, S. Höfer, Th. G. Mayeröfer, J. Popp, K. Krambrock, R. P. S. M Lobo, A. Dias and R. L. Moreira. Optical phonon features of triclinic montebrasite: dispersion analysis and non-polar Raman modes. *Vibrational Spectroscopy, submitted*, 2014
- S. Höfer, R. Uecker, A. Kwasniewski, J. Popp, Th. G. Mayerhöfer. Complete dispersion analysis of single crystal neodymium gallate. *Vibrational Spectroscopy, submitted*, 2014
- S. Höfer, R. Uecker, A. Kwasniewski, J. Popp, Th. G. Mayerhöfer. Dispersion analysis of arbitrarily cut uniaxial crystals. *Vibrational Spectroscopy, submitted*, 2014

Danksagung

An dieser Stelle möchte ich mit bei allen bedanken, die mich bei der Erstellung dieser Arbeit unterstützt haben.

- Dabei möchte ich mit zunächst bei Professor Popp bedanken für die Einstellung meiner Person als Doktorandin und die Übertragung dieses Themas.
- Besonderer Dank geht an Thomas Mayerhöfer für die vielfältige Unterstützung bei fachlichen Fragen und bei der Erstellung dieser Arbeit.
- Bei Frank Hänschke möchte ich mich für die Betreuung währen den Messungen bedanken.
- Bei Dr. Ortrud Werhan möchte ich mich für die Hilfe bei den Röntgenmessungen bedanken sowie für die Bereitstellung verschiedener Kristalle.
- Bei Gabriele Möller möchte ich mich für das Präparieren und Polieren vieler Proben bedanken.
- Vielen Dank an Marion Ludwig für die Hilfe bei der Herstellung der Presslinge
- Vielen Dank auch an Dr. Vladimir Ivanovski für die Bereitstellung mehrerer Kristalle.
- Besonderer Dank geht auch an die Mitarbeiter der Mineralogischen Sammlung für die Dauerleihgabe einiger, durchaus auch wertvoller Kristalle.
- Der größte Dank geht an meinen Mann für die selbstlose Unterstützung in allen Lebenslagen, sowie meiner Familie, ohne deren finanzieller Unterstützung noch nicht einmal das Studium, die Grundlage einer jeden Promotion, möglich gewesen wäre.

Selbstständigkeitserklärung

Ich erkläre, dass ich die vorliegende Arbeit selbstständig und unter Verwendung der angegebenen Hilfsmittel, persönlichen Mitteilungen und Quellen angefertigt habe.

Jena, den 02.02.2015

Sonja Höfer